National Library
of Canada

Acquisitions and
Bibliographic Services Branch

395 Wellington Street
Ottawa, Ontario
K1A 0N4

Bibliothèque nationale
du Canada

Direction des acquisitions et
des services bibliographiques

395, rue Wellington
Ottawa (Ontario)
K1A 0N4

Your file Votre référence

Our file Notre référence

NOTICE

The quality of this microform is heavily dependent upon the quality of the original thesis submitted for microfilming. Every effort has been made to ensure the highest quality of reproduction possible.

If pages are missing, contact the university which granted the degree.

Some pages may have indistinct print especially if the original pages were typed with a poor typewriter ribbon or if the university sent us an inferior photocopy.

Reproduction in full or in part of this microform is governed by the Canadian Copyright Act, R.S.C. 1970, c. C-30, and subsequent amendments.

AVIS

La qualité de cette microforme dépend grandement de la qualité de la thèse soumise au microfilmage. Nous avons tout fait pour assurer une qualité supérieure de reproduction.

S'il manque des pages, veuillez communiquer avec l'université qui a conféré le grade.

La qualité d'impression de certaines pages peut laisser à désirer, surtout si les pages originales ont été dactylographiées à l'aide d'un ruban usé ou si l'université nous a fait parvenir une photocopie de qualité inférieure.

La reproduction, même partielle, de cette microforme est soumise à la Loi canadienne sur le droit d'auteur, SRC 1970, c. C-30, et ses amendements subséquents.

Canada

PARAMETER ESTIMATION IN OCEANOGRAPHIC FLOWS AND COMPUTATION OF FLOWS DRIVEN BY DENSITY GRADIENT

by

SALIL KUMAR DAS

M.Sc. (Applied Mathematics)
SIMON FRASER UNIVERSITY, CANADA, 1989.

THESIS SUBMITTED IN PARTIAL FULFILLMENT OF

THE REQUIREMENTS FOR THE DEGREE OF

DOCTOR OF PHILOSOPHY

in the Department
of
Mathematics and Statistics

SIMON FRASER UNIVERSITY
MAY 1991.

ISBN 0-315-78171-8

APPROVAL

Name: Salil Kumar Das

Degree: Doctor of Philosophy

Title of Thesis: Parameter estimation in oceanographic flows and computation of flows driven by density gradient

Examining Committee:

Chairman: Professor C. Villegas

R.W. Lardner
Senior Supervisor

G. Bojadziev

M. Trummer

C.Y.Shen
Examiner
Simon Fraser University.

I.M. Navon
External Examiner
Professor
Department of Mathematics
and
Supercomputer Computations Research Institute
Florida State University
Tallahassee, Florida, U.S.A.

Date Approved: May 24, 1991

PARTIAL COPYRIGHT LICENSE

I hereby grant to Simon Fraser University the right to lend my thesis, project or extended essay (the title of which is shown below) to users of the Simon Fraser University Library, and to make partial or single copies only for such users or in response to a request from the library of any other university, or other educational institution, on its own behalf or for one of its users. I further agree that permission for multiple copying of this work for scholarly purposes may be granted by me or the Dean of Graduate Studies. It is understood that copying or publication of this work for financial gain shall not be allowed without my written permission.

Title of Thesis/Project/Extended Essay

Parameter estimation in oceanographic flows and computation of flows driven by density gradient

Author:

(signature)

SALIL KUMAR DAS

(name)

27th Nov 1991

(date)

ABSTRACT

This thesis is based on two distinct studies. In the first a model is described for the computation of flows in shallow seas driven by density gradients. Two numerical algorithms are proposed. The first one is based on a splitting method: at each time-step, the surface elevation and vertically integrated mass transports are computed from the depth-averaged equations, then the vertical structure of the current is obtained from the horizontal momentum equations. The second is based on a Galerkin spectral method using eddyviscosity eigenfunctions for the vertical coordinate and a B-grid for the horizontal coordinates. The accuracy of the former is tested on four problems and that of the latter on two problems for which exact steady-state solutions can be computed. These problems have been chosen to distinguish between the effects of horizontal density gradients, vertical structure of the density field, variable depth and Coriolis forces. Both the numerical models are then used to compute that part of the residual currents in the Arabian Gulf caused by density gradient, using as input a series of measurements of the density field made during the Winter of 1977.

The second part of the thesis is concerned with the estimation of both constant and position-dependent parameters in a sectionally integrated hydrodynamical model of tidal flow. Bottom friction coefficients and water depth are parameters estimated and the available data consists of measured periodic values of water surface height at certain stations. The adjoint equation formulation is used to obtain the parameter equations, and several optimization algorithms are examined and compared for the iterative refinement of the parameter values. A direct method, which avoids the use of the gradient of the cost function, has also been investigated to estimate the optimal values of the constant parameters. This method is somewhat more expensive than the adjoint/variational method.

ACKNOWLEDGEMENT

With a sincere sense of gratitude, I would like to express my thanks to Prof. R.W. Lardner, for his constant encouragement and support during the course of this work. His suggestions and criticisms were most relevant and valuable to the research work. I was fortunate to get this opportunity to work with him.

I would like to thank Dr. Steve Kloster for his help with the computer graphics. I also wish to thank the staff members of the Department of Mathematics and Statistics for their untiring and selfless administrative help.

Finally I would like to thank my wife, Soma, for her constant support.

TABLE OF CONTENTS

LIST OF FIGURES

CHAPTER 1 INTRODUCTION

Most numerical models presently being used for computing flows due to tides and storm surges are based on the so-called shallow water equations. These equations are obtained from the full three-dimensional hydrodynamical equations by averaging over the vertical co-ordinate. There are several computational methods which have been used to solve numerically these equations. Finite-difference schemes (Hansen 1962; Leendertse 1967; Matthews and Mungall 1972; Flather and Heaps 1975; Lardner et al 1982; Duff 1983) are the most widely used techniques among these methods. Other numerical schemes have been devised, using finite elements (Connor and Wang 1973; Taylor and Davis 1975; Brebbia and Partridge 1976; Connor and Brebbia 1976; Pinder and Gray 1977; Wang 1978), harmonic analysis in time plus finite elements in space (Le Provost and Poncet 1978; Le Provost et al 1981; Pearson and Winter 1977) and the method of characteristics (Townson 1974; Lai 1976; Lardner et al 1986; Cekirge et al 1986).

In spite of the approximations made in the advective terms and the bottom friction terms in deriving the shallow water equations, the two-dimensional schemes are highly successful for tidal flows but yield only the free surface height and depth-averaged components of velocity. For many purposes this information is not enough, and the vertical profile of the velocity is required, for example, when computing the movement of an oil slick (which depends strongly on the surface velocity), the force on an underwater pipeline or wind driven flow (where the surface velocity differs strongly from the depth-averaged velocity). For this purpose, in recent years, three-dimensional flow models have been developed by a number of workers. The earliest of these models are based on some kind of finite difference schemes in three dimensions (Sundermann 1974; Simons 1974; Laevastu 1975; Leendertse & Liu 1975a, b; Sengupta et al 1978; Johns et al 1983). Heaps (1979) has used an appropriate integral transform in the vertical dimension. Davies & Owen (1979) and Davies (1980a, b; 1983) have used a Galerkin method of solution, using various sets of basis functions of the vertical coordinate. Recently, Lardner (1990) has proposed a more efficient numerical algorithm based on a Galerkin spectral method using eddy-viscosity eigenfunctions for the vertical coordinate.

All of these three-dimensional schemes are generally an order of magnitude more expensive in computer time than the two-dimensional schemes. Another approach in which the two-dimensional equations are solved using bottom friction modelled by a convolution integral

derived from the three-dimensional equations has been proposed by Welander (1957), Jelesniansky (1970), Forristal (1974, 1980), Jordan and Baker (1980), Davies (1987, 1988), Jamart and Ozer (1987) and Hearn and Hunter (1988). This algorithm, which treats the convolution integral in an approximate way, compares well with the two-dimensional algorithms in computer time, but is practically infeasible when the viscosity coefficient is a general time-dependent function.

Lardner & Cekirge (1988) and Lardner & Smoczynski (1990) have proposed an alternative scheme, called the V/HS algorithm (short for vertical/horizontal splitting). The basic approach of this algorithm is to obtain the surface elevation and the depth-averaged velocity components at the given time step using one of the existing two-dimensional schemes. These values are then used as a part of the input to the horizontal momentum equations, which are solved separately at each horizontal grid point for the vertical profiles of the velocity. Davies (1985a) and Lardner & Cekirge (1987) have used this approach to obtain velocity profiles from steady flows, and Davies (1985b) and Backhaus (1985) have proposed related schemes for dynamical problems.

In the first part of the thesis, we shall be concerned with computation of the currents caused by such gradients. Density gradients in near-coastal seas are established by such processes as evaporation, fresh-water run-off and precipitation. While the magnitude of these currents is usually quite small, compared to tidal currents for example, they can be a dominant factor in phenomena such as pollutant transport where long-term drift is of concern.

We shall be interested in particular in modelling a commonly found situation in which the time-scale for changes in the density field itself is much longer than the time-scale for establishment of a quasi-steady flow field in the region of interest. In this situation, it is possible to ignore the salinity transport when computing the flow velocities and to assume that the density field is fixed. Its values can be taken from observational measurements.

We shall describe and test two numerical schemes for computing such density-driven flows, the first based on the V/HS algorithm and the second on the spectral method in the vertical and a B-grid in the horizontal, and shall apply these schemes to the computation of these flows in the Arabian Gulf. Here the dominant factor in establishing the density gradient is evaporation; the fresh-water run-off is rather insignificant except near the head of the Gulf. The changes in density field typically occur over time-scales of one to three months, while the time-scale for establishment of a steady flow over the region is not more than about a week.

The accuracy of the algorithms will be tested on a number of test problems for which the exact steady state solutions are known. The basic density driven flow pattern in the Arabian Gulf turns out to be as expected, but the details of the flow show several surprising features. In particular, the magnitudes of the velocities are smaller by a factor of 2-5 than has been suggested by some authors.The algorithm based on the spectral method produces more accurate results in the test problems than the direction-splitting algorithm and the computed flow in the Gulf, while generally consistent with that found using the latter algorithm, does not show the irregularities near the open boundary found there, and in other earlier computations.

The second part of the thesis is concerned with the estimation of parameters in numerical tidal models. The earliest such models have been based on the vertically-integrated continuity and momentum equations, and yield values of the surface elevation and depth-averaged velocity components. The parameters in such models are usually the water depth and the bottom friction coefficient, both of which are in general position-dependent. Traditionally, numerical tidal models are "tuned" by adjusting these parameters so as to make the predicted surface elevations at certain tide stations agree as closely as possible with their observed values. This technique is not only tedious and difficult to do in any systematic way, but is also unsatisfactory insofar as one can never be sure that such "manual" adjustment of the parameters yields their optimal values. These difficulties become greatly magnified in the case of full three-dimensional numerical models in which the vertical profiles of velocity are computed and in which additional parameters such as eddy-viscosity must be estimated.

In recent years systematic techniques of data assimilation based on optimal control methods have been developed, particularly in the field of meteorology. These methods were originated by Sasaki (1955, 1970) and Marchuk (1974) and have more recently been developed and applied by Lewis and Derber (1985), Le Dimet and Talagrand (1986), Harlan and O'Brien (1986), Hoffman (1986), Lorenc (1986, 1988), Talagrand and Courtier (1987) and Courtier and Talagrand (1987). Recent reviews of much of this work are given by Lorenc (1986), Navon (1986) and Le Dimet and Navon (1989). Similar methods have also been used by Chavent et al. (1975) and Carrera and Neumann (1986a,b,c) to estimate the parameters in models of flow in porous media.

In the field of oceanography such optimal control methods have also recently come into use. Bennett and McIntosh (1982) and Prevost and Salmon (1986) have applied the weak

constraint formalism of Sasaki (1970) to tidal flow and geostrophic flow problems. More recently the strong constraint formalism has been used by Panchang and O'Brien (1989) to determine the bottom friction coefficient in a problem of flow in a channel using some earlier experimental results. Smedstad and O'Brien (1991) has extended this approach and used it to determine the effective phase speed in a model of the equatorial Pacific Ocean based on observations of sea level. Yu and O'Brien (1990) have used a similar method to estimate the eddy viscosity and surface drag coefficient from measured velocities of a wind-driven flow. In recent years, extensive application of the adjoint/variational formulation to the North Atlantic Ocean using steady state general circulation models have been carried out by Tziperman and his associates (see, Tziperman and Thacker, 1989; Tziperman et al 1990a, b). Among other things, they have calculated poorly known parameters such as eddy-mixing coefficients, and surface forcing and tracer boundary fluxes by fitting model results to observations.

For many water bodies, there exists an abundance of observational data on tidal amplitudes and phases, collected often over several decades from tide gauges. This thesis is concerned with the assimilation of such periodic data, using Sasaki's strong constraint formalism, in order to estimate the parameters in a depth-averaged numerical tidal model. The work is an extension in several directions of that of Panchang & O'Brien (1989). First, we have investigated the feasibility of using this approach to estimate more than one parameter and, more importantly, distributed parameters; second, we have assimilated periodic data rather than initial value data; and third, we have examined and compared several numerical optimization algorithms.

We shall consider an idealized problem, similar to that considered by Panchang and O'Brien (1989), involving flow in a channel of uniform width. One end of the channel is open, the other closed, and the water elevation at the open end is varied harmonically with some known amplitude. Measurements of surface elevation are assumed to be made at two tide stations at points interior to the channel. In the case of linear friction and constant depth, the "measured" values are assumed to be equal to the analytic solutions at the two stations. In cases of quadratic friction and/or variable parameters, they are computed numerically using a grid and time-step an order of magnitude smaller than those used for the parameter estimation.

The parameters to be estimated are the water depth and either the linear or quadratic bottom friction coefficient. (In tidal models, the bathymetry is commonly taken from navigational charts, and such depths must be corrected by amounts that are unknown a priori, for two reasons: navigational charts are invariably conservative insofar as they are designed to

prevent ships hitting bottom, and second, the depths on them are relative to some low water level that must be corrected to mean water level. It is reasonable to treat such depth corrections as tuning parameters that are adjusted to optimize the fit with observed surface elevations.)

The variational method involves minimizing a certain functional with the given boundary value problem as a constraint. Construction of the gradient of this functional with respect to the parameters leads to an adjoint boundary value problem that must be solved backwards in time. A similar numerical method is used to solve both the direct and adjoint dynamical equations, namely a leapfrog method with staggered spatial and temporal grids. Several minimization algorithms are examined and compared for computing the final parameter values using the computed gradients: the secant method, a direct iteration method proposed by Panchang and O'Brien (1989), the Polak-Ribiere conjugate gradient method, the conjugate gradient method with Beale restarts and the BFGS quasi-Newton method.

We will also present a second approach for estimating the parameters in the same channel problem using a direct optimization method which avoids the use of gradient of the cost function.

In chapter 2 we present the basic equations on which the work in this thesis will be based. Chapter 3 describes the numerical algorithms used to compute the density driven flows. The test problems on which these algorithms will be tested for accuracy will be presented in chapter 4. In chapter 5 we will present the results obtained for the Arabian Gulf. Chapter 6 and 7 will contain the derivation of the adjoint equation, continuous and discrete, and test results applying the numerical algorithms for parameter estimation on one-dimensional channel problem with tidal-forcing. Finally, in Chapter 8 we present the results on parameter estimation using an optimization method which does not use the gradient.

CHAPTER 2 BASIC EQUATIONS

The equations that form the basis of the model are the usual momentum and mass conservation equations and their depth-averaged forms. For the present problem these equations contain some extra terms beyond those commonly used. The basic equations here are based on an eddy-viscosity model of turbulence; furthermore the fluid is assumed to be incompressible, horizontal eddy shear stresses are neglected, and the vertical momentum equation is approximated by the hydrostatic pressure equation.

We use a system of Cartesian coordinates with the z - axis pointing vertically upwards and the xy - plane occupying the undisturbed position of the water surface. The position of the bottom is taken to be $z = -h\ (x, y)$ while the surface at time t is $z = \zeta\ (x, y, t)$. The horizontal components of fluid velocity are denoted by $u\ (x, y, z, t)$ and $v\ (x, y, z, t)$.

As usual, the vertical momentum equation is approximated by the hydrostatic equation

$$P(x, y, z, t) = P_0 + \int_z^\zeta g\ \rho(x, y, z')\, dz' \tag{2.1}$$

where P is fluid pressure, P_0 is atmospheric pressure, assumed constant, g is the acceleration due to gravity and $\rho\ (x, y, z)$ the given fluid density.

Flows driven by density gradients are generally quite slow, so that the advective terms in the horizontal momentum equations are very small and can be ignored. These equations then take the form

$$\begin{aligned} \rho(u_t - fv) &= -P_x + (\mu u_z)_z \\ \rho(v_t + fu) &= -P_y + (\mu v_z)_z \end{aligned} \tag{2.2}$$

Here, f is the Coriolis parameter, μ is the (dynamical) eddy viscosity and subscripts of x, y, z or t denote the corresponding partial derivative.

It is convenient to introduce a sigma coordinate (Phillips 1957) in the vertical direction in the usual way as $\sigma = \dfrac{(z + h)}{H}$, where $H = h + \zeta$ is the total water depth. The free surface is

then $\sigma = 1$ while the bottom is $\sigma = 0$. Using the chain rule, we can then rewrite equations (2.2) in the form (Lardner & Smoczynski 1990; Johns et al 1983)

$$\begin{aligned}\rho\left\{ u_t - \frac{\sigma\zeta_t}{H}u_\sigma - fv \right\} &= - P_x - \frac{1}{H}(h_x - \sigma H_x)P_\sigma + \frac{1}{H^2}(\mu u_\sigma)_\sigma \\ \rho\left\{ v_t - \frac{\sigma\zeta_t}{H}v_\sigma + fu \right\} &= - P_y - \frac{1}{H}(h_y - \sigma H_y)P_\sigma + \frac{1}{H^2}(\mu v_\sigma)_\sigma\end{aligned} \tag{2.3}$$

while, from (2.1), the pressure is given by

$$P(x, y, \sigma, t) = P_0 + gH\int_\sigma^1 \rho(x, y, \sigma')\, d\sigma'. \tag{2.4}$$

In equations (2.3), the second term on the left is small and can be neglected. After substituting from (2.4), these equations then simplify to

$$\begin{aligned}u_t - fv - \frac{1}{\rho H^2}(\mu u_\sigma)_\sigma &= - g\zeta_x + T^{(x)} \\ v_t + fu - \frac{1}{\rho H^2}(\mu v_\sigma)_\sigma &= - g\zeta_y + T^{(y)}\end{aligned} \tag{2.5}$$

where

$$T^{(x)} = \frac{g}{\rho}\{ R_x - H(1 - \sigma)\rho_x \}, \qquad T^{(y)} = \frac{g}{\rho}\{ R_y - H(1 - \sigma)\rho_y \} \tag{2.6}$$

and

$$R = H\int_\sigma^1 [\rho(\sigma) - \rho(\sigma')]\, d\sigma'. \tag{2.7}$$

In R, $T^{(x)}$ and $T^{(y)}$, we can approximate $H \approx h$ since this factor is already multiplied by small quantities. This approximation is generally of the same order as our earlier neglect of the advective terms. With this approximation and the earlier assumption that the density field is treated as fixed, $T^{(x)}$ and $T^{(y)}$ provide constant forces driving the flow.

In addition, we have boundary conditions on $\sigma = 0$ and 1. We assume that the surface is free of shear traction, so we have the boundary condition $u_\sigma = v_\sigma = 0$ on $\sigma = 1$. On the bottom the boundary condition is

$$\mu(u_\sigma, v_\sigma) = H(\tau^{(bx)}, \tau^{(by)}) \quad \text{on} \quad \sigma = 0 \tag{2.8}$$

where $\tau^{(bx)}$ and $\tau^{(by)}$ are the components of bottom drag. It is assumed that these components are given in terms of the velocity at the bottom by a combination of linear and quadratic terms,

$$(\tau^{(bx)}, \tau^{(by)}) = \bar{\rho}(\kappa_1 + \kappa_2\sqrt{u^2 + v^2})(u, v) \quad \text{on} \quad \sigma = 0 \tag{2.9}$$

where κ_1 and κ_2 are the linear and quadratic drag coefficients and $\bar{\rho}$ the average density (see below). In general, it is physically more realistic to use a quadratic dependence of bottom friction on velocity, but in the case a density-driven flow is superimposed on other, possibly much larger, flows, such as tidal and wind-driven currents, it may be more appropriate to use the linear form for bottom friction (Hunter 1975). The form (2.9) retains both options.

The kinematical boundary conditions are

$$\zeta_t + u^{(s)}\zeta_x + v^{(s)}\zeta_y - w^{(s)} = -\frac{\rho_0}{\rho^{(s)}}W, \qquad u^{(b)}h_x + v^{(b)}h_y + w^{(b)} = 0 \tag{2.10}$$

where superscripts of s and b refer respectively to $\sigma = 1$ and $\sigma = 0$, w is the vertical component of fluid velocity, W is the velocity of evaporation (minus the velocity of precipitation if that is significant) and ρ_0 the density of pure water.

The mass conservation equation,

$$(\rho u)_x + (\rho v)_y + (\rho w)_z = 0, \tag{2.11}$$

can be used to compute w if required. However, it is used here only in integrated form. Defining the average density and the components of mass transport by

$$\bar{\rho} = \int_0^1 \rho\, d\sigma, \qquad (p, q) = \int_{-h}^{\zeta} \rho(u, v)\, dz = H\int_0^1 \rho(u, v)\, d\sigma \tag{2.12}$$

and integrating equation (2.11) over the water column from $z = -h$ to $z = \zeta$, we get, (Pinder & Gray 1977) after using (2.10),

$$\rho^{(s)}\zeta_t + p_x + q_y = -W\rho_0 \tag{2.13}$$

The depth-averaged momentum equations are obtained by similarly integrating equations (2.2) over the water column. They take the form

$$\begin{aligned} p_t - fq &= -g\bar{\rho}H\zeta_x - \tau^{(bx)} - \rho_0 W u^{(s)} - S^{(x)} \\ q_t + fp &= -g\bar{\rho}H\zeta_y - \tau^{(by)} - \rho_0 W v^{(s)} - S^{(y)}, \end{aligned} \tag{2.14}$$

where

$$S^{(x)} = \tfrac{1}{2} gH^2 \bar{\rho}_x + gQ_x, \qquad S^{(y)} = \tfrac{1}{2} gH^2 \bar{\rho}_y + gQ_y,$$

and

$$Q = H^2 \int_0^1 (\rho - \bar{\rho}) \sigma \, d\sigma.$$

Again, we can approximate $H \approx h$ in Q, $S^{(x)}$ and $S^{(y)}$, in which case these terms also become constant driving forces.

We can compute the steady currents caused by a given density field by integrating the dynamical equations (2.5), (2.13) and (2.14), starting with ζ, u and v initially zero everywhere, and stepping forward in t until a steady solution is reached. The time-stepping algorithm we have used (Lardner & Cekirge 1988; Lardner & Smoczynski 1990) is split into two parts: first the quantities ζ, p and q are stepped forward by using the depth-averaged equations (2.13) and (2.14), then the velocity profiles are up-dated by solving equations (2.5). Having found the complete velocity field, the bottom drag stresses are updated by eqn (2.9) for use in eqns (2.14) on the next step. A second algorithm based on a spectral method in the vertical coordinate has also been developed. Further details of these numerical schemes are given in chapter 3.

For both of the algorithms, lateral boundary conditions are required, of the same forms as for the usual two-dimensional hydrodynamical models. On coastal boundaries, the normal component of the mass flux vector (p,q) is taken to be zero. The appropriate condition on the open part of the boundary is the subject of considerable debate and we have tried four different approaches to the condition there.

(i) ζ is set equal to zero at all open boundary points

(ii) ζ is set equal to zero at one of the boundary points and at the other points is determined from the geostrophic balance,

$$\zeta_x = \frac{fq}{g\bar{\rho}H}, \quad \text{or} \quad \zeta_y = -\frac{fp}{g\bar{\rho}H}$$

according to the direction along the boundary.

(iii) A radiation condition of the type proposed by Blumberg and Kantha (1985) is assumed:

$$\zeta_t + \sqrt{gH}\,\zeta_n = -\frac{\zeta}{T_f}$$

where ζ_n is the normal derivative and T_f is a relaxation time.

(iv) The region has been artificially enlarged by an additional five grids normal to the open boundary, with the depth and density extended continuously and the bottom friction substantially increased in the extra region. On the new open boundary a condition of one of the types (i)-(iii) is assumed.

We have found that for each of the two algorithms these four approaches lead to significant differences in the steady flow field only within two or three grid spacings of the open boundary. In the case of the Gulf, with the grid used, the open boundary contains just three grid points, so the solution at all but about six grid points is approximately the same regardless of the boundary condition chosen.

We have also used the algorithms to compute the flows due to some model density fields for which the exact steady state flows can be found and which exhibit four principal features of the problem. These flows are included mainly as a test on the accuracy of the algorithms, but also because they are not without their own interest. The first of them is in fact well-known in the estuarine literature. Details of these tests can be found in chapter 4.

CHAPTER 3 NUMERICAL SCHEMES FOR DENSITY DRIVEN FLOWS

In this chapter, we shall outline the numerical schemes used to compute the velocity fields. First we shall describe the V/HS algorithm and then the spectral method using the eddy-viscosity eigenfunction expansions.

3.1 V/HS ALGORITHM

The time-stepping algorithm (Lardner & Cekirge 1988; Lardner & Smoczynski 1990) is split into two parts: first the quantities ζ, p and q are stepped forward by using the depth-averaged equations (2.13) and (2.14), then the velocity profiles are up-dated by solving equations (2.5).

For the first part, a finite difference method is used, employing an Arakawa C-grid in the xy-plane and a leapfrog time stepping. This algorithm has been described earlier for a simpler set of equations (Lardner & Smoczynski 1990). We use m and n as grid indices in the x and y directions and k to denote the time level. Staggered spatial and temporal grids are used with ζ (and h) specified at points (m, n, k), p specified at points $(m+\frac{1}{2}, n, k+\frac{1}{2})$ and q at points $(m, n+\frac{1}{2}, k+\frac{1}{2})$. Figure 3.1(a) shows the spatial grid and figure 3.1(b) the cross sections of time-planes.The approximating variables are then $\zeta_{m,n}$ at time level k and $p_{m+\frac{1}{2},n}$ and $q_{m,n+\frac{1}{2}}$ at time level $k+\frac{1}{2}$. The finite difference approximations to equations (2.13) and (2.14) are then

$$\zeta^{+}_{m,n} = \zeta_{m,n} - \frac{\tau}{\delta\bar{\rho}_{m,n}}\left(p_{m+\frac{1}{2},n} - p_{m-\frac{1}{2},n} + q_{m,n+\frac{1}{2}} - q_{m,n-\frac{1}{2}}\right) - \frac{\tau W \rho_0}{\bar{\rho}_{m,n}} \tag{3.1}$$

$$p^{+}_{m+\frac{1}{2},n} = p_{m+\frac{1}{2},n} - \frac{g\tau}{\delta}(\bar{\rho h})_{m+\frac{1}{2},n}\left(\zeta^{+}_{m+1,n} - \zeta^{+}_{m,n}\right) - \tau\left[-fq^{(1)}_{m+\frac{1}{2},n} + \tau^{(bx)}_{m+\frac{1}{2},n} + \rho_0 W u^{(s)}_{m+\frac{1}{2},n} + S^{(x)}_{m+\frac{1}{2},n}\right] \tag{3.2}$$

$$q^{+}_{m,n+\frac{1}{2}} = q_{m,n+\frac{1}{2}} - \frac{g\tau}{\delta}(\bar{\rho h})_{m,n+\frac{1}{2}}\left(\zeta^{+}_{m,n+1} - \zeta^{+}_{m,n}\right) - \tau\left[fp^{(1)}_{m,n+\frac{1}{2}} + \tau^{(by)}_{m,n+\frac{1}{2}} + \rho_0 W v^{(s)}_{m,n+\frac{1}{2}} + S^{(y)}_{m,n+\frac{1}{2}}\right] \tag{3.3}$$

Approximation (3.1) is centered at $(m, n, k+\frac{1}{2})$, (3.2) is centered at $(m+\frac{1}{2}, n, k+1)$ and (3.3) at $(m, n+\frac{1}{2}, k+1)$. Here, the superscript '+' denotes an updated variable, that is $\zeta_{m,n}$ at level $k+1$ and $p_{m+\frac{1}{2},n}$ and $q_{m,n+\frac{1}{2}}$ at level $k+\frac{3}{2}$. The size of the time step is τ and the horizontal grid spacing is δ. The local truncation errors in (3.1)-(3.3) are $O(\tau^3, \tau\delta^2)$.To maintain this level of accuracy, the truncation errors in approximating the right hand sides of (2.13) and (2.14) should not be greater than second order, at least in the dominant terms.

The superscript '(1)' in the Coriolis term is used to indicate two things. First the usual four point averages are used. This means that these terms are approximated by central averages:

$$(\overline{f}^{y}q)_{m+\frac{1}{2},n,k+1} = \overline{f}^{y}\overline{q}^{x}_{m,n}, \quad (\overline{f}^{x}p)_{m,n+\frac{1}{2},k+1} = \overline{f}^{x}\overline{p}^{y}_{m,n}, \tag{3.4}$$

where

$$\overline{q}^{xy}_{m,n} = \frac{1}{4}(q_{m,n} + q_{m,n-1} + q_{m+1,n} + q_{m+1,n-1}), \tag{3.5}$$

$$\overline{p}^{xy}_{m,n} = \frac{1}{4}(p_{m,n} + p_{m-1,n} + p_{m,n+1} + p_{m-1,n+1}). \tag{3.6}$$

(The algorithm does not produce spurious boundary layers at coasts, so it is not necessary to use a device such as Jamart and Ozer's wet-points-only averaging (Jamart & Ozer 1987).) Second, p and q are updated in alternating order on successive time steps, with the most recent value of the other variable being used in these Coriolis terms.On odd time-steps, (3.2) is solved first and the updated values $p^{+}_{m,n}$ used to compute $\overline{p}^{xy}_{m,n}$ via (3.6). On even time-steps, (3.3) is solved first and the up-dated values $q^{+}_{m,n}$ used to compute $\overline{q}^{xy}_{m,n}$ via (3.5).

The computation of the vertical velocity profiles as described below is carried out at each (m,n) spatial grid-point and at each time-step $(k+\frac{1}{2})$. After each such computation the bottom drag components $\tau^{(bx)}$ and $\tau^{(by)}$ are computed and stored. At the time-step $k+1$ at which these are required in the right hand side of (3.2) and (3.3) their values are only available for step $k+\frac{1}{2}$. Since the bottom drag terms are relatively significant they must therefore be computed by extrapolation in time:

$$(\tau^{(bx)})_{m+\frac{1}{2},n,k+1} = \frac{1}{4}[3(\tau^{(bx)}_{m+1,n} + \tau^{(bx)}_{m,n}) - ((\tau^{(bx)})^{-}_{m+1,n} + (\tau^{(bx)})^{-}_{m,n})],$$

$$(\tau^{(by)})_{m,\, n+\frac{1}{2},\, k+1} = \tfrac{1}{4}\,[3(\tau^{(by)}{}_{m,\, n+1} + \tau^{(by)}{}_{m,\, n}) - ((\tau^{(by)})^{-}{}_{m,\, n+1} + (\tau^{(by)})^{-}{}_{m,\, n})], \qquad (3.7)$$

where minuses denote values at time-step $(k - \frac{1}{2})$ and the unsuperfixed values refer to the latest available time-step, $(k + \frac{1}{2})$. This again maintains the required order of truncation error.

A generalized Crank-Nicolson scheme (Lardner & Cekirge 1988) is used to approximate equations (2.5). Using an index j for vertical level, with the bottom being at $j = 1$ and the free surface at $j = J + \frac{1}{2}$, we get the following finite difference approximation to these equations. The indices m and n are suppressed for clarity and again the '+' indicates updated values, at time step $k + \frac{3}{2}$ in the case of u and v.

$$u_j^{+} = u_j + \tau f v_j^{\nu} - \frac{\tau}{H^2 \rho_j \Delta\sigma^2}\left[\mu_{j+\frac{1}{2}}(v_{j+1}^{\lambda} - v_j^{\lambda}) - \mu_{j-\frac{1}{2}}(v_j^{\lambda} - v_{j-1}^{\lambda})\right] - \tau g \zeta_x^{+} + \tau T_j^{(x)} \qquad (3.8)$$

$$v_j^{+} = v_j - \tau f u_j^{\nu} - \frac{\tau}{H^2 \rho_j \Delta\sigma^2}\left[\mu_{j+\frac{1}{2}}(u_{j+1}^{\lambda} - u_j^{\lambda}) - \mu_{j-\frac{1}{2}}(u_j^{\lambda} - u_{j-1}^{\lambda})\right] - \tau g \zeta_y^{+} + \tau T_j^{(y)} \qquad (3.9)$$

Here $\Delta\sigma$ is the vertical grid spacing and λ and ν are two implicitness parameters, required for stability, with

$$u_j^{\lambda} = \lambda u_j^{+} + (1 - \lambda) u_j, \qquad v_j^{\lambda} = \lambda v_j^{+} + (1 - \lambda) v_j$$

and u_j^{ν}, v_j^{ν} defined similarly. Equations (3.8) and (3.9) comprise a tri-diagonal system for the updated velocities. This system is solved in conjunction with finite difference approximations to the free surface boundary conditions and to equations (2.12b,c) in which the values of p and q are used from the first part of the algorithm. This, together with the values of ζ in eqns (3.8,9), provide the linkage from the first to the second part of the algorithm.

The velocity profiles computed in the second part of the algorithm are then used to evaluate the bottom stress and surface velocity components in preparation for use in eqns (3.1-3.3) on the next time step. This provides the coupling from the second back to the first part of the algorithm.

Further details of the algorithm (for a fluid of uniform density) can be found in references (Lardner & Cekirge 1988) and (Lardner & Smoczynski 1990) and a discussion of its stability in (Lardner 1990).

3.2 SPECTRAL ALGORITHM

Writing the velocity in complex form, $U = u + iv$, in (2.5) we have

$$\rho U_t - if\rho U - H^{-2}(\mu U_\sigma)_\sigma = -g\rho(\zeta_x + i\zeta_y) + T^{(x)} + iT^{(y)} \tag{3.10}$$

with boundary conditions

$$U_\sigma = 0 \quad on \quad \sigma = 1 \tag{3.11}$$

$$\mu U_\sigma = h\bar{\rho}\kappa U \quad on \quad \sigma = 0 \tag{3.12}$$

In order to solve the boundary value problem (2.13), (3.10)-(3.12), we construct the eigenfunctions of the eigenvalue problem:

$$\frac{\partial}{\partial\sigma}\left(\mu\frac{\partial\phi}{\partial\sigma}\right) + \lambda\rho\phi(\sigma) = 0 \tag{3.13}$$

$$\mu\frac{\partial\phi}{\partial\sigma} = 0 \quad \text{on} \quad \sigma = 1 \ , \ \mu\frac{\partial\phi}{\partial\sigma} - \kappa h\bar{\rho}\phi = 0 \quad \text{on} \quad \sigma = 0 \tag{3.14}$$

For given μ and ρ the eigenpairs $\{\lambda_j, \phi_j(\sigma)\}$ can be computed numerically using the SLEIGN subroutine [see, Bailey, 1978]. At each point (x,y), they satisfy the orthogonality condition:

$$\int_0^1 \rho\phi_i\phi_j d\sigma = \begin{cases} 1 \ , & \text{when } i = j \\ 0 \ , & \text{when } i \neq j \end{cases} \tag{3.15}$$

Expanding the current profile in terms of the eigenfunctions, we obtain

$$U(\sigma) = \sum_{j\geq 1} c_j(x,y,t)\phi_j(\sigma) \tag{3.16}$$

where

$$c_j(x,y,t) = \int_0^1 \rho U(\sigma)\phi_j(\sigma) d\sigma \tag{3.17}$$

Multiplying (3.10) by $\phi_j(\sigma)$ and integrating from $\sigma = 0$ to 1, we get

$$\frac{\partial c_j}{\partial t} + (if + \frac{\lambda_j}{h^2})c_j = R_{1j}\left[\zeta_x + i\zeta_y\right] + R_{2j} + R_{3j} \tag{3.18}$$

where

$$R_{1j} = -g\int_0^1 \rho\phi_j d\sigma$$

$$R_{2j} = \int_0^1 \left[T^{(x)} + iT^{(y)}\right]\phi_j d\sigma$$

$$R_{3j} = \left(h^{-2} - H^{-2}\right)\lambda_j c_j$$

The initial values for the system of equations (3.18) can be obtained by assuming the motion starts from a state of rest, then $U|_{t=0} = 0$, and so

$$c_j\big|_{t=0} = 0 \tag{3.19}$$

The mass transports can be obtained by combining (2.12) and (3.16) as

$$p + iq = \sum_{j\geq 1} c_j(x,y,t)H\int_0^1 \rho\phi_j d\sigma \tag{3.20}$$

We can compute the steady currents caused by a given density field by solving equations (2.13) and (3.18) with appropriate boundary conditions and initial values. The staggered B-grid has been used in solving these equations. The advantages of using the B-grid scheme have been discussed in Lardner and Song (1990b). Using indices m and n in the x-direction and y-direction with spacings Δx and Δy respectively, we specify p, q and c_j at points (m,n), while ζ is specified at central points $(m+\frac{1}{2}, n+\frac{1}{2})$.

The spatial finite difference approximations to equations (2.13) and (3.18) are described as follows.

$$\rho^{(s)}\frac{\partial \zeta}{\partial t} + \overline{(\delta_x p)}^y + \overline{(\delta_y q)}^x = 0$$

$$\frac{\partial c_j}{\partial t} + \alpha_j c_j = R_{1j}\left\{\overline{(\delta_x \zeta)}^y + i\overline{(\delta_y \zeta)}^x\right\} + R_{2j} + R_{3j}$$

In these equations the following notation is used:

$$\alpha_j = k_j + if$$

$$k_j = h^{-2}\lambda_j^2$$

$$(\delta_x p)_{m,n} = \Delta x^{-1}\left(p_{m+\frac{1}{2},n} - p_{m-\frac{1}{2},n}\right)$$

$$(\overline{\beta}^x)_{m,n} = \frac{1}{2}\left(\beta_{m+\frac{1}{2},n} + \beta_{m-\frac{1}{2},n}\right)$$

with similar definitions for the y-direction.

The time differencing scheme used for above equations has been a leap-frog scheme which has the advantage of being explicit and also second order in the time step, though the size of the time-step is restricted by the CFL stability criterion. It is described in Lardner (1990), Lardner and Song (1990a, 1990b).

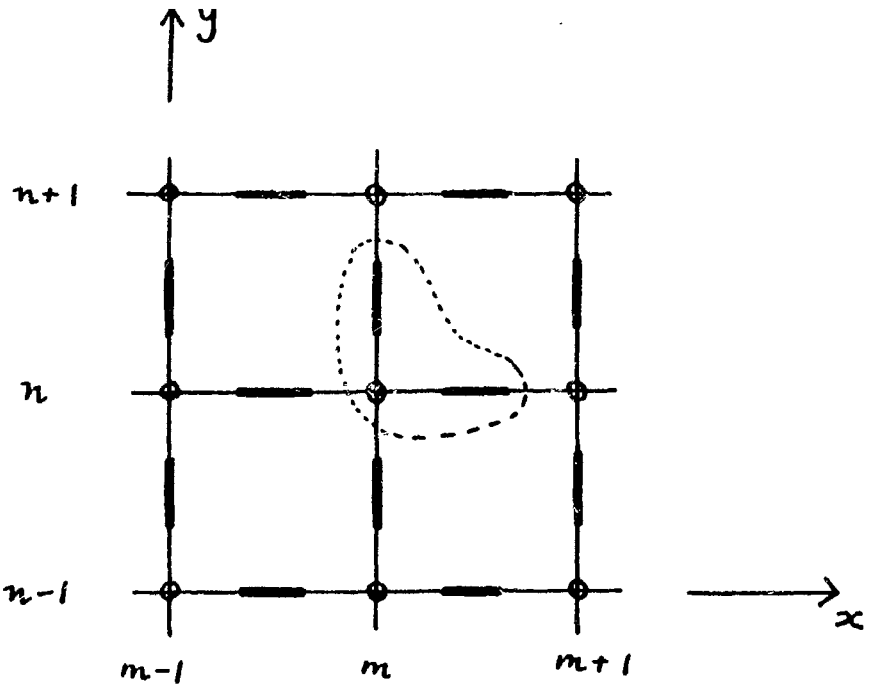

Fig. 3.1(a)

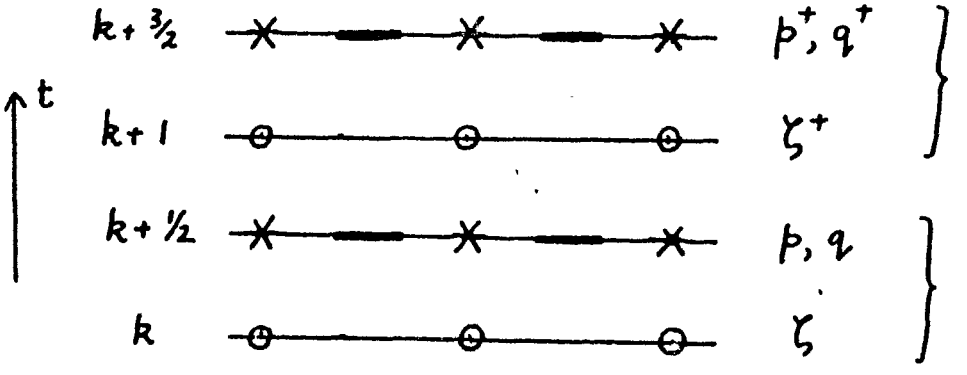

Fig. 3.1(b)

Fig. 3.1(a) The spatial grid: O indicates points where ζ is specified; ▬ indicates points where p is specified; ▮ indicates points where q is specified. The encircled three points correspond to $\zeta_{m,n}$, $p_{m,n}$ and $q_{m,n}$.

Fig. 3.1(b) The temperal grid: ζ is specified at integer time steps; p and q are specified at half-odd-integer time-steps. The stars indicate space-time points at which vertical profiles are computed.

CHAPTER 4 TEST PROBLEMS FOR SPLITTING AND SPECTRAL ALGORITHMS

The accuracy of the first algorithm was tested by using it to solve four problems for which the exact steady solutions can be calculated. These problems were designed to test the code's accuracy in handling four distinct physical features: horizontal gradient of density, vertical density variations, variable depth and Coriolis forces. The accuracy of the second algorithm was tested on the latter two problems.

For the first three problems, we consider a channel occupying the region $0 < x < l$ with the end $x = 0$ being closed and $x = l$ open. The eddy viscosity μ is assumed constant, evaporation is ignored ($W = 0$) and bottom drag is assumed linear ($\kappa_2 = 0$). Only longitudinal flow is considered, with v and f taken as zero.

For steady flow, equation (2.13) then reduces to $p_x = 0$, and since $p = 0$ at $x = 0$, it follows that $p = 0$ for all x. Therefore,

$$\int_0^1 \rho u \, d\sigma = 0. \tag{4.1}$$

Equation (2.5a) then reduces, for steady flow, to

$$(\mu u_\sigma)_\sigma = g\rho h^2 \zeta_x + gh^3 \frac{\partial}{\partial x}\int_\sigma^1 \rho(\sigma')d\sigma' - gh^2 \frac{\partial h}{\partial x}\int_\sigma^1 [\rho(\sigma) - \rho(\sigma')]d\sigma' \tag{4.2}$$

while the boundary conditions are

$$\mu u_\sigma = \begin{cases} 0 & \text{on} \quad \sigma = 1 \\ \bar{\rho} h \kappa \mu^{(b)} & \text{on} \quad \sigma = 0. \end{cases} \tag{4.3}$$

The depth-averaged momentum equation (2.14a) becomes

$$g\bar{\rho}h\zeta_x + \bar{\rho}\kappa\mu^{(b)} + gh^2 \frac{\partial}{\partial x}\int_0^1 \rho(\sigma)\sigma \, d\sigma + 2gh \frac{\partial h}{\partial x}\int_0^1 [\rho(\sigma) - \bar{\rho}]\sigma \, d\sigma = 0.$$

It is readily verified that this is not independent of the above equations, and it can be ignored.

The finite difference equations used for the numerical computations are the appropriately

simplified forms of equations (3.1), (3.2) and (3.8), and they will not be repeated here.

In the numerical results given below, the channel was taken with the closed end at grid-point $m = \frac{3}{2}$ and the open end at $m = 19$, the horizontal grid spacing being $\delta = 40{,}000$m.. The number of vertical levels was taken as $J = 10$. The other constants used were (in MKS units) $g = 9.81$, $\kappa_1 = 0.002$ and $N = 0.065$. The time step was $\tau = 360$s, with the computation being run until a steady solution was obtained. (Typically, this took about 3000 steps, corresponding to 12 days of real time.)

Two explicit density distributions have been examined for constant depth of 65 m. In the first of these, the density field has a strong horizontal gradient but no vertical gradient, while in the second there is vertical density gradient but the mean density has no horizontal gradient. Thus these two special cases distinguish between the effects of horizontal and vertical structure in the density fields, and the comparative flows in the two cases are in themselves quite interesting. A third problem with variable depth has also been examined.

4.1 **Model I** $\rho = \rho_0(1 - \beta x)$, h = constant

In this case, $\bar{\rho} = \rho$ and equation (4.2) takes the form

$$(\mu u_\sigma)_\sigma = g\rho h^2 \zeta_x - \beta\rho_0 g h^3(1 - \sigma)$$

After using the conditions (4.1) and (4.3), we obtain the solution

$$u = \frac{U}{1+4\kappa}\{1 + 12\kappa\sigma - 6(1+5\kappa)\sigma^2 + 4(1+4\kappa)\sigma^3\}$$

$$\zeta_x = \tfrac{1}{2}\beta h \frac{1+3\kappa}{1+4\kappa}$$

where

$$\kappa = \frac{\kappa_1 h\rho_0}{12\mu}, \qquad U = \frac{\beta g h^3 \rho_0}{24\mu}. \tag{4.4}$$

For the values $\rho_0 = 1035$ kg.m^{-3} and $\beta = 1.47\times10^{-8}$ m^{-1} (which gives a density variation from 1035 to 1025 kg.m^{-3} along the channel), the exact velocity solution is given in units of 0.1 mm/s. in the second column of Table 4.1. In this case, the flow is the same for all x. At the

upper surface there is strong inflow from the open end towards the closed end of magnitude about 20 mm/s while there is a corresponding outflow of somewhat lower magnitude near the bottom. (Near the closed end, there is, of course a boundary layer where the flow overturns, but the model is too simplified to pick this up.)

The computed steady velocity is given in the third column of Table 4.1. Clearly the numerical algorithm is very accurate.

j	Exact	Computed
11	−198	−199
9	−172	−172
7	−67	−68
5	59	59
3	151	151
1	151	153

Table 4.1. Exact and computed velocity profiles in units of 0.1 mm/s for flow in a channel with the density field of Model I. The level $j = 1$ corresponds to the bottom while the free surface is mid-way between $j = 10$ and $j = 11$. The flow is the same at all values of x.

4.2 **Model II** $\rho = \rho_0[1 + \beta x(1 - 2\sigma)]$, h = constant

In this case, $\bar{\rho} = \rho_0$ and equation (4.2) reduces to

$$(\mu u_\sigma)_\sigma = g\rho h^2 \zeta_x - \beta\rho_0 g h^3 \sigma(1 - \sigma)$$

with boundary conditions (4.3) as well as (4.1). The solution can be conveniently expressed in terms of the bottom velocity

$$u^{(b)} = -\frac{U}{15D}[1 + 5\beta x - 2(\beta x)^2]$$

where U and κ have the same meaning as in (4.4) and

$$D = 1 + 2\kappa[2 - \beta x + \tfrac{1}{5}(\beta x)^2]. \qquad (4.5)$$

Then

$$u = u^{(b)}\{1+6\kappa[2\sigma - \sigma^2 - \beta x\sigma^2(1-\tfrac{2}{3}\sigma)]\} + 2U\sigma^2[(1-\sigma)^2 + \beta x(1-\tfrac{2}{3}\sigma)]$$

$$\zeta_x = \tfrac{1}{6}\beta h\left\{1 - \frac{3\kappa u^{(b)}}{U}\right\}.$$

Again the values $\rho_0 = 1035$ kg.m^{-3} and $\beta = 1.47\times10^{-8}$ m^{-1} were used. In this case, the density on the free surface (in kg.m^{-3}) varies from 1025 at the open end to 1035 at the closed end while at the bottom it varies from 1035 at the closed end to 1045 at the open end. There is thus zero vertical density gradient at the closed end and maximum vertical gradient at the open end.

m:	4	10	16
j	u	u	u
11	−19	−18	−18
9	−11	−11	−11
7	9	9	9
5	13	13	13
3	0	0	0
1	−10	−10	−10

m:	4	10	16
j	u	u	u
11	−20	−20	−19
9	−12	−12	−11
7	8	8	9
5	13	13	13
3	1	0	0
1	−9	−10	−10

Table 4.2. Exact and computed velocity profiles, in units of 0.1 mm/s, for flow in a channel with the density field of Model II. The exact solution is given in the upper part of the table and the computed solution below. The profiles are given at three points along the channel, the leftmost profile being adjacent to the closed end of the channel and the rightmost adjacent to the open end.

The exact and computed velocities are given in units of 0.1mm/s. in Table 4.2. In this case, the flow is an order of magnitude smaller than for Model I, and varies slightly with x. Both at the upper surface and at the bottom there are inflows from the open end towards the closed end of approximate magnitudes 2 and 1 mm/s respectively, while there is a band of outflow of magnitude 1.3 mm/s near the middle of the water column. Again the computed solution is in very good agreement with the exact one. The absolute errors are about the same as those for Model I, though are larger in relative terms.

4.3 **Model III** $\rho = \rho_0[1 + \beta x(1 - 2\sigma)]$, $h = h(x)$

In this case, $\bar{\rho} = \rho_0$ again and equation (4.2) reduces to

$$(\mu u_\sigma)_\sigma = g\rho h^2 \zeta_x - \beta\rho_0 g\left[h^3\sigma(1-\sigma) + h^2 h' x\,(1-\sigma)^2\right].$$

Taking the conditions (4.1) and (4.3) into account, we obtain the bottom velocity

$$u^{(b)} = -\frac{U}{15D}[1 + 5\beta x - 2(\beta x)^2 - s(2 - \beta x)^2]$$

where U, D and κ have the same meaning as in (4.4) and (4.5) and $s = 4xh'(x)/h(x)$. The rest of the solution is given by

$$u = u^{(b)}\left\{1 + 6\kappa\left[2\sigma - \sigma^2 - \beta x\sigma^2(1 - \tfrac{2}{3}\sigma)\right]\right\}$$
$$+ 2U\sigma^2\left[(1-\sigma)^2 + (1 + \tfrac{1}{2}s)\beta x\,(1 - \tfrac{2}{3}\sigma) - \tfrac{1}{4}s(2-\sigma)^2\right]$$

$$\zeta_x = \tfrac{1}{6}\beta h\left\{1 + \tfrac{1}{2}s - \frac{3\kappa u^{(b)}}{U}\right\}.$$

For the example computed, the parameters were given the same values as for Model II except for the depth which was taken to increase uniformly from 35 m at the closed end of the channel to 95 m at the open end. Typical results are given in Table 4.3 which shows the exact and computed velocity profiles at three positions along the channel. The two solutions are again in very close agreement.

Comparing with Table 4.2, it is clear that depth variation has a very significant effect on the magnitude of the velocity, its vertical profile and its variation along the channel.

m:	4	10	16
j	u	u	u
11	-16	-96	-268
9	-13	-81	-227
7	-2	-25	-76
5	6	32	89
3	9	66	189
1	7	61	168

m:	4	10	16
j	u	u	u
11	-14	-93	-264
9	-11	-78	-223
7	-2	-24	-74
5	6	31	88
3	8	64	187
1	6	60	168

Table 4.3. Exact and computed velocity profiles at three points along the channel, in units of 0.1 mm/s, for flow in a channel with the density field of Model II and variable depth. The exact solution is given in the upper part of the table and the computed solution below.

Using the spectral algorithm the exact and the computed solutions at the same set of horizontal grid points are given in Table 4.4. As the figures indicate the accuracy is better in this case. It must be noted that the exact values shown in Table 4.3a is different from that shown in Table 4.4a. This is because the vertical levels do not coincide for the two algorithms.

m:	4	10	16
j	u	u	u
11	−17.3	−98.7	−269.6
9	−11.3	−71.4	−198.5
7	−0.5	−15.6	−49.0
5	7.2	37.2	101.3
3	9.3	66.1	186.8
1	7.4	60.9	167.5

m:	4	10	16
j	u	u	u
11	−17.7	−99.5	−271.0
9	−11.5	−71.4	−198.9
7	−0.5	−15.4	−47.3
5	7.5	37.8	102.5
3	9.5	66.5	187.0
1	7.6	60.1	167.3

Table 4.4 Exact and computed velocity profiles at three points along the channel, in units of 0.1 mm/s computed using the spectral algorithm.

4.4 **Model IV** Rectangular sea model

The fourth model is designed to test the accuracy of the computer code's treatment of the Coriolis terms. We consider a rectangular body of water of constant depth, occupying the region $0 < x < L$, $0 < y < M$, with lateral boundary conditions $p = 0$ on the sides $x = 0,L$ and q having certain prescribed values, to be given below, on the sides $y = 0,M$. W and κ_2 are again zero and f, μ and κ_1 constant. We suppose that the density $\rho(x)$ is a function of x only and that all flow variables are independent of y. In this case, eqns (2.5), for steady flow, reduce to

$$\begin{aligned} &(\mu u_\sigma)_\sigma + \rho h^2 f v - g\rho h^2 \zeta_x - g h^3 \rho'(x)(1-\sigma) = 0 \\ &(\mu v_\sigma)_\sigma - \rho h^2 f u = 0. \end{aligned} \tag{4.6}$$

The depth-averaged equations (2.14) become

$$-fq + g\rho h\zeta_x + \kappa_1 \rho u^{(b)} + \tfrac{1}{2} g h^2 \rho'(x) = 0, \qquad fp + \kappa_1 \rho v^{(b)} = 0. \tag{4.7}$$

The continuity equation reduces to $p_x = 0$, and in view of the lateral boundary conditions therefore, $p = 0$. Eqn (4.7b) then implies that $v^{(b)} = 0$, so that the boundary conditions associated with eqns (4.6) are:

$$u_\sigma = v_\sigma = 0 \quad \text{on} \quad \sigma = 1$$
$$v = v_\sigma = \mu u_\sigma - \kappa_1 h \rho u = 0 \quad \text{on} \quad \sigma = 0.$$

The general solution of eqns (4.6) has the form

$$(u, v) = \frac{gh\rho'}{f\rho}(\alpha, \beta), \qquad \zeta_x = \frac{h\rho'}{\rho}\gamma,$$

where

$$\alpha = e^{r\sigma}(a\cos r\sigma - b\sin r\sigma) + e^{-r\sigma}(c\cos r\sigma + d\sin r\sigma)$$
$$\beta = \gamma + 1 - \sigma + e^{r\sigma}(b\cos r\sigma + a\sin r\sigma) + e^{-r\sigma}(d\cos r\sigma - c\sin r\sigma)$$

with $r = \sqrt{\dfrac{\rho f h^2}{2\mu}}$. The terms involving $a,\ldots,d$ are of course an Ekman spiral type of solution. These constants as well as γ are determined from the above five boundary conditions, which take the form

$$\begin{bmatrix} 1 & 0 & 1 & 0 & 1 \\ 0 & 1 & 1 & -1 & -1 \\ 0 & \lambda - 1 & 1 & \lambda + 1 & -1 \\ 0 & -e^r\cos r & e^r\sin r & e^{-r}\cos r & e^{-r}\sin r \\ 0 & e^r\sin r & e^r\cos r & e^{-r}\sin r & -e^{-r}\cos r \end{bmatrix} \begin{bmatrix} \gamma + 1 \\ a \\ b \\ c \\ d \end{bmatrix} = \begin{bmatrix} 0 \\ 1/r \\ 0 \\ -1/2r \\ 1/2r \end{bmatrix}$$

where $\lambda = \dfrac{\kappa_1 h \rho}{\mu r}$. This matrix equation is solved numerically to construct the exact solution.

For the computed solution, we require the boundary values of q on $y = 0, M$, which are taken from the above exact solution. It is easily seen from the first of eqns (4.7) and the above solution that

$$q = \frac{gh^2\rho'}{f}\left[\gamma + \tfrac{1}{2} + \frac{\lambda}{2r}(a + c)\right].$$

The solution has been computed for a rectangle of dimensions 600 kms in the x -direction and 200 kms in the y -direction with a grid spacing of 20 kms. The density function and other parameters were taken as in Model I with the addition of $f = 1.22\times10^{-4}$ s^{-1}. Table 4.5 gives the exact and computed velocities at the centre point of the rectangle. There is very little variation of the final steady solution with x and the accuracy of the computed solution is about the same throughout the rectangle.

	Exact		Computed	
j	u	v	u	v
11	−165	255	−166	256
9	−142	240	−142	241
7	−55	175	−55	176
5	48	91	47	91
3	124	24	124	23
1	126	0	126	0

Table 4.5. Exact and computed velocity profiles in units of 0.1 mm/s at the centre point of a rectangle with the density field of Model I. The flow is the same at all values of y and is almost independent of x.

We present a part of the results obtained with the spectral algorithm in Table 4.6. The accuracy of the results are obviously somewhat better. (The discrepancy between the exact solutions given in Tables 4.5 and 4.6 is due to the difference between the Arakawa B and C grids used by the two algorithms.)

	Exact		Computed	
j	u	v	u	v
11	−169	257	−169	257
9	−129	231	−128	231
7	−40	164	−40	164
5	58	84	58	84
3	127	22	127	22
1	127	0	127	0

Table 4.6. Exact and computed velocity profiles at the B-grid point (15,9) in the rectangle region, in units of 0.1 mm/s.

CHAPTER 5 DENSITY DRIVEN FLOWS IN THE ARABIAN GULF

The residual currents in the Gulf have been attributed to two principal factors: wind-forcing which, coupled with Coriolis effects generates a net anti-clockwise circulation, and the effects of density gradients sustained by evaporation and radiative heat transfer and, to a lesser extent, by fresh water inflow at the head of the Gulf. The relative importance of these two mechanisms has been the subject of a certain amount of controversy in the literature. Hughes and Hunter (1980) argued that that wind-driven currents made the major contribution, but Hunter (1982) subsequently concluded that the circulation was probably dominated by density-driven flow, geostrophically balanced across the Gulf and frictionally balanced in the direction of flow. Galt and co-workers (1983) agree with this assessment in the southern half of the Gulf, but conclude that wind-driven circulation plus the effects of fresh-water inflow dominate in the northern half.

The computation of the wind-driven currents by Galt et al. (1983) was based on a two-dimensional depth-averaged model. Later, more detailed calculations were made by Lardner, Lehr, Fraga and Sarhan (1988a,b) of the vertical structure of the flow generated by the monthly averaged winds in the region, and it was found that the surface flow is considerably stronger and more uniform in direction than the depth-averaged flow. Furthermore, the magnitude of this surface current is consistent over most of the Gulf with the observed values found by Hunter (1982) from an analysis of ship-drift data as well as with more recent experimental drift-buoy studies in the North-West part of the region (Henaidi 1984). Subsequent simulation of some of the drift buoy movements, using actual wind measurements and a dynamical three-dimensional model has yielded good agreement with the observations.

An estimate of the density-driven currents was made by Lardner, Lehr, Fraga and Sarhan (1987) using a simple two-layer, sectionally integrated model, similar to that constructed by Pearson and Winter (1978) for the flow in fjords. It was found that the magnitude of this component of the surface flow is sufficient on its own to explain Hunter's empirical values (1982) within the Strait of Hormuz, but as one moves into the Gulf, the density-driven currents decrease rapidly and after about 100 kilometers they become appreciably smaller than the wind-driven currents. At the northern end of the Gulf, the density-driven effects are highly localized near the Shatt-al Arab, where substantial fresh water inflow occurs, but over most of this part of the region wind-forcing is the dominant factor.

It can be argued that the use of a sectionally integrated model tends to underestimate the local flow velocities, and in particular ignores the effects of Coriolis forces and channelling of the flow by the deeper trench parallel to the Iranian coast, both of which tend to concentrate the surface inflow towards the Iranian side of the Gulf, thus producing much larger surface currents on that side than those computed by Lardner et al (1987). Hunter's computations (1983) indicate such concentration of the flow and in fact show that the density-driven flow persists along the Iranian side with significant magnitude over much of the length of the Gulf.

Thus, there is agreement among the above authors that wind-forcing contributes significantly to and perhaps dominates the surface flow in the region adjacent to the Saudi coastline.and that within the Strait of Hormuz, the density-gradient effects are significant, or perhaps even dominant. Concerning the rest of the Gulf there is still disagreement, which we hope the results presented here will help resolve.

5.1 INPUT DATA

We have used the same horizontal grid and bathymetric data as used earlier (Lardner et al 1988a,b) for computation of the wind-driven currents and before that for tidal current modelling (Lardner et al 1982). The horizontal grid size is δ = 20,230m. and a time step τ = 240s. was found to be sufficiently small to produce a stable computation. In the vertical direction, 11 levels were used (J = 10 in the notation of chapter 3).

The basic equations contain terms involving gradients of the depth (the terms $T^{(x)}$ and $T^{(y)}$ in equations (2.5) and the terms $S^{(x)}$ and $S^{(y)}$ in equations (2.14)) and it was found that the large irregularities in the raw bathymetric data produce effects significant enough in some cases to swamp the average flow. It is unlikely that such localized eddies in the flow can be modelled in any realistic way with the coarse grid used and in particular with the deficiencies in the available data, so we eliminated them by making a preliminary smoothing of the bathymetric data.

The only consistent series of density measurements in the Gulf of which we are aware were made by the survey vessel Atlantis II during February and March, 1977 and reported by Brewer and co-workers (1978). Within the region modelled in the present work, measurements of density and other parameters were made at 43 stations, generally at depth intervals of 5 or 10m., for a total of 246 measurements. These measured data were smoothed by fitting

them to a polynomial in the variables m, n, and σ, yielding values of ρ on the three-dimensional grid of the numerical model. Contours of constant density for the smoothed data are shown in Figure 5.1(a) for the surface values and in Figure 5.1(b) for the values at the sea-bed. The detailed description of the method used to get the best fit values of the temperature, salinity and density values are given in the appendix at the end of this chapter. The accepted value (Lardner et al 1987) for the average velocity of evaporation in the Gulf is W = 1.44 metres per year.

Since the density-driven flow is a relatively small flow superimposed on larger tidal currents, we have considered it most appropriate to use a linear formula for the bottom friction in equation (2.9) (Hunter 1975). The effective linear drag coefficient experienced by the steady flow is given by the formula

$$\kappa_1 = (3/\pi)\kappa_2 |u_{tide}|$$

where u_{tide} is the amplitude of the tidal velocity and κ_2 is the actual quadratic coefficient.. For the Gulf, a typical value of u_{tide} is 0.2 m/s. Taking the quadratic drag coefficient κ_2 = 0.003, we are led to the value κ_1 = 0.0006 m^2/s.

The major ambiguity in the model centres around the choice of eddy viscosity function. Here, we chose a similar function to that used in the computation of the wind-driven currents (Lardner et al 1988a,b). In the following we let $N = \mu/\rho$ denote the kinematical eddy viscosity and N_s its surface value. Over the bulk of the water column, it is assumed that this is given by the Neumann-Pearson formula (1964)

$$N = 1.8 \times 10^{-4} V^{2.5} \qquad \text{(MKS units)}$$

where V is the wind speed. An analysis of wind data for the region (Anon. 1980) showed that the annual mean wind speed is $\bar{V} \approx 5$m/s. If an exponential distribution of wind speed is assumed, the mean value of $V^{2.5}$ is about $3\bar{V}^{2.5}$ and this leads to a bulk eddy viscosity N = 0.03 m^2/s. However, this argument neglects the suppressive effect on turbulence of density stratification, which is relatively stable in the Gulf, and we propose to use the value N = 0.01 m^2/s as best guess for this parameter.

Next, it is assumed that over the top ten metres of the water column, the eddy viscosity varies linearly from this bulk value N to a surface value N_s. The value of N_s is estimated, following the approach of Davies (1985a), as $N_s = k_0 u_* z_0$ where k_0 = 0.4 is von Karman's constant, z_0 is a roughness length and u_* is related to the mean surface shear stress, $\tau^{(s)}$

by the turbulent boundary layer equation $\tau^{(s)} = \rho u_*^2$. The roughness length is associated with the mean amplitude of surface waves and is taken as 0.3m. The mean surface shear stress, $\tau^{(s)}$ is computed from the wind data (Anon. 1980) using the formula of Lystad and Martinsen (1980) for the surface drag due to wind (see Mathison & Johansen 1983)) and is found to have the value $\tau^{(s)} = 6.46 \times 10^{-5}\,\rho$. This leads to $u_* = 8.0 \times 10^{-3}$ and $N_z = 0.001$ m^2/s.

The arguments leading to these values of κ_1, μ and μ_z are of course suspect. Hunter (1983) appears to have used the values $\kappa_1 = 0.0005$, $N = 0.005$ and $N_z = 0.005$ which differ somewhat from the values we have indicated. Because of this uncertainty, we have considered it essential to examine the sensitivity of the computed results to the choice of these three parameters, and this will be discussed.

5.2 RESULTS

5.2.1 Computed Flows due to Splitting Algorithm

In this section we shall report the results of the numerical computations, reserving their discussion to the next section. All figures relate to the steady flow, which is attained in the case of the Gulf after about 2000-2500 time steps, or 6-7 days of real time.

We begin by noting that the value used for the velocity of evaporation W was found to have an almost insignificant effect on the numerical results. The evaporation plays an essential role in establishing the density field, but once established, it is the density gradient rather than the evaporation that drives the flow.

The depth-averaged currents are similar for all choices of eddy viscosities and bottom friction coefficient. There is no net flow in or out of the Gulf in the steady state, and the depth-averaged flow consists of several large vortices. A typical picture is presented in the figure 5.2.

Figures 5.3(a) and 5.3(b) illustrate the currents at the free surface and at level 2* obtained using the values $N = 0.01$, $N_z = 0.001$, $\kappa_1 = 0.0006$, which, as discussed in the last section, represent the most reasonable estimates for these parameters. As anticipated, the dominant feature of the flow is an inflow in the upper layers of the water column from the Strait of

* Level 2 is 10.5% of the way from the bottom to the top of the water column.

Hormuz towards the Northern and Western portions of the Gulf and a compensating outflow in the lower layers. The transition from inflow to outflow occurs at most of the horizontal grid points between levels 5 and 7 (figures 5.4(a), 5.4(b) and 5.4(c)), that is, in the middle 20% of the water column.

Beyond this broad picture, however, the computed flows show a number of unexpected features, both in direction and magnitude. The main stream of surface inflow does not stay close to the Iranian shore, but rather proceeds in a Westerly direction, across the Gulf and north of the tip of the Qatar peninsula, and thence towards the mid-section of the Saudi coast. The maximum velocity of this surface inflow is about 18 cm/s within the Strait, but it decreases within 100 km to the range 9-12 cm/s and by the time the flow reaches Qatar it has diminished to about 4 cm/s. In the Southern portion of the Gulf, between Qatar and the Emirates, there is a uniform pattern of Westerly to South-Westerly surface inflow with magnitude diminishing to very small values after 250-300 kms from Hormuz.

On the Iranian side, within the Strait of Hormuz, the flow is confused, the surface inflow occuring 20-40 kms offshore for the first 250 kms into the Gulf. This area of confused flow occurs regardless of the choice of open boundary condition and it is worth noting that it has also been reported by Hunter (1983) in related calculations. Its cause may lie in the extensive region of relatively shallow water that occurs on that side of the Strait but may also be caused by a deficiency in the algorithm used (see below). Along the North-East portion of the Iranian coast the surface flow for almost the last 250 kms is directed towards the coast with the flow velocities of about 2 cm/s.

This pattern of flow is repeated with reducing magnitude of the velocities as one moves down the water column until reversal of the pattern occurs around level 6. The maximum reverse flow occurs generally at level 2 (see Figure 5.3(b)). Over most of the region, this flow is about opposite in direction to the surface inflow and with velocities generally about half the magnitude of those on the surface. There are however two significant exceptions to this. From the Qatar peninsula to the mid-Saudi coast, there is a slow Westerly bottom flow, parallel to the surface flow, this flow then sweeping to the north to join the main outflow. And along the Emirates coast close to Hormuz, the inflow persists at all levels of the water column, though the velocities at the bottom are very small.

In order to test the sensitivity of the computed velocities to the particular choices of the physical parameters, we have made numerical experiments with smaller values of eddy

viscosities and bottom drag. The following summarizes the effect of reducing these parameters.

(i) $N = 0.01$, $N_z = 0.001$, $\kappa_1 = 0.0012$

We have used this case as a benchmark against which to measure the effects of parameter changes. (Note the different value of κ_1.)

(ii) $N = 0.01$, $N_z = 0.001$, $\kappa_1 = 0.0005$

This case is to examine the effect of smaller bottom friction. The effect on surface flow is generally quite small, the main exception being in the Strait of Hormuz where the maximum inflow velocity is increased by 10% . There is a somewhat larger effect of this parameter on velocities at the lower levels.

(ii) $N = 0.01$, $N_z = 0.0001$, $\kappa_1 = 0.0012$

This case is to examine the effect of smaller surface eddy viscosity. The effect of this change is to increase the surface velocities by a very small amount, generally less than 5%, with even less change on the bottom velocities. In this regard, the density-driven flow is unlike a wind-driven flow, for which surface velocities are particularly sensitive to N_z (Davies 1985; Lardner & Cekirge 1987).

(iii) $N = 0.005$, $N_z = 0.001$, $\kappa_1 = 0.0012$

This case is to examine the effect of smaller bulk eddy viscosity. This parameter has the most significant effect on the flow. With the above values, the maximum inflow velocity was 16% greater than that in Case (i), and generally both the surface and bottom velocities are increased by about this amount, with some modification also of the direction of flow.

(iv) $N = 0.003$, $N_z = 0.0001$, $\kappa_1 = 0.0005$

We have seen in the above experiments that the effect of reducing the values of the three parameters is generally to increase the flow velocities. This final choice represents about the smallest reasonable set of values for the parameters and hence provides what is probably an upper bound for the magnitude of the density-driven flow. The computed currents at the surface and level 2 are shown in Figures 5.5(a) and (b). The pattern of the flow is almost the same as that in Figures 5.3(a) and (b),

with small differences in direction in some areas. The magnitudes of the velocities are increased over those shown in Figure 5.3 by generally 10-20%. The maximum velocity of surface inflow is 20 cm/s while the flow velocity off the Qatar peninsula is about 4 cm/s.

5.2.2 Computed Flows due to Spectral Algorithm

Figures 5.6(a), 5.6(b) and 5.6(c) illustrate the currents at the free surface, at level 2 and depth averaged current obtained using these values $N = 0.01$, $N_z = 0.001$, $\kappa = 0.0006$. With one notable exception (see below), the flow is virtually identical to that reported in 5.2.1, and reaffirms certain unexpected features found there. In particular, the main stream of surface inflow does not stay close to the Iranian shore, but rather proceeds in a Westerly direction, across the Gulf and north of the tip of the Qatar peninsula, and thence towards the mid-section of the Saudi coast. The maximum velocity of this surface inflow is about 16 cm/s within the Strait, but it decreases within 100 km to the range 7-10 cm/s and by the time the flow reaches Qatar it has diminished to about 3 cm/s. In the Southern portion of the Gulf, between Qatar and the Emirates, there is a uniform pattern of Westerly to South-Westerly surface inflow with magnitude diminishing to very small values after 250-300 kms from Hormuz.

On the Iranian side, the surface flow is directed predominantly onshore along virtually the whole coast, with magnitudes decreasing from 15 cm/s in the Strait of Hormuz to 2-4 cm/s along the North-Eastern portion of the coast.

It was found in 5.2.1 (and also earlier by Hunter(1983)) that the surface flow near the Iranian coast for the first 250 kms into the Gulf was confused. In 5.2.1, this was ascribed to the extensive area of shallow water that lies in that location. However, the present spectral algorithm yields a completely regular flow there, and it now seems likely that the origin of the confused flow lies in the inability of the earlier finite difference algorithms to deal accurately with a situation of rapidly shelving depths adjacent to an open boundary.

This pattern of the surface flow is repeated with reducing magnitude of the velocities as one moves down the water column until reversal of the pattern occurs around the middle depth level. The maximum reverse flow occurs generally at a level about 10% from the bottom (see Figure 5.6(b)). Over most of the region, this flow is about opposite in direction to the surface inflow and with velocities generally about half the magnitude of those on the surface. There is

however a significant exception to this. From the Qatar peninsula to the mid-Saudi coast, there is a slow Westerly bottom flow, parallel to the surface flow, this flow then sweeping to the north to join the main outflow. Along the Iranian coast, the bottom flow is offshore, with magnitude generally equal to or even exceeding the onshore surface flow.

The depth-averaged flow, consisting of several large gyres, is shown in Figure 5.6(c). Velocities are generally much smaller than surface velocities.

We have again conducted certain experiments to test the sensitivity of the predicted flow to choice of these parameters. We have re-computed the flow with all the parameters reduced by half, to N=0.005 m^2/s, N_s = 0.0005 m^2/s and κ = 0.0003 m/s. It is not likely that these parameters could be smaller than this. The general pattern of flow turns out to be the same as that shown in Figures 5.6(a)-5.6(c), with the magnitudes of the velocities increased by 20-40%. In particular, the maximum velocity of surface inflow in the Strait of Hormuz is increased to 20 cm/s.

5.3 DISCUSSION AND SUMMARY

The computed steady-state flow shows an expected pattern, consisting of inflow into the Gulf in the upper layers of the water column and a balancing outflow in the lower layers. The detailed results however show several unexpected features. One of these is that the main stream of surface inflow does not flow along the Iranian shoreline, but rather follows a Westerly course from Hormuz to the Qatar peninsular then continues towards the Saudi coast (see Figures 5.3(a), 5.5(a) and 5.6(a)). Between this line of flow and the Emirates coast, the Westerly surface flow persists but with diminishing magnitude. Along the North-Easterly part of the Iranian coast the surface flow is directed towards the coast.

The most significant result concerns the magnitude of the velocities, which turn out to be much smaller than has been suggested by some authors. The surface velocities within the Strait of Hormuz have a maximum value of about 16 cm/s if one uses what we have taken as the most plausible values for eddy viscosities and bottom drag coefficient, or about 20 cm/s if one uses the smallest reasonable values of these parameters. These values are smaller than the empirical residual velocities estimated by Hunter (1982) on the basis of ship-drift reports. Furthermore, the computed velocities decrease within a distance of 100 kms into the Gulf to 7-10 cm/s, smaller by a factor of 3 or 4 than the empirical estimates.

Previous calculations of surface velocities caused by average winds (Lardner et al 1988a,b) have shown that they are consistent in magnitude with Hunter's estimates over most of the Gulf. Thus, we are lead to conclude that the dominant factor in generating residual flow in most of the Gulf is wind-forcing rather than density gradient, the only exception being probably within the Strait of Hormuz.

The velocities computed in this chapter are very similar in magnitude to those calculated earlier (Lardner et al 1987) on the basis of a simple two-layer, sectionally averaged model of the flow. Comparing them with the velocities computed by Hunter using a three-dimensional model (Hunter 1983), however, our velocities appear to be somewhat smaller within the Strait of Hormuz and significantly smaller, generally by a factor of 2 to 3, within the Gulf itself. Hunter's results in particular show a significant surface flow parallel to the Iranian coast whereas ours show a much smaller flow directed on the surface towards that coast. The origin of the discrepancy between these two sets of results may lie in the approximations of Hunter's model or may be caused by different input data for the density field or the bathymetry, but since few details of the analysis are given in reference (Hunter 1983), it is difficult to draw any firm conclusion on this point.

Our conclusions regarding the relative significance of the density-driven residual flow in the Gulf must be tempered by the remark that the density data we used was gathered during the Winter season, and presumably the density gradients during Summer would be significantly greater than those measured, leading to greater velocities during that season. However it does not seem likely that the velocities could be sufficiently increased that they would approach those caused by the wind.

APPENDIX A

A major geochemical, biological and geophysical survey of the Persian Gulf and adjacent waters was carried out on in February and March of 1977 by Peter Brewer et al (1978). They obtained chemical oceanographic data from which the density values have been used to estimate the flow driven by density gradient in the Gulf as presented in Chapter 5.

As reported by Peter Brewer et al (1978) the data were obtained at several hydrographic stations situated at various points in the Persian Gulf. Hence the measurements were taken at locations which had different latitude and longitude. At each particular point the data were charted at different depths from the water surface. This means that the observations were a function of the coordinates of the station as well as the depth.

If the latitude and longitude of a particular station were represented by x- and y-coordinates and the depth by the z-coordinate, then we approximate the measurements by a polynomial of degree N of the form

$$\sigma_t = f(x,y,z) = \sum_{k=0}^{N} \sum_{j=0}^{N-k} \sum_{i=0}^{N-k-j} a_{ijk} x^i y^j z^k \qquad (A.1)$$

where σ_t = (density – 1000) in MKS units.

We are now given values of the three independent variables x,y and z at the data points and corresponding values of the dependent variable f and we wish to fit to the latter by least squares a third degree polynomial in x, y and z.

In all there are twenty terms in the polynomial corresponding to N=3. Now we outline the least squares method employed to do the data fit. The aim is to get the best-fit coefficients of each of the terms in the third degree polynomial such that it approximates reasonably the data values. Determining what order polynomial will yield the best fit to the data depends on the criteria that one uses in defining best fit. For example, equation (A.1) can be solved for successive higher order fits either to some maximum order or until the residuals have been minimized to below a specified error tolerance. In our case we also experimented with fourth and fifth degree polynomials and came to conclusion that the third degree fit was the best.

This decision was based on the fact that oscillations were appearing in the curve between adjacent data points, near the ends of the range.

A.1 LEAST SQUARES METHOD

Consider the problem of finding a vector $x \varepsilon R^n$ such that $Ax = b$ where $A \varepsilon R^{m \times n}$ and $b \varepsilon R^m$ are given and $m>n$. This is an overdetermined system of equations and usually has no exact solution, unless b is an element of $R(A)$, a proper subspace of R^m.

This suggests that we strive to minimize $\|Ax - b\|_p$ for some suitable choice of p. For $p=2$ this function is a continously differentiable function of x. One tactic for solution is to convert the original least squares problem into an equivalent, easy-to-solve problem using orthogonal transformations. The basic idea is to use one of the many orthogonal transformations (Golub and Van Loan, 1983) to compute the factorization $A = QR$, where Q is orthogonal and R is upper triangular.

Suppose that an orthogonal matrix $Q \varepsilon R^{m \times m}$ has been computed such that

$$Q^T A = R = \begin{bmatrix} R_1 \\ 0 \end{bmatrix} \begin{matrix} n \\ m-n \end{matrix} \qquad (A.2)$$

is upper triangular. If

$$Q^T b = \begin{bmatrix} c \\ d \end{bmatrix} \begin{matrix} n \\ m-n \end{matrix}$$

then

$$\|Ax - b\|_2^2 = \|Q^T Ax - Q^T b\|_2^2 = \|R_1 x - c\|_2^2 + \|d\|_2^2$$

for any $x \varepsilon R^n$. Clearly, if rank(A) = rank$(R_1) = n$, then x_{LS} is defined by the upper triangular system $R_1 x_{LS} = c$. $\|d\|_2^2$ represents the minimum sum of squares. Thus, the full rank LS problem can be readily solved once we have computed (A.2), which we refer to as the *Q-R factorization*. We have used the Householder's orthogonalization procedure (pp. 146-153, Golub & Van Loan, 1983) to factor the matrix A into the Q and R matrix.

A.2 BEST FIT VALUES

In our case the matrix x represents the coefficients of the terms in the fitting polynomial and the elements of the matrix A are the terms themselves. There are 43 stations in all and 225 observation points. Hence, $A \in R^{225\times20}$ and $x \in R^{20}$. We also obtained the best fit values to the temperature and salinity data. These are depicted as contours of constant density σ_t, temperature and salinity on the surface and at the bottom in figures 5.1(a), 5.1(b), 5.7(a), 5.7(b), 5.8(a) and 5.8(b). These contour plots match very well with those presented by Brewer et al (1978). The best fit coefficients for the three data sets are given in Table 5.1.

In the table the coefficients are denoted by $A(1)$,.....,$A(20)$ are the coefficients of the terms involving $1, x, y, \sigma, x^2, y^2, \sigma^2, xy, y\sigma, \sigma x, x^3, y^3, \sigma^3, x^2y, x^2\sigma, xy^2, x\sigma^2, xy\sigma, y\sigma^2$ and $y^2\sigma$ respectively. Here σ is defined in Chapter 2, x is latitude and y is longitude.

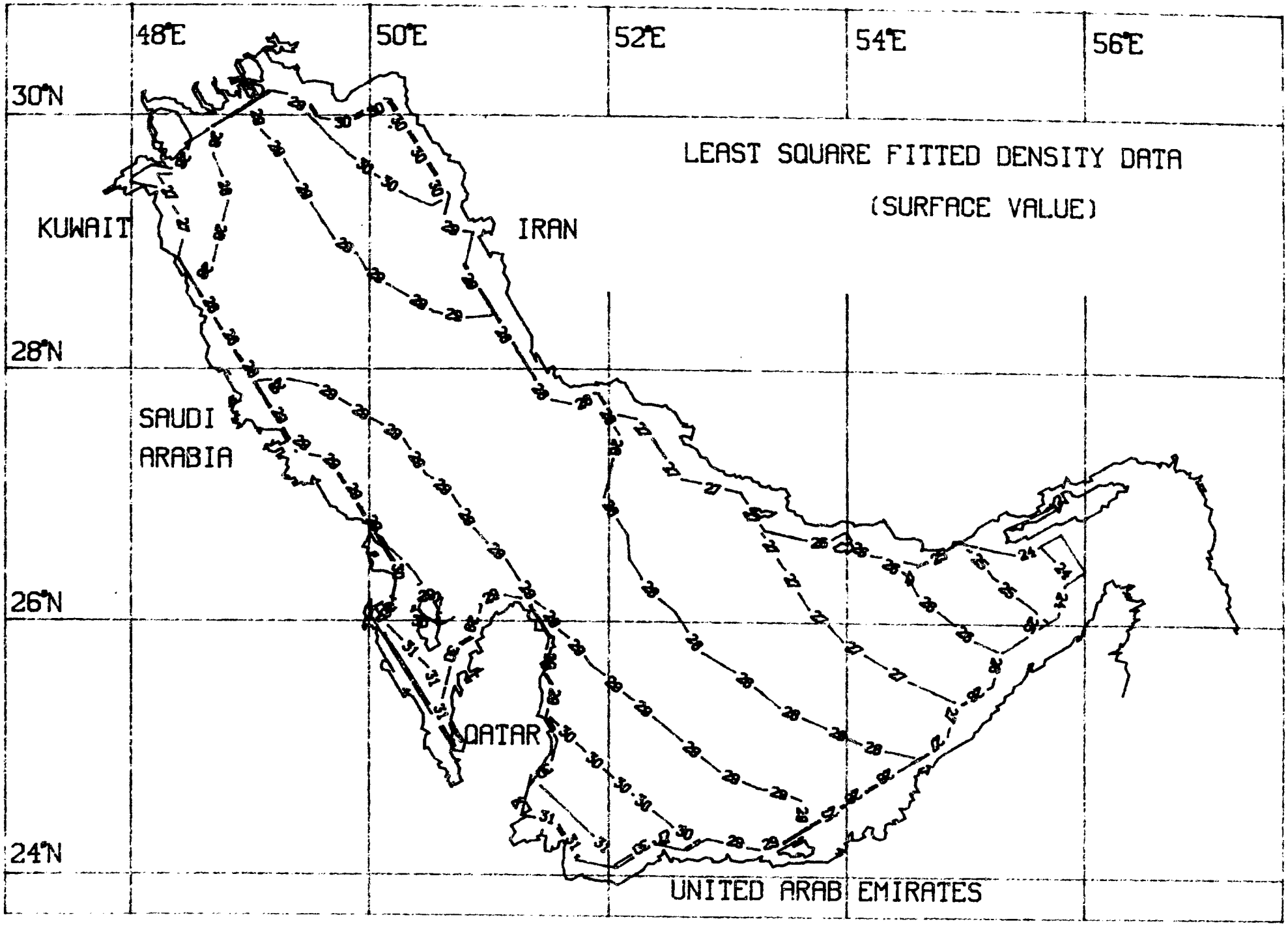
48°E
50°E
52°E
54°E
56°E
30°N
28°N
26°N
24°N
LEAST SQUARE FITTED DENSITY DATA
(SURFACE VALUE)
KUWAIT
IRAN
SAUDI
ARABIA
QATAR
UNITED ARAB EMIRATES

Figure 5.1(a)

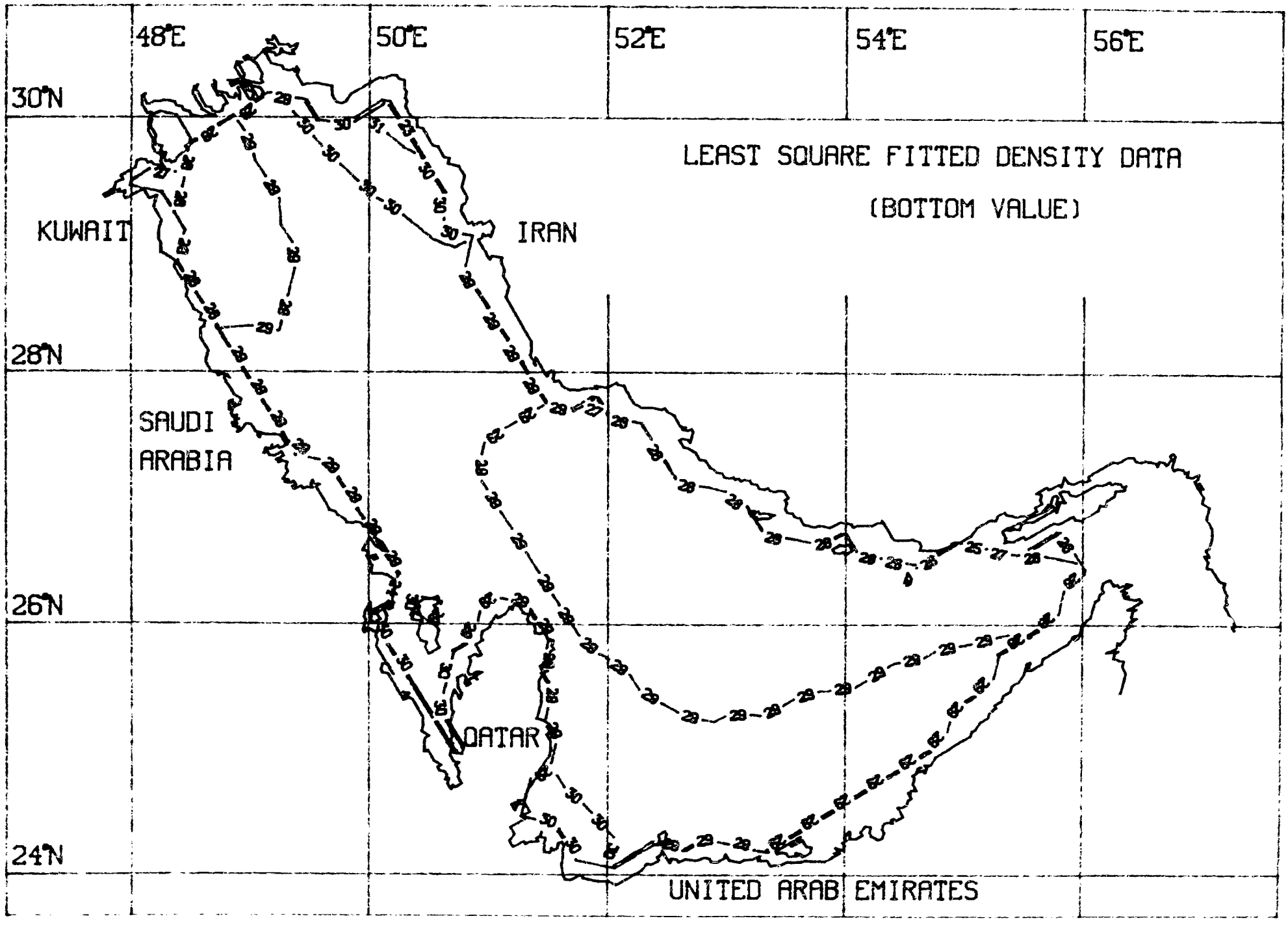
48°E
50°E
52°E
54°E
56°E
30°N
28°N
26°N
24°N
LEAST SQUARE FITTED DENSITY DATA
(BOTTOM VALUE)
KUWAIT
IRAN
SAUDI
ARABIA
QATAR
UNITED ARAB EMIRATES

Figure 5.1(b)

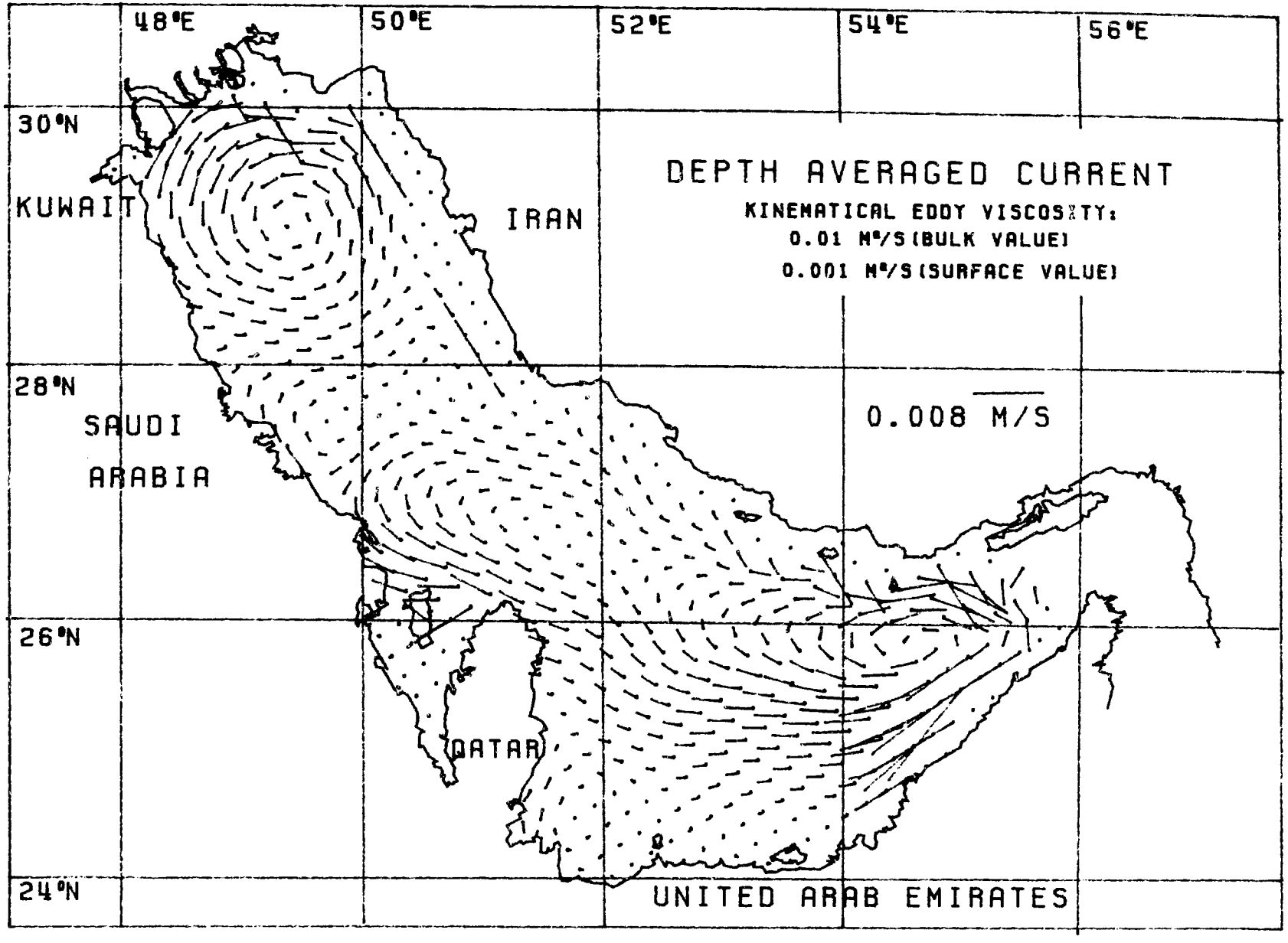
48°E
50°E
52°E
54°E
56°E
30°N
28°N
26°N
24°N
KUWAIT
IRAN
SAUDI
ARABIA
QATAR
UNITED ARAB EMIRATES
DEPTH AVERAGED CURRENT
KINEMATICAL EDDY VISCOSITY:
0.01 M²/S (BULK VALUE)
0.001 M²/S (SURFACE VALUE)
0.008 M/S

Figure 5.2

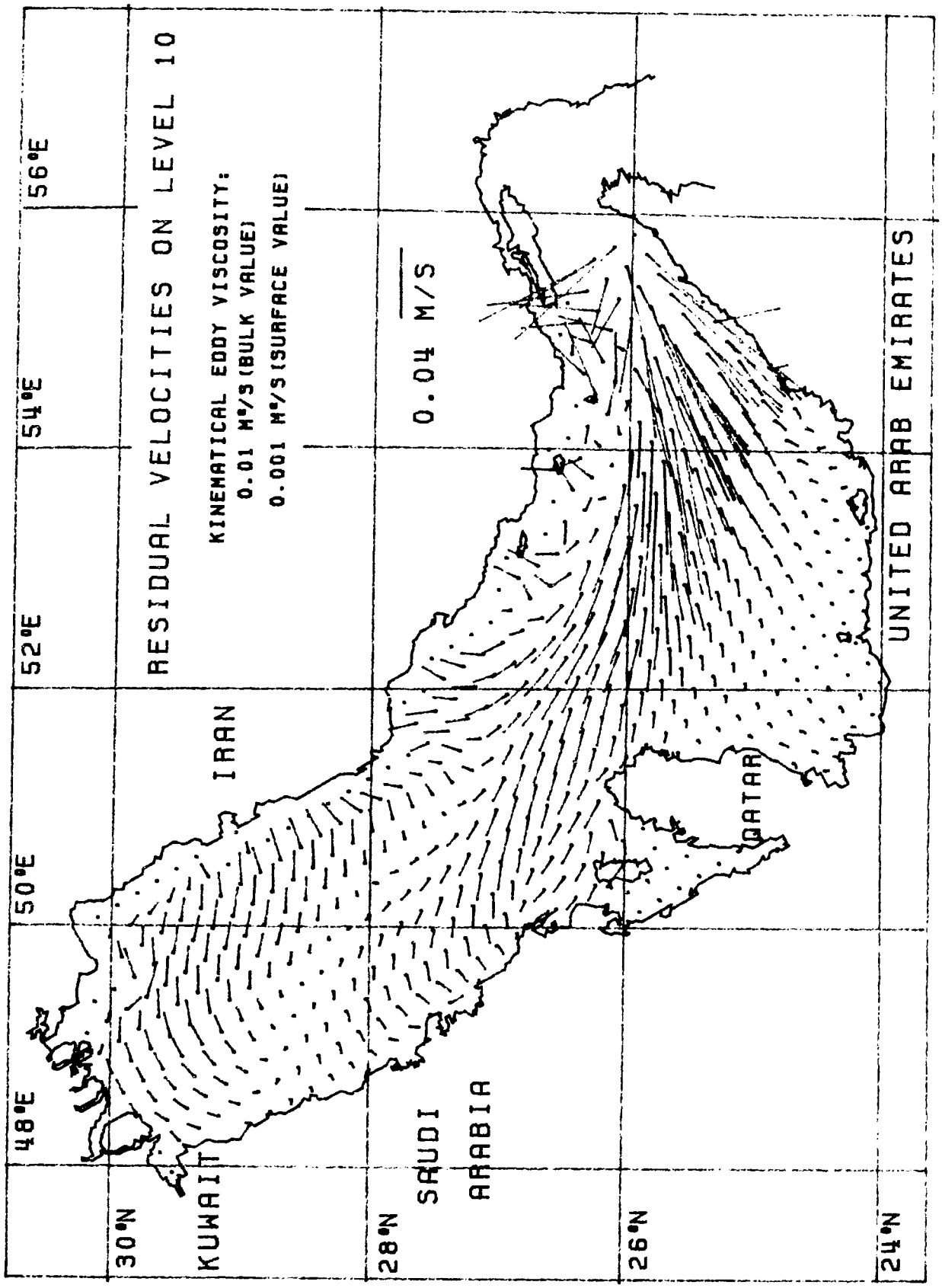
RESIDUAL VELOCITIES ON LEVEL 10
KINEMATICAL EDDY VISCOSITY:
0.01 M*/S (BULK VALUE)
0.001 M*/S (SURFACE VALUE)
0.04 M/S
48°E
50°E
52°E
54°E
56°E
30°N
28°N
26°N
24°N
KUWAIT
IRAN
SAUDI ARABIA
QATAR
UNITED ARAB EMIRATES

Figure 5.3(a)

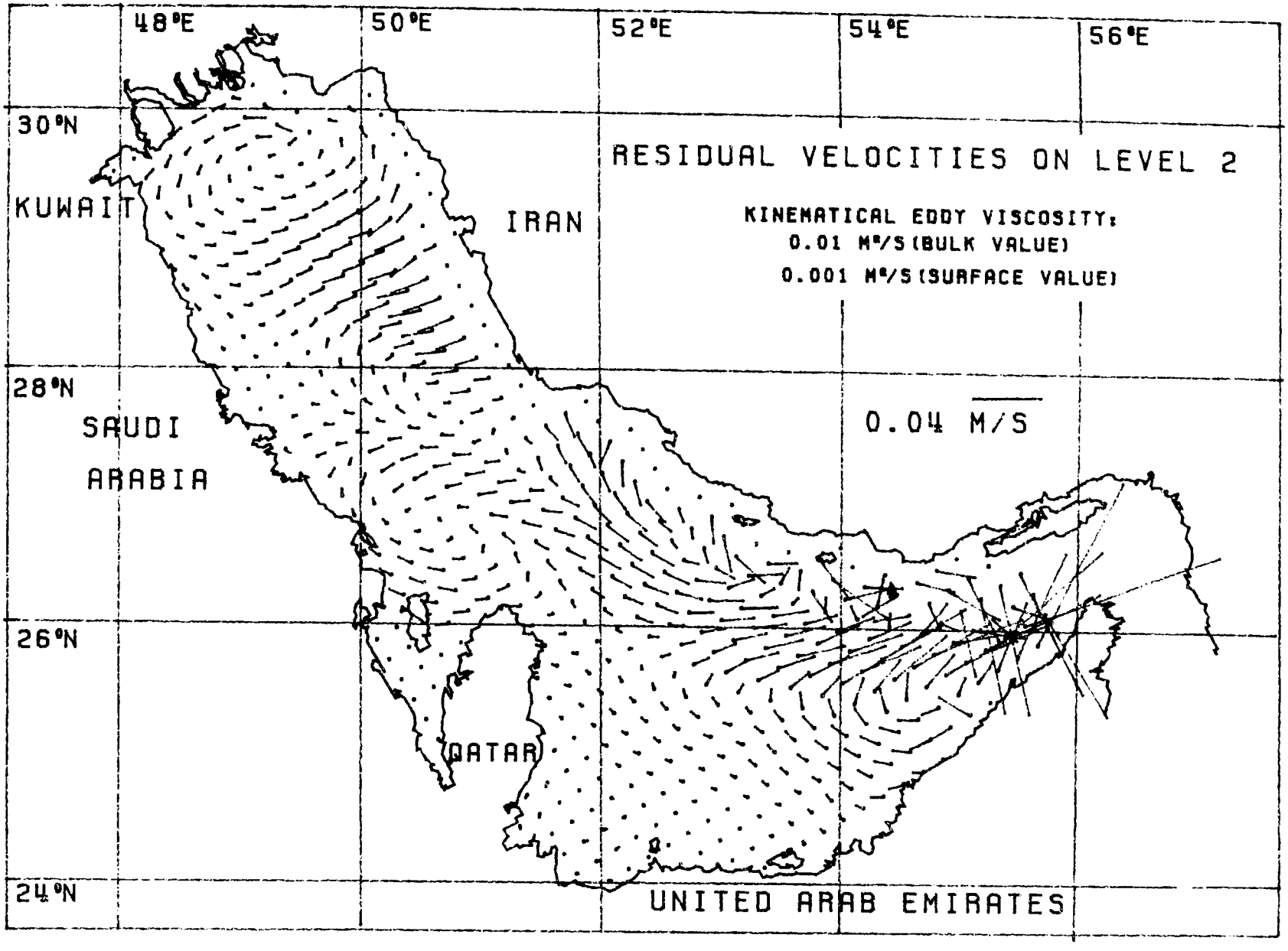
48°E
50°E
52°E
54°E
56°E
30°N
28°N
26°N
24°N
KUWAIT
IRAN
SAUDI
ARABIA
QATAR
UNITED ARAB EMIRATES
RESIDUAL VELOCITIES ON LEVEL 2
KINEMATICAL EDDY VISCOSITY:
0.01 M²/S (BULK VALUE)
0.001 M²/S (SURFACE VALUE)
0.04 M/S

Figure 5.3(b)

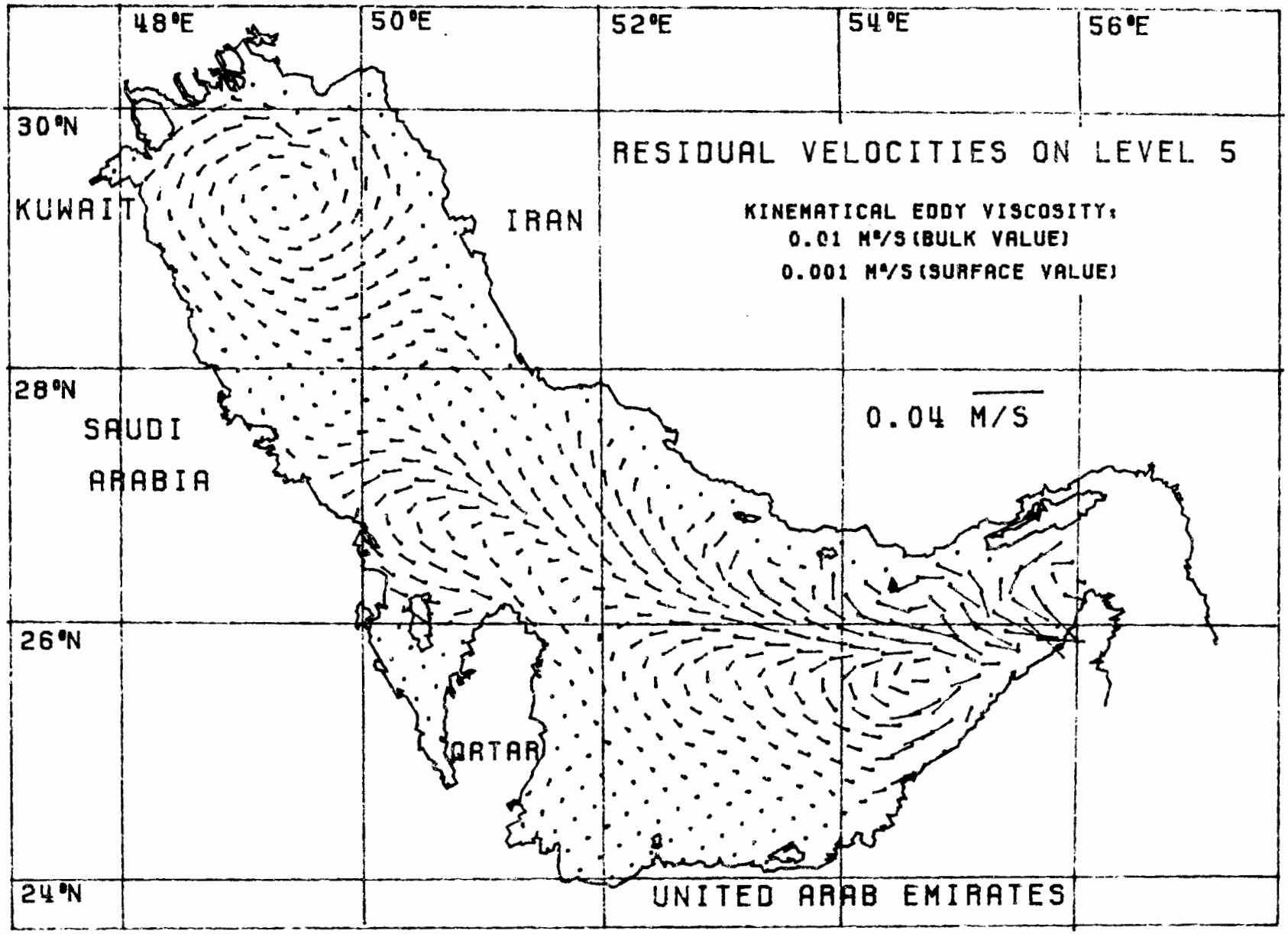
48°E
50°E
52°E
54°E
56°E
30°N
28°N
26°N
24°N
KUWAIT
IRAN
SAUDI
ARABIA
QATAR
UNITED ARAB EMIRATES
RESIDUAL VELOCITIES ON LEVEL 5
KINEMATICAL EDDY VISCOSITY:
0.01 M²/S (BULK VALUE)
0.001 M²/S (SURFACE VALUE)
0.04 M/S

Figure 5.4(a)

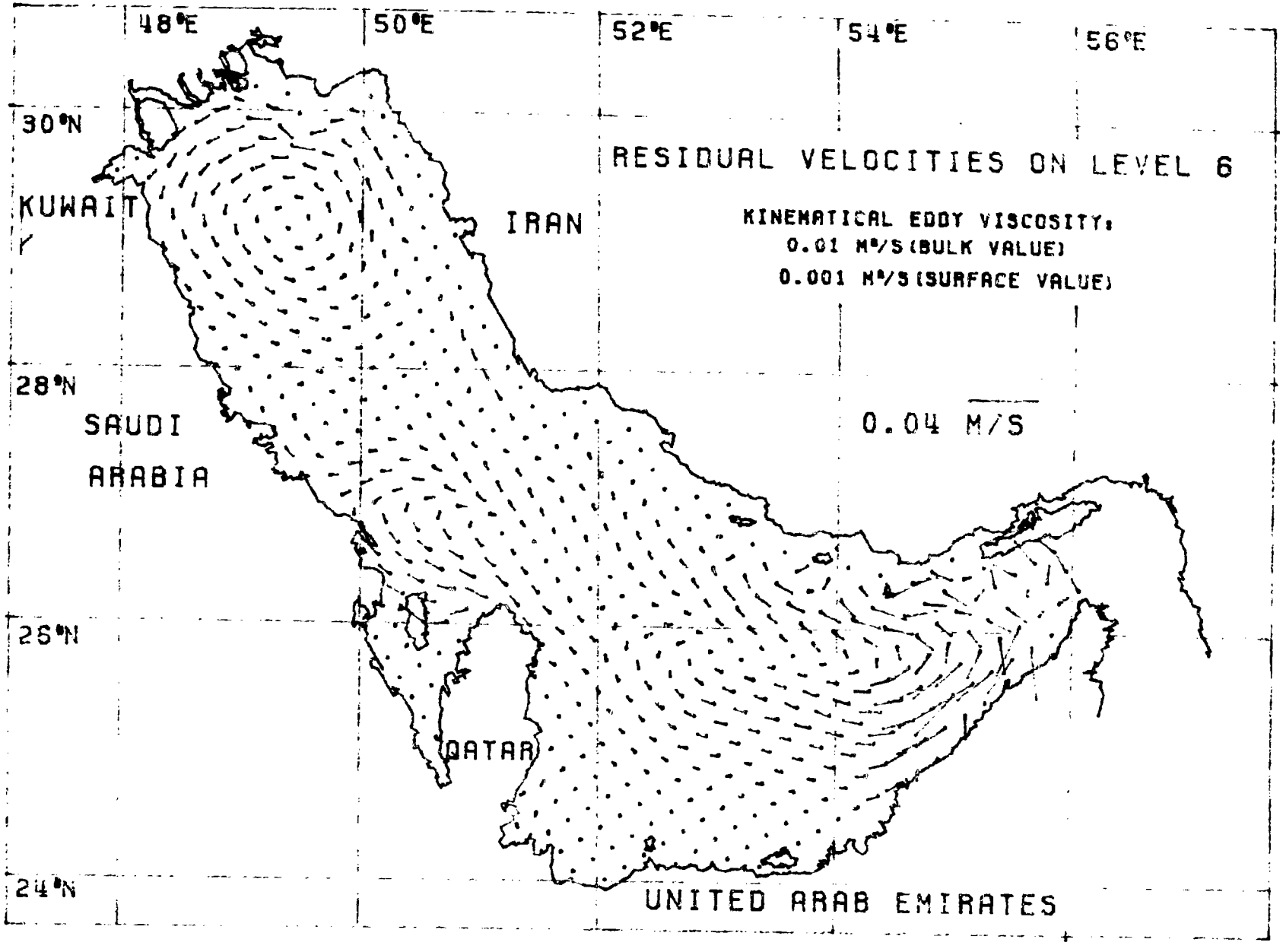
48°E
50°E
52°E
54°E
56°E
30°N
28°N
26°N
24°N
KUWAIT
IRAN
SAUDI
ARABIA
QATAR
UNITED ARAB EMIRATES
RESIDUAL VELOCITIES ON LEVEL 6
KINEMATICAL EDDY VISCOSITY:
0.01 M²/S (BULK VALUE)
0.001 M²/S (SURFACE VALUE)
0.04 M/S

Figure 5.4(b)

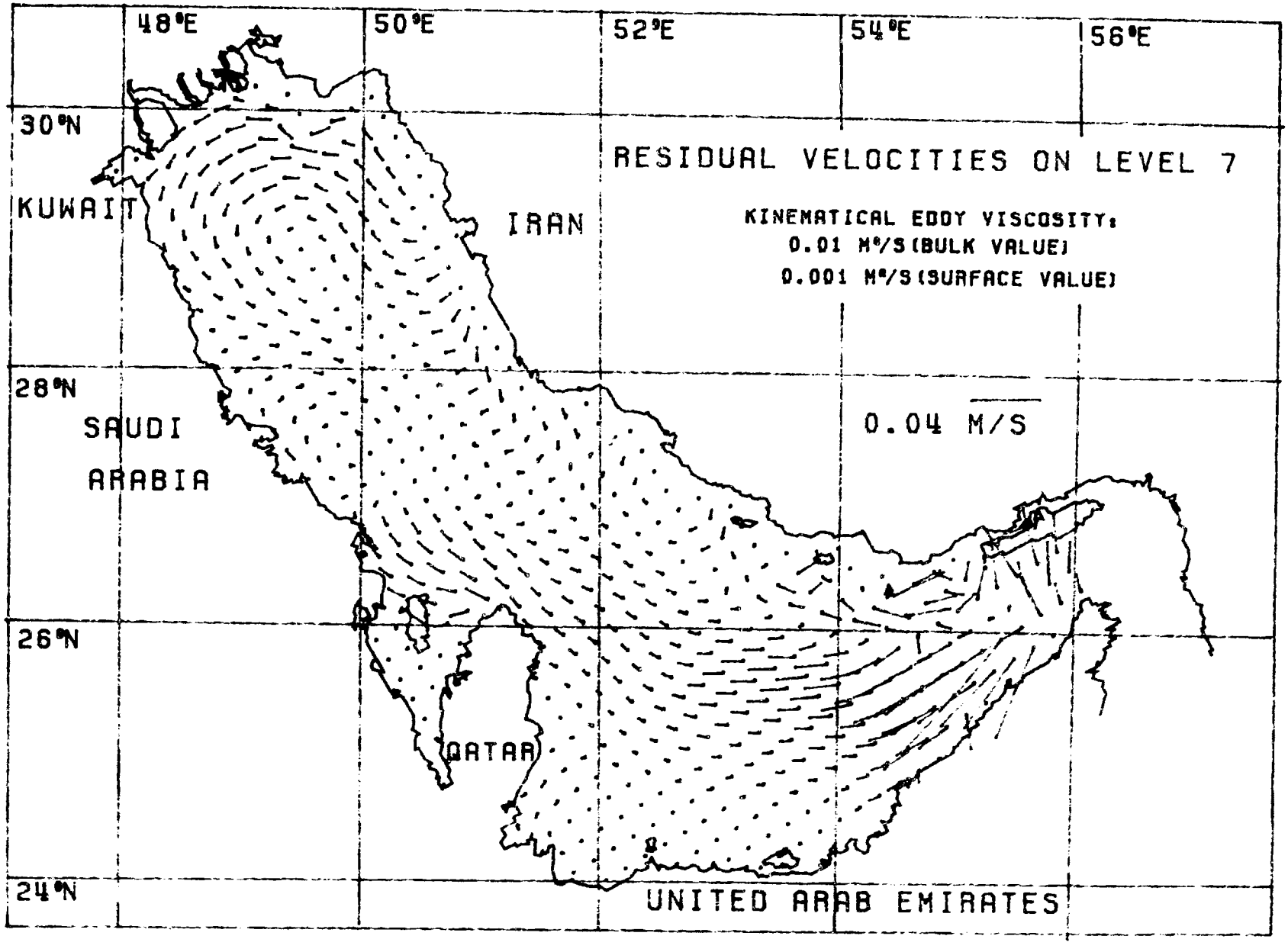
48°E
50°E
52°E
54°E
56°E
30°N
28°N
26°N
24°N
KUWAIT
IRAN
SAUDI
ARABIA
QATAR
UNITED ARAB EMIRATES
RESIDUAL VELOCITIES ON LEVEL 7
KINEMATICAL EDDY VISCOSITY:
0.01 M²/S (BULK VALUE)
0.001 M²/S (SURFACE VALUE)
0.04 M/S

Figure 5.4(c)

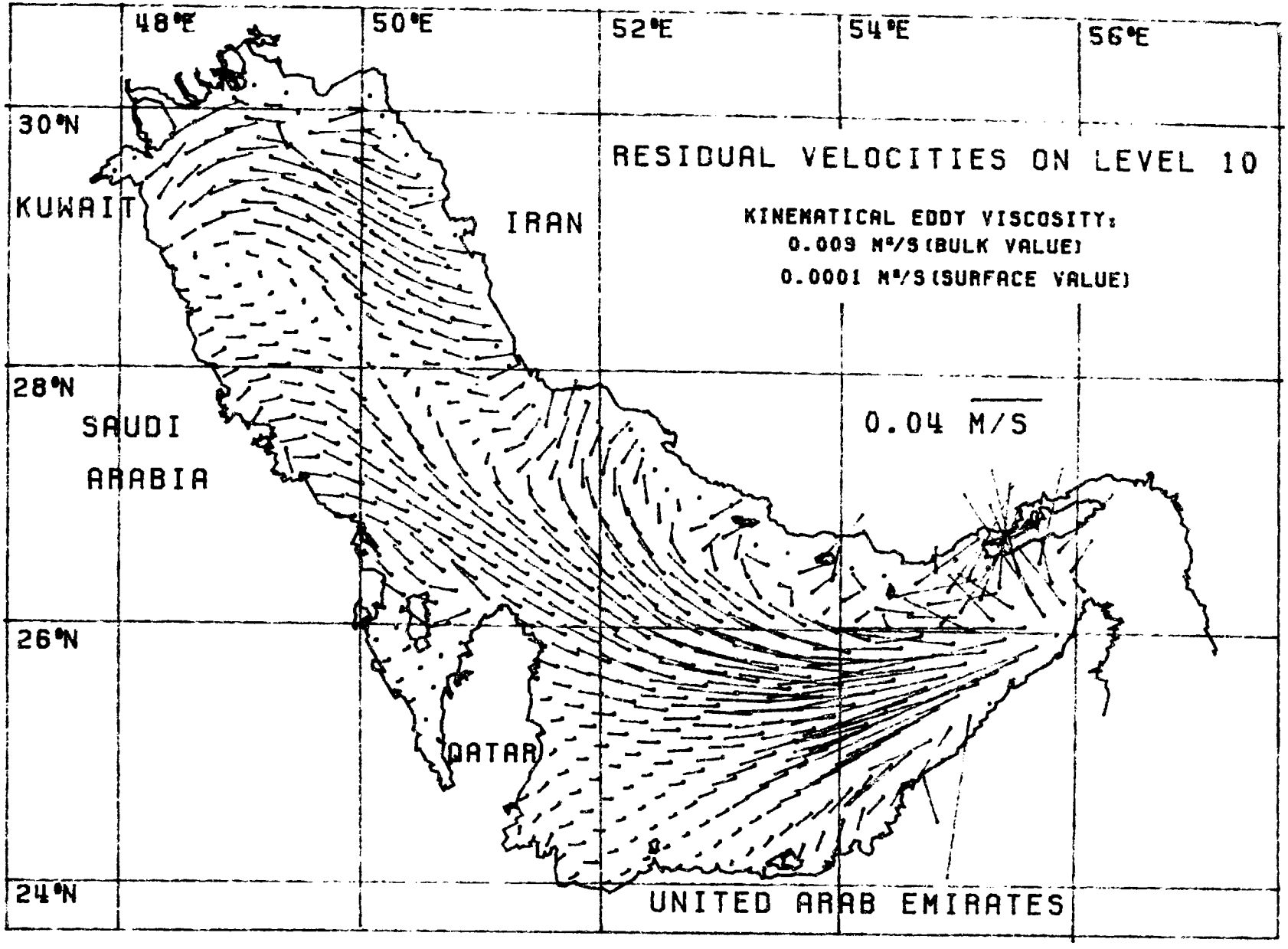
48°E
50°E
52°E
54°E
56°E
30°N
28°N
26°N
24°N
KUWAIT
IRAN
SAUDI
ARABIA
QATAR
UNITED ARAB EMIRATES
RESIDUAL VELOCITIES ON LEVEL 10
KINEMATICAL EDDY VISCOSITY:
0.009 M²/S (BULK VALUE)
0.0001 M²/S (SURFACE VALUE)
0.04 M/S

Figure 5.5(a)

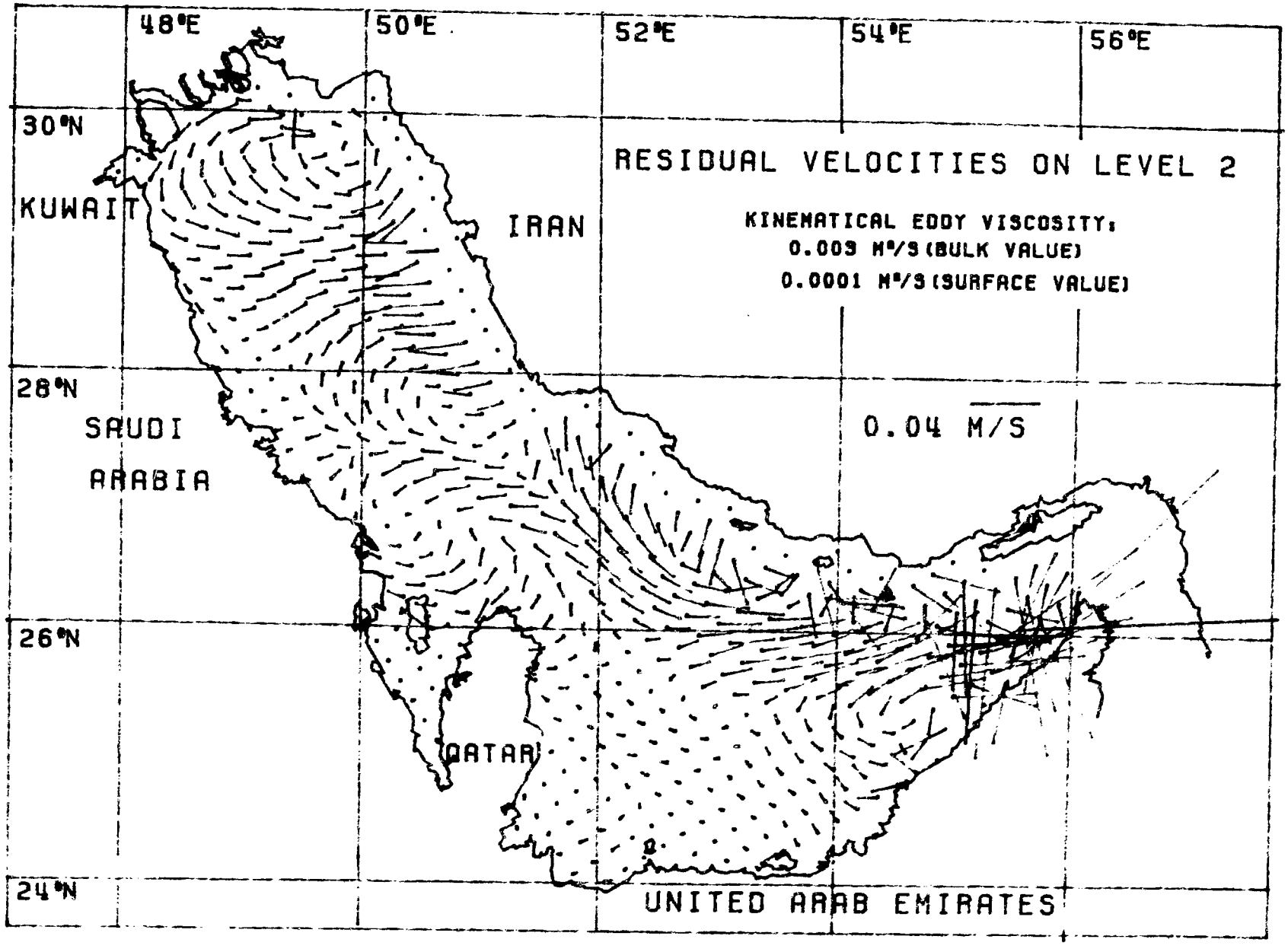
48°E
50°E
52°E
54°E
56°E
30°N
28°N
26°N
24°N
KUWAIT
IRAN
SAUDI
ARABIA
QATAR
UNITED ARAB EMIRATES
RESIDUAL VELOCITIES ON LEVEL 2
KINEMATICAL EDDY VISCOSITY:
0.009 M*/S (BULK VALUE)
0.0001 M*/S (SURFACE VALUE)
0.04 M/S

Figure 5.5(b)

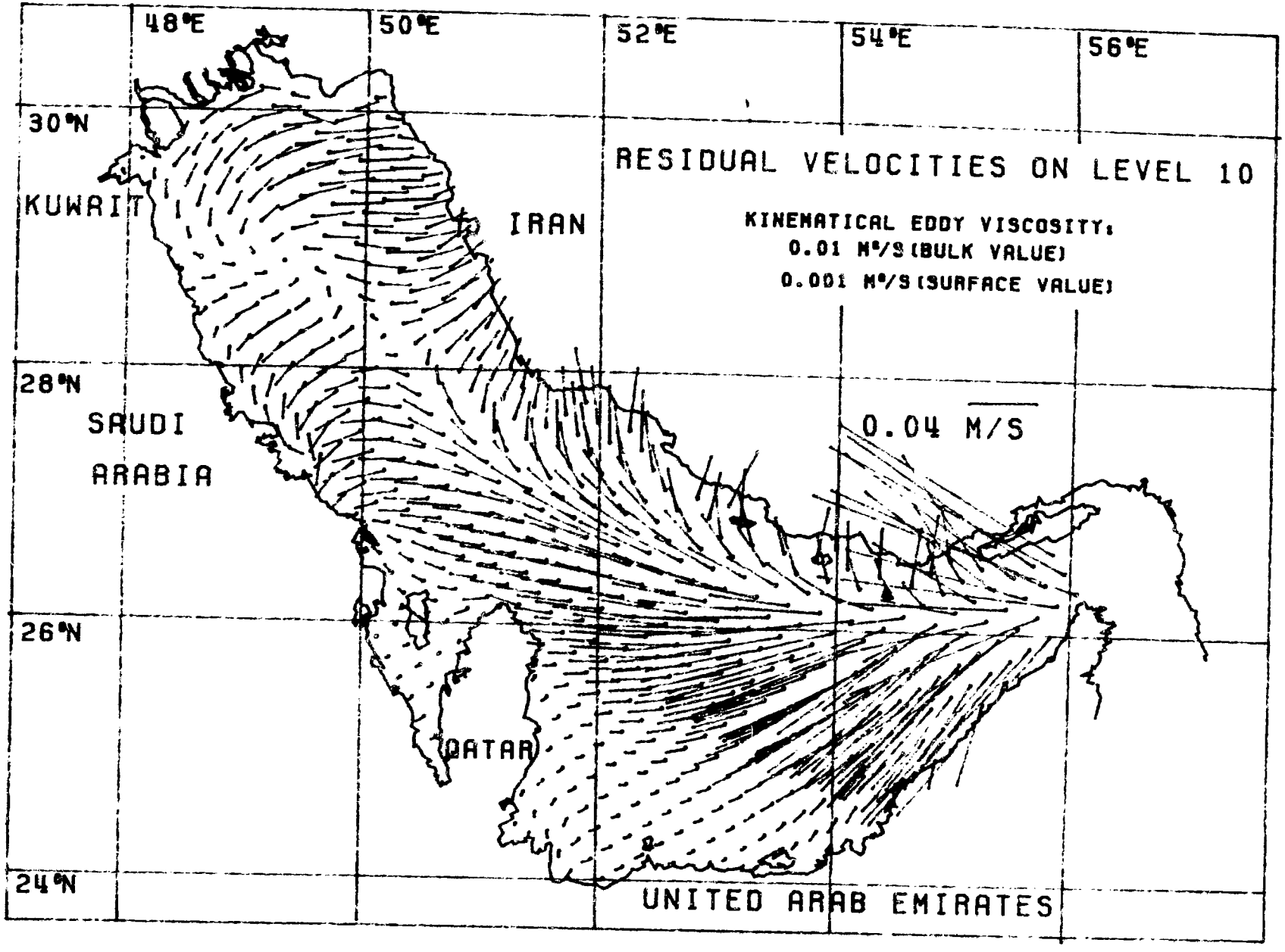
48°E
50°E
52°E
54°E
56°E
30°N
28°N
26°N
24°N
KUWAIT
IRAN
SAUDI
ARABIA
QATAR
UNITED ARAB EMIRATES
RESIDUAL VELOCITIES ON LEVEL 10
KINEMATICAL EDDY VISCOSITY:
0.01 M²/S (BULK VALUE)
0.001 M²/S (SURFACE VALUE)
0.04 M/S

Figure 5.6(a)

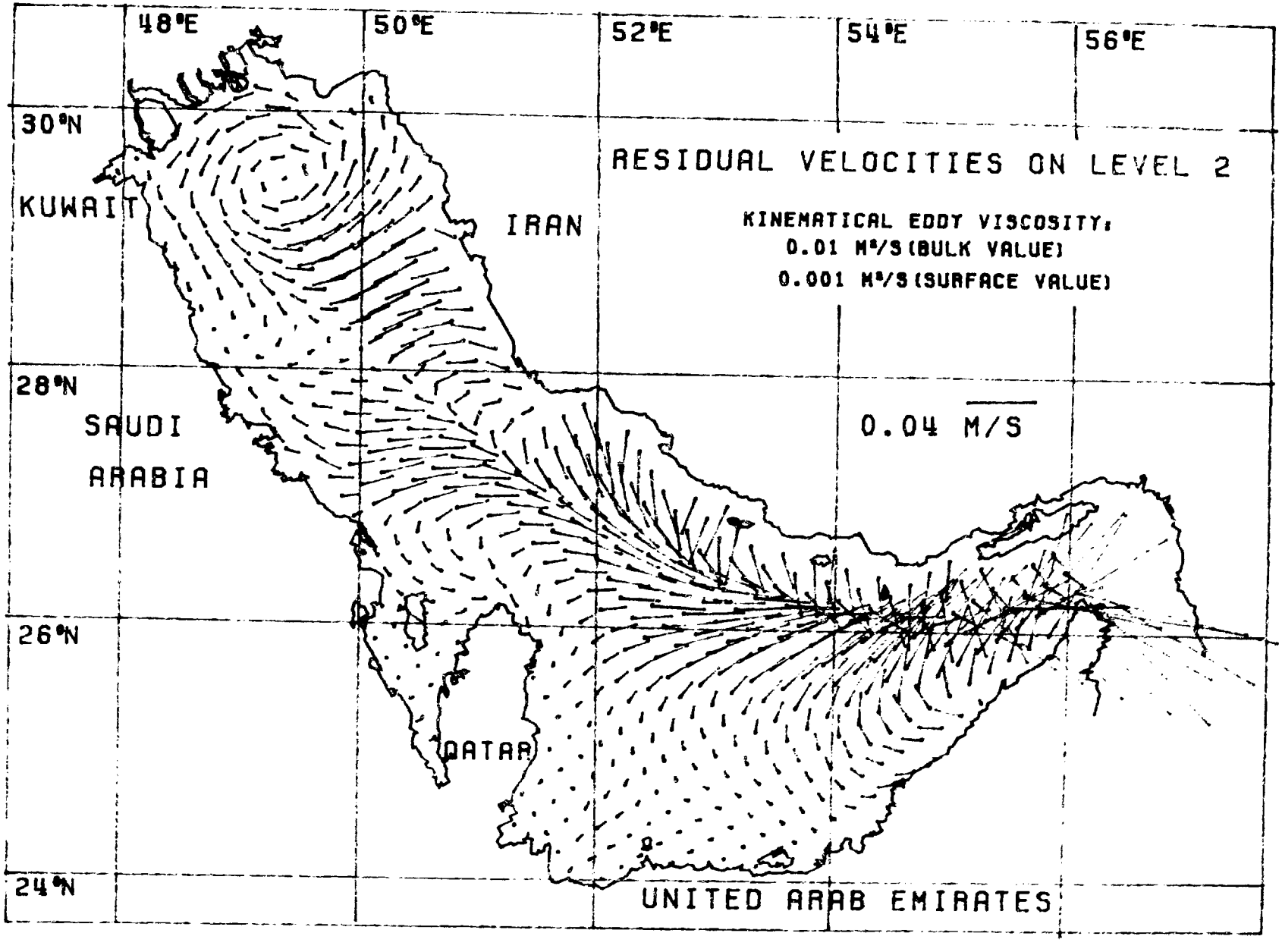
48°E
50°E
52°E
54°E
56°E
30°N
28°N
26°N
24°N
KUWAIT
IRAN
SAUDI
ARABIA
QATAR
UNITED ARAB EMIRATES
RESIDUAL VELOCITIES ON LEVEL 2
KINEMATICAL EDDY VISCOSITY:
0.01 M²/S (BULK VALUE)
0.001 M²/S (SURFACE VALUE)
0.04 M/S

Figure 5.6(b)

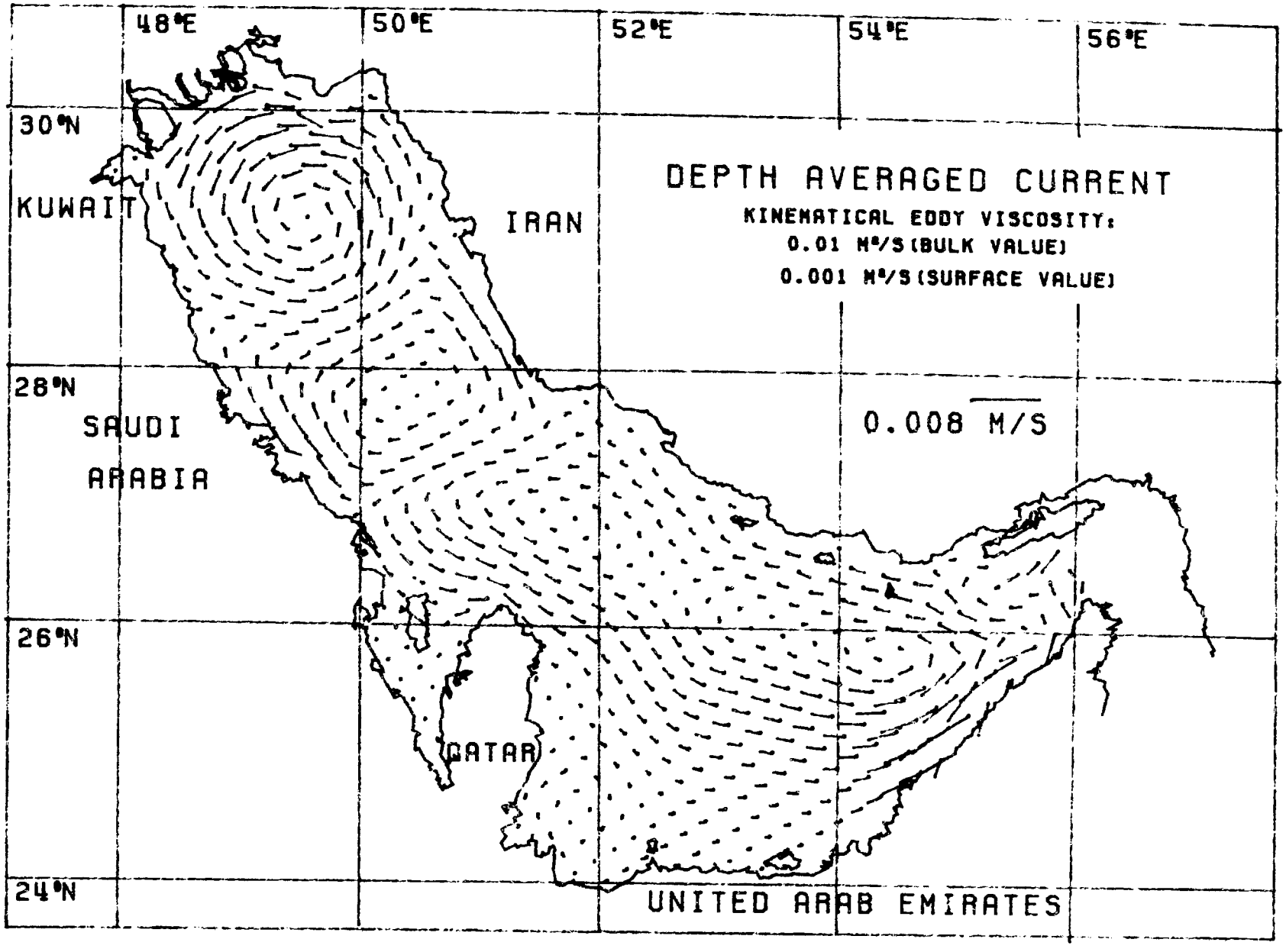
48°E
50°E
52°E
54°E
56°E
30°N
28°N
26°N
24°N
KUWAIT
IRAN
SAUDI
ARABIA
QATAR
UNITED ARAB EMIRATES
DEPTH AVERAGED CURRENT
KINEMATICAL EDDY VISCOSITY:
0.01 M²/S (BULK VALUE)
0.001 M²/S (SURFACE VALUE)
0.008 M/S

Figure 5.6(c)

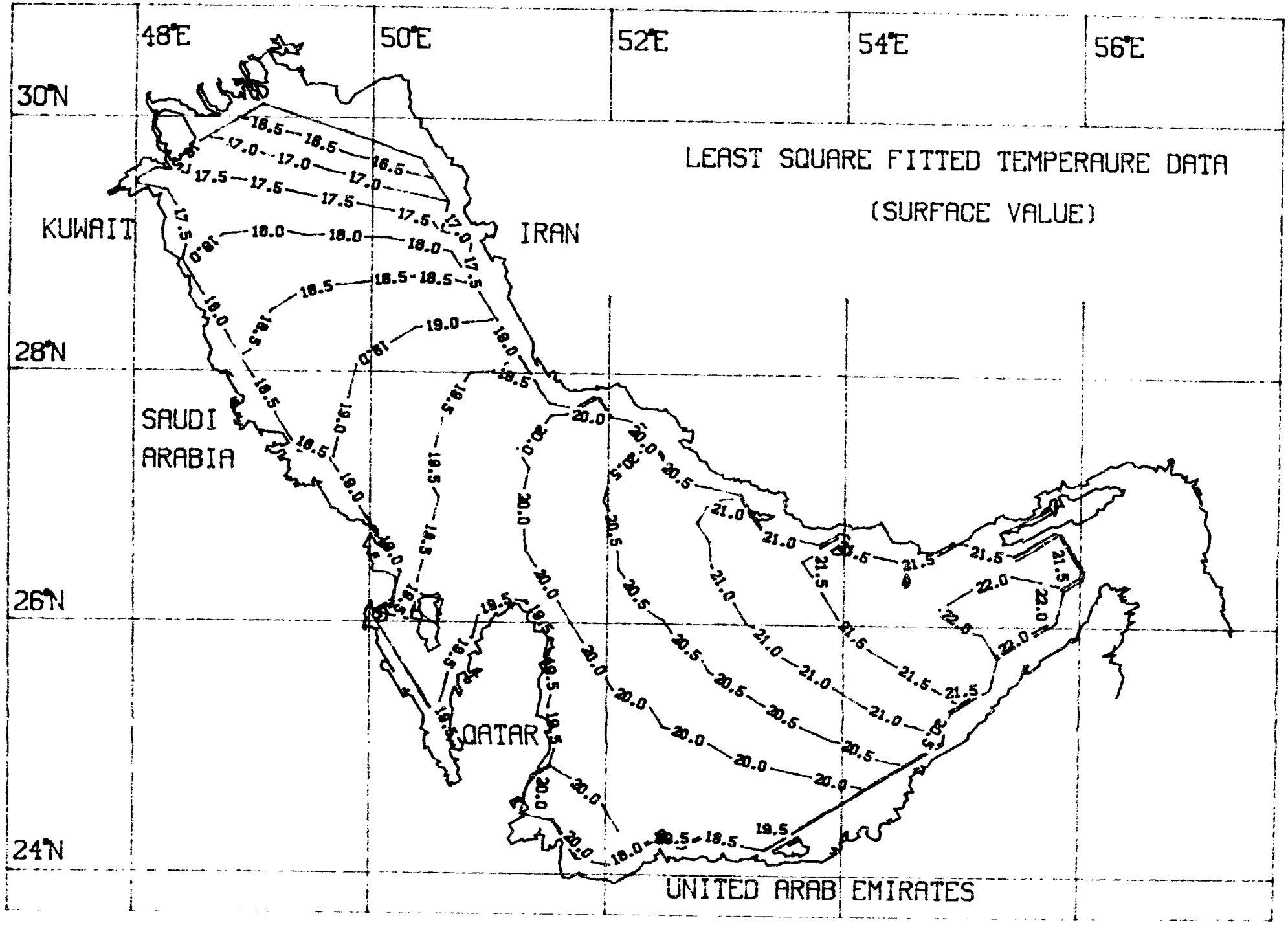
LEAST SQUARE FITTED TEMPERAURE DATA
(SURFACE VALUE)
48°E
50°E
52°E
54°E
56°E
30°N
28°N
26°N
24°N
KUWAIT
IRAN
SAUDI
ARABIA
QATAR
UNITED ARAB EMIRATES

Figure 5.7(a)

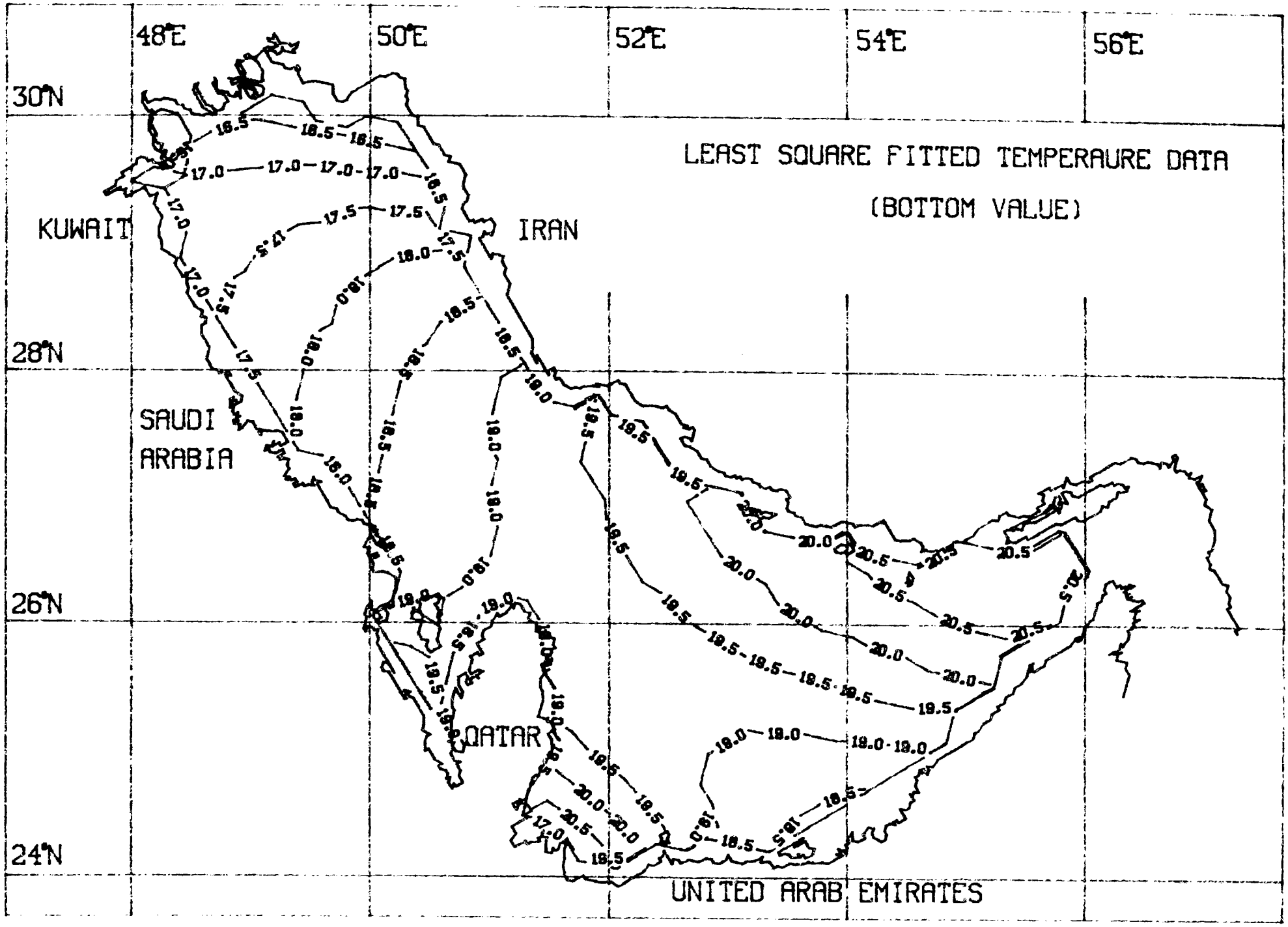
48°E
50°E
52°E
54°E
56°E
30°N
28°N
26°N
24°N
LEAST SQUARE FITTED TEMPERAURE DATA
(BOTTOM VALUE)
KUWAIT
IRAN
SAUDI
ARABIA
QATAR
UNITED ARAB EMIRATES

Figure 5.7(b)

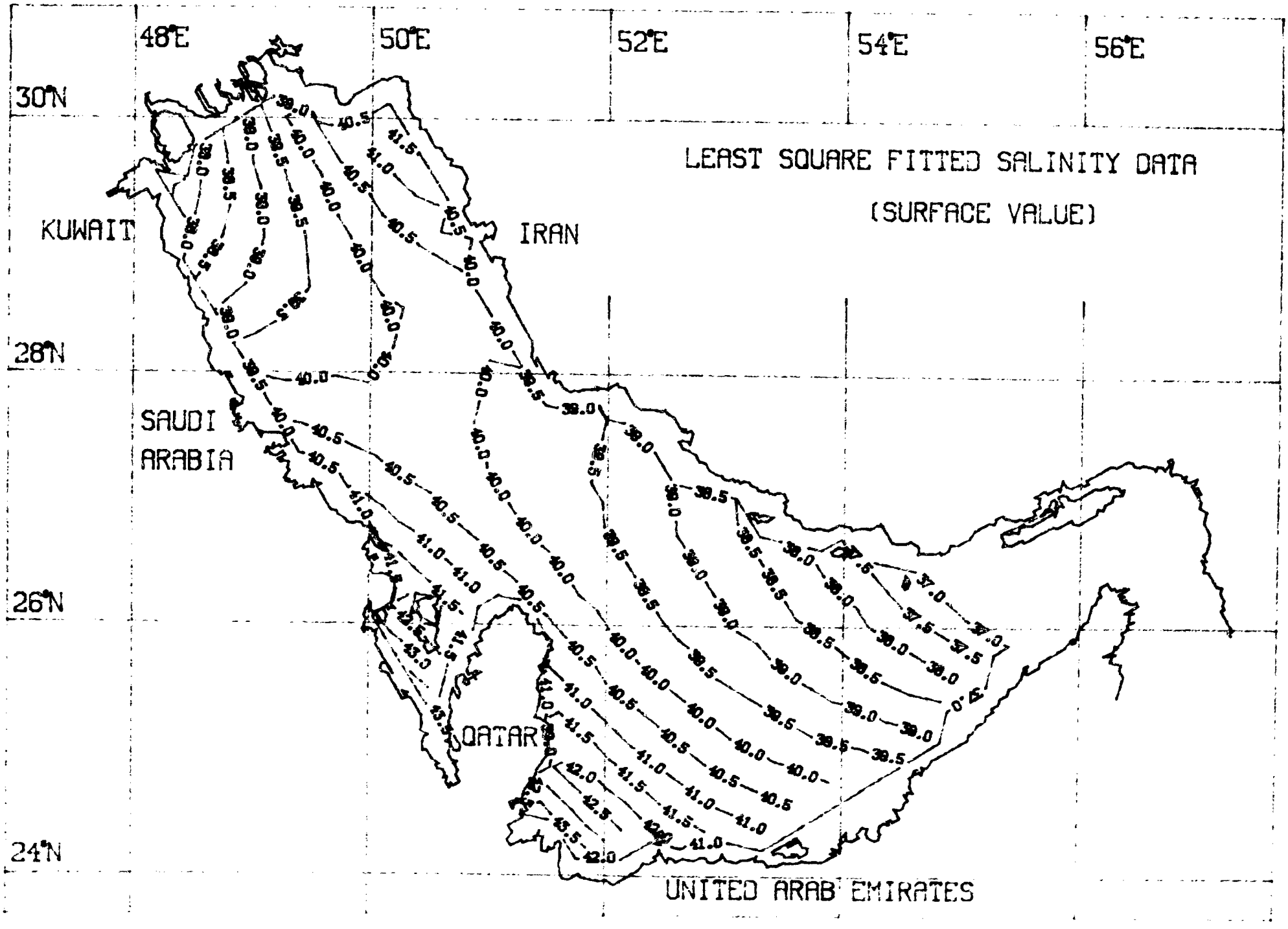
LEAST SQUARE FITTED SALINITY DATA
(SURFACE VALUE)
48°E
50°E
52°E
54°E
56°E
30°N
28°N
26°N
24°N
KUWAIT
IRAN
SAUDI ARABIA
QATAR
UNITED ARAB EMIRATES

Figure 5.8(a)

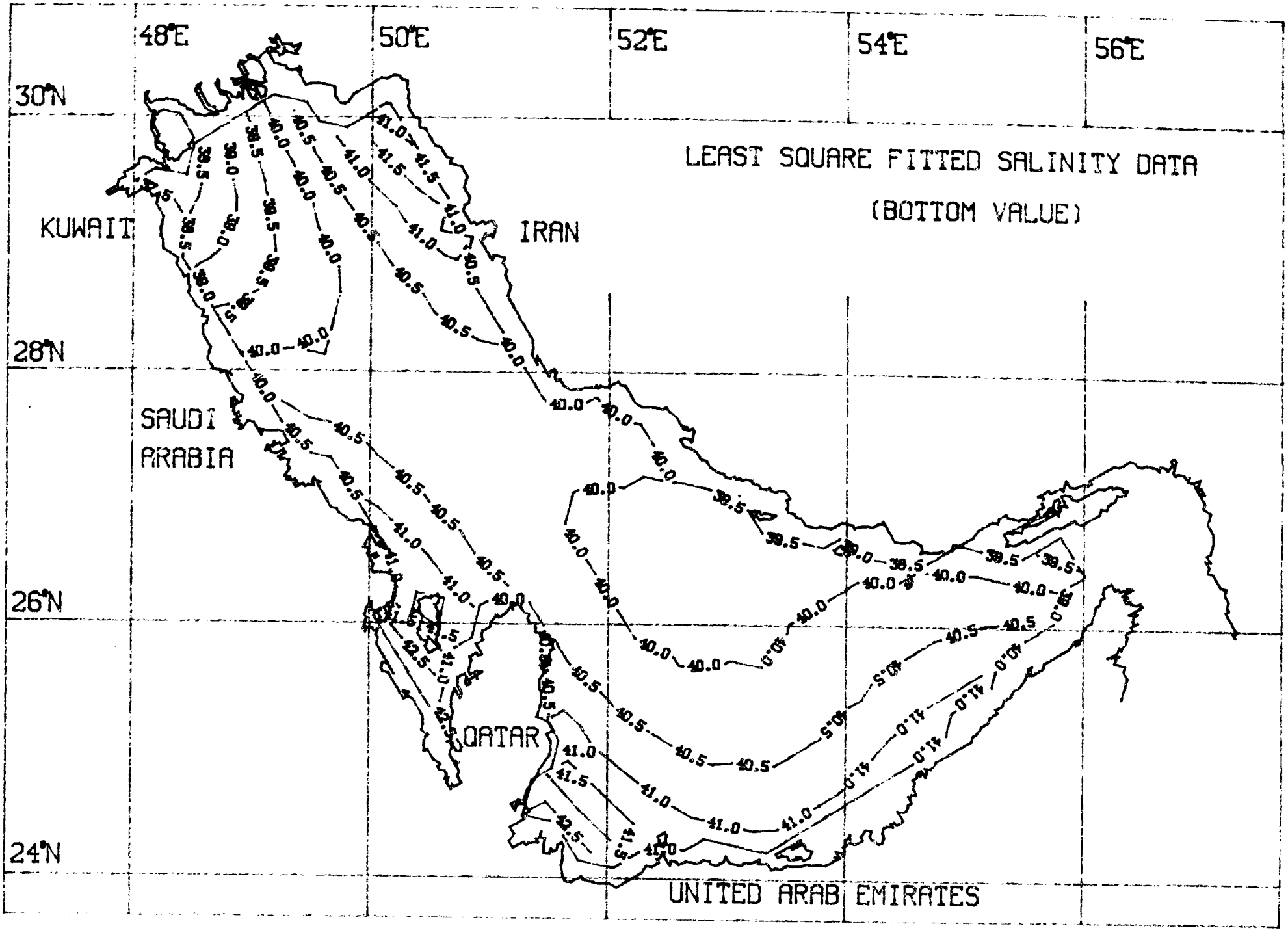
LEAST SQUARE FITTED SALINITY DATA
(BOTTOM VALUE)
48°E
50°E
52°E
54°E
56°E
30°N
28°N
26°N
24°N
KUWAIT
IRAN
SAUDI
ARABIA
QATAR
UNITED ARAB EMIRATES

Figure 5.8(b)

Table 5.1

THE COEFFICIENTS FOR CUBIC FIT TO DENSITY, TEMPERATURE AND SALINITY DATA

	DENSITY	TEMPERATURE	SALINITY
A(1)	0.2650703938462771E+02	0.1667718905517789E+02	0.3620953999376544E+02
A(2)	0.4156932653090434E+00	0.5326787620283518E-01	0.5548308659118876E+00
A(3)	0.2102030559495898E-01	0.3001589953815688E-01	0.3016097907459827E-01
A(4)	-0.6674575712447526E+00	0.1398276519901718E+00	-0.8538821997528205E+00
A(5)	-0.1014503194530303E-01	0.1874769075019286E-02	-0.1227875371961810E-01
A(6)	0.3628374280366405E-01	-0.3971854840894030E-02	0.4674031382902372E-01
A(7)	-0.2142270920490791E+01	0.1474472248871622E+01	-0.2294295598473574E+01
A(8)	-0.4067571889908309E-01	0.7219099042307165E-02	-0.5089966248998657E-01
A(9)	-0.6026352066931123E-02	0.2249974575808201E-01	0.3892760788720810E-02
A(10)	0.1356709886290270E+00	-0.3936769353476895E-01	0.1638165952083810E+00
A(11)	0.7550389339515351E-04	0.5493691252966855E-04	0.1133871551511578E-03
A(12)	-0.4996543671913025E-03	-0.1082901262967899E-02	-0.1038783559128668E-02
A(13)	0.1636381597518812E+01	-0.7043281635381746E+00	0.1903524241417859E+01
A(14)	0.7503153394689535E-03	-0.9538760429519637E-03	0.6531344383353995E-03
A(15)	0.6963068898661909E-03	-0.1756196453469596E-02	0.2791662024435831E-03
A(16)	-0.2962957205632414E-03	0.1791575270114884E-02	0.2327541745506059E-03
A(17)	-0.8784772146363867E-01	0.3625421258610620E-01	-0.1019368183269824E+00
A(18)	-0.6824238606794397E-02	0.1004790120175733E-01	-0.5365343533295787E-02
A(19)	0.1156763086052800E+00	-0.7830559325057540E-01	0.1233005584269260E+00
A(20)	-0.1704055464708122E-02	-0.8187735522069126E-02	-0.5215823201217600E-02

CHAPTER 6 ADJOINT EQUATION FORMULATION FOR DATA ASSIMILATION

In this chapter we will present the mathematical formalism of the variational adjoint formulation of the tidal data assimilation problem. We consider the depth-integrated equations for flow along a one-dimensional channel, the aim being to estimate the parameters in these equations from measurements of surface elevation at certain data stations. First the basic equations are presented on which the work is based. Then the derivation of the adjoint is going to be explicitly stated. This is going to be followed by the finite difference approximations of both the forward and the adjoint problem. Lastly the equations for the parameter approximations are going to be shown.

6.1 Basic equations

We let x be a coordinate along the channel with the channel occupying the interval $0 < x < L$. For definiteness, the end $x = 0$ is taken to be closed and $x = L$ open. The undisturbed depth of the water at the position x is denoted by $h(x)$, the elevation of the free surface above its undisturbed position at time t by $\zeta(x, t)$ and the depth-averaged velocity of the water by $u(x, t)$. The depth-integrated equations of continuity and momentum are then

$$\zeta_t + (hu)_x = 0, \qquad \rho h u_t + g\rho h \zeta_x + \tau = 0$$

where τ is the bottom friction stress and ρ the density, assumed constant. (See eqns. (2.13) and (2.14a) in which $p \to \rho hu$, $q \to 0$, $H = h$ and $\rho = \overline{\rho} = \rho^{(s)}$.) It is assumed that the bottom friction has the form (2.9) which in the present problem becomes

$$\tau = \rho(\kappa_1 + \kappa_2|u|)u$$

where $\kappa_1(x)$ and $\kappa_2(x)$ are linear and quadratic bottom friction coefficients. Usually, only one of κ_1 and κ_2 would be taken as non-zero, depending on whether one is using a linear or quadratic model of bottom friction. By maintaining both terms, we shall be able to deal with both linear and quadratic cases in one go, but in most subsequent applications, only one of them will be retained. The equations can then be expressed as follows:

$$\zeta_t + p_x = 0, \tag{6.1}$$

$$p_t + gh\zeta_x + (k_1 + k_2|p|)p = 0, \tag{6.2}$$

where $p\,(x,\,t) \equiv h\,(x)u\,(x,\,t)$ is the volume flux per unit width of channel and $k_1(x)$ and $k_2(x)$ are defined by $k_1 = \kappa_1/h,\ k_2 = \kappa_2/h^2$.

The boundary conditions are taken to be

$$p(0,t) = 0, \quad \zeta(L,t) = \zeta_0(t), \tag{6.3}$$

where $\zeta_0\,(t)$ is a prescribed periodic function of t determined by the tidal motions in an adjacent large water body to which the channel is connected at its open end. We shall be concerned with the use of tidal measurements to determine the parameter values, so rather than satisfying given initial conditions we suppose that the solution is periodic in time with period T, the period of the tidal component under consideration.

6.2 Derivation of the adjoint problem

It is supposed that prior estimates are available for the three parameters $k_1(x)$, $k_2(x)$ and $h\,(x)$, either from previous measurements or from physical arguments; these are denoted by $k_1'(x), k_2'(x) \text{and} h'(x)$ respectively. It is now assumed that the surface elevation is measured throughout the tidal period at certain stations $x_1, x_2, \ldots$, the measured values being denoted by $\zeta(x_i,t) = Z_i(t)$. These measurements are to be used to determine improved estimates of the three parameters. The basic principle is that the new estimates should minimize the functional

$$\begin{aligned} F = {} & \tfrac{1}{2}L\sum_i \int_0^T K_\zeta\left[\zeta(x_i,t) - Z_i(t)\right]^2 dt \\ & + \tfrac{1}{2}T\int_0^L \left[K_1(k_1 - k_1')^2 + K_2(k_2 - k_2')^2 + K_h(h - h')^2\right]dx \end{aligned} \tag{6.4}$$

The cost function F has been constructed on the premises that it measures the distance(the misfit) between the model and the observations and also, the variational method makes use of the derivative of F, and the cost function must therefore be differentiable. The first term in (6.4) measures the data misfits and will be the forcing for the adjoint equation. The last three terms in (6.4) are added to the cost function because the goal of this research is to estimate the parameters in the model. By adding these terms, the new estimate of the parameters will not be too far from the initial guess. Essentially minimizing the cost function results in a solution which is close to the observations and new values of the parameters which are close to the estimate. Here K_ζ, K_1, K_2 and K_h are the respective weights given to the

measurements and the three prior values. The K's depend on the error variance of each observational point, and give information of the quality of the data.

F is to be minimized subject to the boundary value problem (6.1)-(6.3). Introducing Lagrange multipliers $\lambda(x, t)$ and $\mu(x, t)$, we then obtain

$$\begin{aligned}\delta F = {} & L\sum_i \int_0^T K_\zeta\{\zeta(x_i,t) - Z_i(t)\}\delta\zeta(x_i,t)\,dt \\ & + T\int_0^L \{K_1(k_1 - k_1')\delta k_1 + K_2(k_2 - k_2')\delta k_2 + K_h(h - h')\delta h\}\,dx \\ & + \int_0^T \int_0^L \{\lambda(x,t)\,\delta(\zeta_t + p_x) + \mu(x,t)\,\delta(p_t + gh\zeta_x + (k_1 + k_2|p|)p)\}\,dx\,dt.\end{aligned}$$

The terms in the last integral here that contain t-derivatives are integrated by parts with respect to t. The boundary terms vanish provided we assume that λ and μ are periodic in t with period T. The terms involving x-derivatives are integrated by parts with respect to x. The boundary terms vanish, in view of conditions (6.3), if we require λ and μ to satisfy

$$\mu(0,t) = 0, \quad \lambda(L,t) = 0. \tag{6.5}$$

The remaining terms have the form

$$\begin{aligned}\delta F = {} & L\sum_i \int_0^T K_\zeta\{\zeta(x_i,t) - Z_i(t)\}\delta\zeta(x_i,t)\,dt \\ & - \int_0^T \int_0^L \{\delta\zeta(\lambda_t + (gh\mu)_x) + \delta p(\mu_t + \lambda_x - (k_1 + 2k_2|p|)\mu)\}\,dx\,dt \\ & + T\int_0^L \left\{\delta k_1\left(TK_1(k_1 - k_1') + \int_0^T \mu p\,dt\right) + \delta k_2\left(TK_2(k_2 - k_2') + \int_0^T \mu|p|p\,dt\right)\right. \\ & \left. + \delta h\left(TK_h(h - h') + \int_0^T \mu g\zeta_x\,dt\right)\right\}dx\end{aligned} \tag{6.6}$$

Setting the coefficients of $\delta\zeta$ and δp equal to zero, we obtain the adjoint equations

$$\lambda_t + (gh\mu)_x = \sum_i LK_\zeta\{\zeta(x_i,t) - Z_i(t)\}\delta(x - x_i) \tag{6.7}$$

$$\mu_t + \lambda_x - (k_1 + 2k_2|p|)\mu = 0. \tag{6.8}$$

Here $\delta(x)$ is the Dirac delta function. In view of the sign of the damping term in the second of these equations, the solution must be computed in the negative t-direction, exactly as it would had we started with an initial value problem.

The coefficients of δk_1, δk_2 and δh then provide the three parameter equations

$$\begin{aligned} F_1(x) &\equiv TK_1(k_1 - k_1') + \int_0^T \mu p \, dt = 0 \\ F_2(x) &\equiv TK_2(k_2 - k_2') + \int_0^T \mu |p| p \, dt = 0 \\ F_h(x) &\equiv TK_h(h - h') + \int_0^T \mu g \zeta_x \, dt = 0. \end{aligned} \tag{6.9}$$

In the special case in which the parameters are independent of x, the variations δk_1, δk_2 and δh are constant and the final term in eqn (6.6) then leads to the parameter equations

$$\begin{aligned} F_1 &\equiv LTK_1(k_1 - k_1') + \int_0^L \int_0^T \mu p \, dt \, dx = 0 \\ F_2 &\equiv LTK_2(k_2 - k_2') + \int_0^L \int_0^T \mu |p| p \, dt \, dx = 0 \\ F_h &\equiv LTK_h(h - h') + \int_0^L \int_0^T \mu g \zeta_x \, dt \, dx = 0 \end{aligned} \tag{6.10}$$

in place of (6.9).

If the prior value of a particlar parameter is regarded as sufficiently accurate, the corresponding coefficient K can be taken very large, which in effect means that the corresponding equation can be removed from among eqns (6.9) or (6.10). In particular, the second of eqns (6.9) or (6.10) is dropped for the linear friction case ($k_2 = 0$), while the first of these equations is dropped for quadratic friction ($k_1 = 0$).

6.3 Finite difference approximations

We shall first outline the numerical algorithm used to solve the forward boundary value problem (6.1)-(6.3). Before doing so however, we replace the parameters h, k_1 and k_2 in eqn (6.2) by $S_h h$, $S_1 k_1$ and $S_2 k_2$ where the scale factors S_j are chosen so that the new parameters h, k_1 and k_2 have the same orders of magitude. In practice, we have taken $S_h = 10^2$, $S_1 = 10^4$ and $S_2 = 10^{-5}$. This re-scaling is needed because some minimization algorithms fail unless the variables all have comparable magnitudes.

The numerical algorithm is based on a leapfrog method with staggered spatial and temporal grids. The index m is used for grid-points along the x direction while j indicates the time level. The variables ζ and p are discretized respectively by ζ_m^j which refers to the grid point

(m,j) and p_m^j which refers to the point $(m+\frac{1}{2}, j+\frac{1}{2})$. The open boundary is set at $m = M$.

The finite difference approximation to eqn (1), centred at the grid point $(m, j+\frac{1}{2})$, is then

$$\frac{\zeta_m^{j+1} - \zeta_m^j}{\Delta t} + \frac{p_m^j - p_{m-1}^j}{\Delta x} = 0, \qquad 2 \le m \le M-1 \tag{6.11}$$

where Δx and Δt are the spatial and temporal grid spacings. Eqn (6.11) may be solved explicitly for ζ_m^{j+1}, $m = 2,\ldots,M-1$. ζ_M^{j+1} is determined from the boundary condition (6.3_2) with the appropriate value of $\zeta_0(t)$.

In the discretization of eqn (6.2), the friction term is treated semi-implicitly in order to improve stability. The approximation, centred at the grid point $(m+\frac{1}{2}, j+1)$, is

$$\frac{p_m^{j+1} - p_m^j}{\Delta t} + gS_h h_m \frac{(\zeta_{m+1}^{j+1} - \zeta_m^{j+1})}{\Delta x} + (S_1 k_{1,m} + S_2 k_{2,m} |p_m^j|)\{\alpha p_m^{j+1} + (1-\alpha) p_m^j\} = 0, \qquad 2 \le m \le M-1 \tag{6.12}$$

where α is an implicitness parameter. (In practice we have taken $\alpha = \frac{1}{2}$.) It is here assumed that the depth h is specified as h_m at the same spatial grid points as p_m and that the two friction parameters k_1 and k_2 are also specified at these points. Eqn (6.12) may be solved explicitly for p_m^{j+1}, $m = 2,\ldots,M-1$. The left boundary condition gives $p_1^{j+1} = 0$.

In order to generate a periodic solution, eqns (6.11) and (6.12) are stepped forward starting from zero initial values. After several periods, the initial transients disappear and the solution becomes essentially periodic. The values of ζ and p from the final period are then continued periodically backwards and these continuations used in the discretized versions of the adjoint equations (6.7) and (6.8). In the test problems reported in the next section, we computed the solution over twenty periods to eliminate the transients, but in a practical situation fewer than this would usually suffice. ζ and p must be stored for the last period which corresponds to the last 120 time steps and used in conjunction with the μ and λ stored in the last period to evaluate the gradient of the cost function. The major percentage of memory cost is in storing the ζ, p and the observation Z. Each of them require 2400 bytes of storage space. The remaining memory is shared among the other one-dimensional arrays.

In order to obtain the discrete version of the adjoint problem, the argument of Section 2(b) must be re-developed for the discrete case because the adjoint and discretization operators do not commute. The discrete analogue of the functional F is

$$F = \tfrac{1}{2}\sum_{m=2}^{M-1}\sum_{j=1}^{J} K_\zeta(\zeta_m^j - Z_m^j)^2\,\phi(m)$$
$$+\tfrac{1}{2}J\sum_{m=2}^{M-1}\left\{K_1(k_{1,m}-k'_{1,m})^2 + K_2(k_{2,m}-k'_{2,m})^2 + K_h(h_m - h'_m)^2\right\} \qquad (6.13)$$

where J is the number of time steps per period and $\phi(m) = 1$ if m is a grid point at which the surface elevation is observed and $\phi(m) = 0$ otherwise. F must be minimized subject to the constraints (6.11) and (6.12). To derive the adjoint model equations we form an Augmented Lagrange function by adding to the cost function (6.13) the finite difference model equations:

$$F = \tfrac{1}{2}\sum_{m=2}^{M-1}\sum_{j=1}^{J} K_\zeta(\zeta_m^j - Z_m^j)^2\,\phi(m)$$
$$+\tfrac{1}{2}J\sum_{m=2}^{M-1}\left\{K_1(k_{1,m}-k'_{1,m})^2 + K_2(k_{2,m}-k'_{2,m})^2 + K_h(h_m - h'_m)^2\right\}$$
$$+\sum_{m=2}^{M-1}\sum_{j=1}^{J}\lambda_m^j\left\{\frac{\zeta_m^{j+1}-\zeta_m^j}{\Delta t} + \frac{p_m^j - p_{m-1}^j}{\Delta x}\right\}$$
$$+\sum_{m=2}^{M-1}\sum_{j=1}^{J}\mu_m^{j+1}\left\{\frac{p_m^{j+1}-p_m^j}{\Delta t} + gh_m\frac{(\zeta_{m+1}^{j+1}-\zeta_m^{j+1})}{\Delta x} + (k_{1,m}+k_{2,m}|p_m^j|)\{\alpha p_m^{j+1} + (1-\alpha)p_m^j\}\right\}.$$

where λ_m and μ_m^{j+1} are Lagrange multipliers. In general, the boundary conditions should also appear as constraints with their own Lagrange multipliers; however, for prescribed values at the boundaries, it is simpler to exclude the boundary values from the set of unknowns. Stationarity with respect to the Lagrange multipliers, $\frac{\partial F}{\partial \lambda_m} = 0$ and $\frac{\partial F}{\partial \mu_m^{j+1}} = 0$, gives the original model equations, whereas stationarity with respect to elevation and velocity, $\frac{\partial F}{\partial \zeta_m^j} = 0$ and $\frac{\partial F}{\partial p_m^j} = 0$, gives a set of adjoint equations for the Lagrange multipliers. We then have the following expression for the first variation of F.

$$\delta F = \sum_{m=0} \sum_{j=1}^{J} K_\zeta(\zeta_m^j - Z_m^j)\delta\zeta_m^j$$
$$+J\sum_{m=2}^{M-1}\left[K_1(k_{1,m}-k'_{1,m})\delta k_{1,m} + K_2(k_{2,m}-k'_{2,m})\delta k_{2,m} + K_h(h_m - h'_m)\delta h_m\right]$$
$$+\sum_{m=2}^{M-1}\sum_{j=1}^{J}\lambda_m^j\,\delta\left\{\frac{\zeta_m^{j+1}-\zeta_m^j}{\Delta t} + \frac{p_m^j - p_{m-1}^j}{\Delta x}\right\}$$
$$+\sum_{m=2}^{M-1}\sum_{j=1}^{J}\mu_m^{j+1}\,\delta\left\{\frac{p_m^{j+1}-p_m^j}{\Delta t} + gh_m\frac{(\zeta_{m+1}^{j+1}-\zeta_m^{j+1})}{\Delta x} + (k_{1,m}+k_{2,m}|p_m^j|)\{\alpha p_m^{j+1}+(1-\alpha)p_m^j\}\right\}.$$

The multiplier λ_m^j refers to the grid point $(m, j+\frac{1}{2})$ while μ_m^{j+1} refers to $(m+\frac{1}{2}, j+1)$. After changing certain of the summation indices in an appropriate way and imposing the boundary and periodicity conditions

$$\lambda_M^j = 0, \quad \mu_1^j = 0, \quad \lambda_m^j = \lambda_m^{j+J}, \quad \mu_m^j = \mu_m^{j+J}, \tag{6.14}$$

we can re-write this as

$$\delta F = +\sum_{m=2}^{M-1}\sum_{j=1}^{J}\delta\zeta_m^j\left\{\frac{\lambda_m^{j-1}-\lambda_m^j}{\Delta t} + g\frac{\mu_{m-1}^j h_{m-1} - \mu_m^j h_m}{\Delta x} + K_\zeta(\zeta_m^j - Z_m^j)\delta_{m,0}\right\}$$
$$+\sum_{m=2}^{M-1}\sum_{j=1}^{J}\delta p_m^j\left\{\frac{\mu_m^j - \mu_m^{j+1}}{\Delta t} + \alpha(k_{1,m}+k_{2,m}|p_m^{j-1}|)\mu_m^j + (1-\alpha)(k_{1,m}+k_{2,m}|p_m^j|)\mu_m^{j+1}\right.$$
$$\left.+k_{2,m}\operatorname{sgn} p_m^j\{\alpha p_m^{j+1}+(1-\alpha)p_m^j\}\mu_m^{j+1} + \frac{(\lambda_m^j - \lambda_{m+1}^j)}{\Delta x}\right\}$$
$$+\sum_{m=2}^{M-1}\delta k_{1,m}\left\{JK_1(k_{1,m}-k'_{1,m}) + \sum_{j=1}^{J}\mu_m^{j+1}\{\alpha p_m^{j+1}+(1-\alpha)p_m^j\}\right\}$$
$$+\sum_{m=2}^{M-1}\delta k_{2,m}\left\{JK_2(k_{2,m}-k'_{2,m}) + \sum_{j=1}^{J}\mu_m^{j+1}|p_m^j|\{\alpha p_m^{j+1}+(1-\alpha)p_m^j\}\right\}$$
$$+\sum_{m=2}^{M-1}\delta h_m\left\{JK_h(h_m - h'_m) + \sum_{j=1}^{J} g\mu_m^{j+1}\frac{1}{\Delta x}(\zeta_{m+1}^{j+1} - \zeta_m^{j+1})\right\}. \tag{6.15}$$

Setting the coefficients of the different variations equal to zero, we obtain the following equations holding for $2 \le m \le M-1$.

$$\frac{\lambda_m^{j-1}-\lambda_m^j}{\Delta t} + gS_h\frac{\mu_{m-1}^j h_{m-1} - \mu_m^j h_m}{\Delta x} + K_\zeta(\zeta_m^j - Z_m^j)\phi(m) = 0 \tag{6.16}$$

$$\frac{\mu_m^j - \mu_m^{j+1}}{\Delta t} + \frac{\lambda_m^j - \lambda_{m+1}^j}{\Delta x} + \alpha(S_1 k_{1,m} + S_2 k_{2,m}|p_m^{j-1}|)\mu_m^j$$
$$+ (1-\alpha)(S_1 k_{1,m} + S_2 k_{2,m}|p_m^j|)\mu_m^{j+1} + S_2 k_{2,m} \operatorname{sgn} p_m^j \{\alpha p_m^{j+1} + (1-\alpha)p_m^j\}\mu_m^{j+1} = 0 \qquad (6.17)$$

These quantities satisfy the boundary and periodicity conditions

$$\lambda_M^j = 0, \quad \mu_1^j = 0, \quad \lambda_m^j = \lambda_m^{j+J}, \quad \mu_m^j = \mu_m^{j+J}, \qquad (6.18)$$

The discrete analogues of eqns (6.9) are

$$F_{1,m} \equiv JK_1(k_{1,m} - k'_{1,m}) + S_1 \sum_{j=1}^{J} \mu_m^{j+1}\{\alpha p_m^{j+1} + (1-\alpha)p_m^j\} = 0$$
$$F_{2,m} \equiv JK_2(k_{2,m} - k'_{2,m}) + S_2 \sum_{j=1}^{J} \mu_m^{j+1}|p_m^j|\{\alpha p_m^{j+1} + (1-\alpha)p_m^j\} = 0 \qquad (6.19)$$
$$F_{h,m} \equiv JK_h(h_m - h'_m) + S_h \sum_{j=1}^{J} g\mu_m^{j+1} \frac{1}{\Delta x}(\zeta_{m+1}^{j+1} - \zeta_m^{j+1}) = 0.$$

Equations (6.16) and (6.17) may be stepped backwards in time, first solving (6.17) explicitly for μ_m^j, $m = 2,\ldots,M-1$ then solving (6.14) explicitly for λ_m^{j-1}, $m = 2,\ldots,M-1$. From (6.18) we also have $\mu_1^j = 0$ and $\lambda_M^{j-1} = 0$. As with the forward equations, these adjoint equations are stepped backwards through several periods, starting with zero values, until the solution becomes essentially periodic. The values of λ and μ from the final period are then used, together with the periodic continuation of the corresponding final values of ζ and p from the forward problem to evaluate the sums in eqns (6.19).

We have tested the validity of the gradient of the cost function to be minimized using the formula:

$$\lim_{\alpha \to 0} \frac{F(x + \alpha \vec{\text{grad}} dF) - F(x)}{(\vec{\text{grad}} dF, \alpha \vec{\text{grad}} dF)} = 1$$

as described in Thepaut and Courtier (1991). The test was applied when evaluating single constant parameter k_1, two constant parameters k_2 and h and variable parameters, both k_2 and h, and k_1 and h. Within the limits of rounding error the α was made as small as possible. In every case the gradient was found to be correct.

The expressions in eqns (6.19) are the components of the gradient of F with respect to the parameters $k_{1,m}$ or $k_{2,m}$ and h_m. For the case of constant parameters, these expressions must be replaced by

$$
\begin{aligned}
F_1 &\equiv (M-2)JK_1(k_1-k_1') + S_1\sum_{m=2}^{M-1}\sum_{j=1}^{J}\mu_m^{j+1}\left\{\alpha p_m^{j+1}+(1-\alpha)p_m^j\right\}=0\\
F_2 &\equiv (M-2)JK_2(k_2-k_2') + S_2\sum_{m=2}^{M-1}\sum_{j=1}^{J}\mu_m^{j+1}\left|p_m^j\right|\left\{\alpha p_m^{j+1}+(1-\alpha)p_m^j\right\}=0\\
F_h &= (M-2)JK_h(h-h') + S_h\sum_{m=2}^{M-1}\sum_{j=1}^{J} g\mu_m^{j+1}\frac{1}{\Delta x}(\zeta_{m+1}^{j+1}-\zeta_m^{j+1})=0.
\end{aligned}
\tag{6.20}
$$

6.4 Parameter approximations

In a practical situation, the use of eqns (6.19) to determine the parameter values at each grid point presents a formidable problem due to the large number of grid points in a realistic problem. The effective number of parameters may be reduced by making some approximation, for example by assuming the parameters are piecewise constant or piecewise linear (Chavent et al., 1975). In general, let us suppose the parameters are approximated by some finite element expansions of the form

$$
k_{1,m} \text{ or } k_{2,m} = \sum_{A=1}^{N} M_{mA}p_A, \qquad h_m = \sum_{A=1}^{N} M_{mA}p_{N+A} \tag{6.21}
$$

where $\{p_A : 1 \le A \le 2N\}$ represent some reduced set of parameters and (M_{mA}) is a coefficient matrix. The corresponding expressions for the components of ∇F with respect to the new parameters are given by

$$
\frac{\partial F}{\partial p_A} = \sum_{m=2}^{M-1} M_{mA}F_{1,m} \text{ or } \sum_{m=2}^{M-1} M_{mA}F_{2,m}, \qquad \frac{\partial F}{\partial p_{N+A}} = \sum_{m=2}^{M-1} M_{mA}F_{h,m}, \tag{6.22}
$$

where $F_{1,m}$, $F_{2,m}$ and $F_{h,m}$ are given by eqns (6.20).

In some of the numerical tests to be described below, we have used piecewise linear approximations of this type with $\{p_A\}$ being the nodal values of the actual parameters and (M_{mA}) the appropriate interpolation matrix.

CHAPTER 7 NUMERICAL EXPERIMENTS IN PARAMETER ESTIMATION

The procedure for using the variational method for data assimilation and parameter estimation can be formulated in the following way. A cost function is defined, measuring the distance between model results and observations as in Chapter 6. The cost function is therefore a function of both the observations and the unknown model parameters. Given an initial guess for the model parameters, the numerical model is used to calculate the value of the cost function. An adjoint numerical model is then used to calculate the gradient of the cost function with respect to the many unknown model parameters. Next, an optimization algorithm, as will be described in this Chapter, uses the gradient information to obtain a new guess for the parameters, reducing the value of the cost function. Several such iterations are needed to obtain the minimum value of the cost function, where model results and observations are as close as allowed by the level of measurements noise. The optimal estimate for the parameters is that corresponding to the minimum value of the cost function. We now present a detailed discussion of the several minimization methods employed to carry out the optimization. Subsequently, we will present the results of the numerous numerical experiments carried out to test the efficiency and accuracy of these to get the optimum value of the parameters.

7.1 *Secant method*

Let the parameters be denoted by q_j, j=1,....,P and the gradient components by F_j. To solve a system of P equations, $F_j = 0$, by the secant method requires $P + 1$ starting points at which the values of the quantities F_j have been found. Each of the functions F_j is approximated by a linear function through the appropriate $P + 1$ points, and the P linear equations are then solved for the approximate root.

Suppose that at $P + 1$ points, $q_j = q_j^p$, $p = 0,1,...,P$, the gradient components in eqns (6.19),(6.20) or (6.22) are given by certain known values $F_j = F_j^p$. Then the system

$$\sum_{j=1}^{P}(q_j^p - q_j^0)A_{jE} = F_E^p - F_E^0 \qquad p = 1,...,P$$

is first solved for the coefficients A_{jE} where $E = 1,...,P$, and then the system

$$\sum_{j=1}^{P}(q_j - q_j^0)A_{jE} = -F_E^0 \qquad E = 1,...,P$$

is solved to determine the next approximation q_j to the solution. The last of the $P + 1$ original points is now discarded and the new approximation q_j used as the zeroth point for the next iteration.

Selection of the initial $P + 1$ points can conveniently be reduced to choosing one point in the following way. Let $q_j', j = 1,...,P$ be the initial values of the parameters, leading to the value F' of the functional F and F_j' of one of the corresponding F_j in (6.19). Now F_j is the derivative of F with respect to q_j, so if F is approximated by a quadratic function of q_j and the minimum value is assumed to be close to zero, it follows that the minimum point is given by

$$q_j = q_j' - 2F'/F_j'.$$

This value of the jth parameter is generally found to be closer to the minimum of F than the original q_j'. By modifying each variable in turn in this way, we can generate the required additional P points.

The secant method may be regarded as a quasi-Newton method of minimizing F in which an approximate Hessian matrix is computed at each step using secant approximations to the second derivatives. The above version of this method becomes inefficient when the number of variables is large because of the repeated matrix inversions and an explicit iteration algorithm must be used.

7.2 ***Descent methods***

The expressions on the left of eqns (6.19),(6.20) or (6.22) are the components of ∇F in the space of the parameters. The method of steepest descent involves modifying the parameters in the direction $-\nabla F$, that is,

$$\tilde{q}_j = q_j - sF_j, \qquad j = 1,...,P, \tag{7.1}$$

where the tilde indicates the new parameter values and s is an iteration parameter (or step size) determining the amount of modification.

In the case of a single constant parameter k_2, the iteration formulas (6.21) take the form

$$\tilde{k}_2 = k_2 - s\left\{(M-2)JK_2(k_2 - k_2') + S_2\sum_{m=2}^{M-1}\sum_{j=1}^{J}\mu_m^{j+1}\left|p_m^j\right|\left\{\alpha p_m^{j+1} + (1-\alpha)p_m^j\right\}\right\} \qquad (7.2)$$

In the case of no prior value, this iteration formula is equivalent to the parameter equation of Panchang and O'Brien. In general we shall refer to direct iteration of eqns (7.1) or a subset thereof, with a constant value of s, as the PO method.

Panchang and O'Brien found in their numerical example that direct iteration of (7.2) converged for any initial guess for k_2 and for any choice of s within a very wide range, but to obtain a reasonable rate of convergence an appropriate choice of s must be made. As we shall see later, we have found that in general, the iteration (7.1) does not converge for any s unless the initial guess is sufficiently close to the true value. However, this method generally does converge for a wider range of starting values than does the secant method.

The method of steepest descent itself consists of making repeated line minimizations (or line searches) of F in the direction $-\nabla F$, starting each time from the preceding minimum point. An alternative, which in most cases gives much more rapid convergence, is to use a conjugate gradient method, in which the minimizations are made in a set of conjugate directions rather than steepest descent directions. We have used the Polak-Ribiere form of this method, with and without Beale restarts, with Davidon cubic interpolation for the line searches. A detailed discussion of these algorithms, including the restart criteria, is given by Navon and Legler (1987). We have provided a short description of the Polak-Ribiere conjugate gradient method and Davidon interpolation in an appendix at the end of this chapter.

More sophisticated quasi-Newton methods of minimization are available, in which some information about the Hessian matrix is used. A discussion of some of these is given by Navon and Legler (1987). In obtaining some of the numerical results reported in the next section we have made use of the subroutine CONMIN, written by Shanno and Phua (1980), which contains both a conjugate gradient like memoryless quasi-Newton algorithm with Beale restarts and a quasi-Newton algorithm based on the Broyden-Fletcher-Goldfarb-Shanno (BFGS) scheme of updating the approximate Hessian.

7.3 NUMERICAL TESTS

A number of numerical examples have been used to test the effectiveness of the method described in Chapter 6. In all the examples the values $M = 19$ and $\Delta x = 40{,}000$m have been used, so that $L = 700$ km. The boundary condition (6.3_2) are taken to be sinusoidal,

$$\zeta(L,t) = \cos\omega t, \qquad \omega = 2\pi/T, \tag{7.3}$$

where $T = 12$ hrs. The time step used was $\Delta t = 360$s, or 120 steps per period.

It is assumed that the values of ζ at the two points x_1 and x_2 corresponding to the grid points $m = 8$ and 16 are known from measurements, and occur in the first term of eqn (6.4). The function F can be normalized arbitrarily, and we have taken $K_\zeta \Delta t = 1$, which somewhat simplifies eqn (6.16).

The convergence criterion used for most of the iterations was that successive values of each parameter should differ by less than 0.01%. For the algorithms in the CONMIN subroutine, the convergence criterion is based on the magnitude of the gradient of F.

Unless explicitly stated, all quantities given below are in MKS units.

7.3.1 Constant coefficients, linear friction

In this case, $k_2 = 0$ and k_1 and h are constant. The parameters are determine from eqns (6.20_1) and (6.20_3). The exact solution with boundary condition (7.3) is given by

$$Z_i(t) = \Re\left\{\frac{\zeta_0 \cos\alpha x_i}{\cos\alpha L} e^{i\omega t}\right\}, \qquad \alpha = \sqrt{\frac{\omega^2 - ik\omega}{gh}},$$

and this is used as the "empirical" values at the two points x_1 and x_2.

We consider the following three cases: (i) h is known (= 65m) and k_1 is determined from eqn (6.20_1), the true value being 0.3×10^{-4}; (ii) k_1 is known ($= 0.3\times10^{-4}$) and h is determined from eqn (6.20_3), the true value being 65; (iii) both k_1 and h are to be determined, with their true values being 0.3×10^{-4} and 65 respectively. These cases involve just one or two variables and offer a good opportunity to compare the PO (direct iteration) method, the secant method and the Davidon cubic interpolation method (plus conjugate gradients in case (iii)). The results obtained are as follows.

Case (i)

When $K_1 = 0$ (no prior information) the secant method converges when the starting value is in the interval $0 \leq k_1 \leq 0.73\times10^{-4}$, but diverges outside that interval. The convergence typically requires 5 - 6 iterations for 0.01% error. As K_1 is increased the interval of convergence also increases and the number of iterations decreases. Table 7.1 shows how the final value of k_1 and number of iterations changes as the weight K_1 is increased. The prior estimate k_1' was 0.15×10^{-4} and it can be seen that the final value of k_1 approaches this estimate as K_1 is increased. This result is not surprising, and shows that the variational algorithm is working as expected. In Figure 7.1 we plot the function value against k_1 as K_1 is increased.

$(M-2)JK_1$	Final value of k_1	Number of iterations
10^{-3}	0.2972×10^{-4}	5
10^{-2}	0.2948×10^{-4}	4
10^{-1}	0.2751×10^{-4}	4
10^{0}	0.2084×10^{-4}	4
10^{1}	0.1598×10^{-4}	3
10^{2}	0.1511×10^{-4}	3

Table 7.1. Final value of k_1 and number of iterations for different values of the prior weighting factor K_1. The starting value was $k_1 = 0.5\times10^{-4}$ in each case.

When K_1 is zero the PO method converges if the starting value is in the somewhat larger interval $0 \leq k_1 \leq 0.9\times10^{-4}$, provided a suitable iteration parameter s is used in eqn (7.1), and again there is convergence for a larger interval when $K_1 > 0$. The number of iterations can be diminished and the interval of convergence considerably enlarged by adjusting the iteration parameter s in (6.22_1) from one iteration to the next. However, unlike the case investigated by Panchang and O'Brien (1989), convergence cannot be achieved for all starting values by using only positive values of s.

When $K_1 = 0$ the Davidon cubic interpolation algorithm converges if the initial value is in the interval $0 \leq k_1 \leq 0.78\times10^{-4}$, and typically requires 5 - 7 iterations.

The first two rows of Table 7.2 give some comparison of the rates of convergence of the three methods when $K_1 = 0$. Each method was run for two starting values: $k_1 =$

0.5×10^{-4}, and 0.1×10^{-4} with the same termination criterion. The table gives for each method the final value of k_1 and the number of iterations (that is, the number of evaluations of the gradient of F required to meet this convergence condition). It can be seen that all the methods converge to the same parameter value.

In the case of the PO method it is always possible to find a value of s in (7.1) so that this method converges in a single iteration, that is with two such evaluations, so this number is rather meaningless in this case. However, considerable experimentation is required to find this value of s. Furthermore, this magic value sometimes lies outside the interval $0 < s < s_0$ in which the iterations converge (for example when $k_1 = 0.5\times10^{-4}$) and in such a case, the smallest number of iterations that is obtainable within the interval of convergence is given.

For the secant method the second value of the parameter is chosen as $k_1 - 2F/F_1$ where F and F_1 are computed using the starting value k_1. We have plotted the values of $\frac{|\nabla F|}{|\nabla F_0|}$ against the number of iterations in Figure 7.1(a) for this case.

		PO method		Secant method		Davidon method	
Case	Start value	Final value	N	Final value	N	Final value	N
(i)	$k_1 = 0.5\times10^{-4}$	0.2975×10^{-4}	5	0.2975×10^{-4}	6	0.2975×10^{-4}	5
(i)	$k_1 = 0.1\times10^{-4}$	0.2975×10^{-4}	2	0.2975×10^{-4}	5	0.2975×10^{-4}	7
(ii)	$h = 55$	65.26	2	65.27	6	65.28	7
(ii)	$h = 75$	65.28	5	65.27	8	65.28	6

Table 7.2. Estimates in the single parameter cases for linear friction. The starting values of the different parameters are given in column 2 and the final values obtained with the three different minimization algorithms are in subsequent columns.

Case (ii)

When K_h is zero the secant method converges when the starting value is in the interval $47 \leq h \leq 78$, but diverges outside that interval. The PO method converges if the starting value is in the interval $43.5 \leq h \leq 446$, provided a suitable iteration parameter s is used. The Davidon cubic interpolation algorithm converges if the initial value is in the interval $43.9 \leq h \leq 125$.

The last two rows of Table 7.2 again give some comparison of the final values of h and the numbers of iterations for the three methods with each method being run for two starting values: $h = 55$ and 75. In each case $K_h = 0$. As before, the value of s for the PO method is chosen to give the optimum rate of convergence and the second value of the parameter for the secant method is chosen as $h - 2F/F_h$ where F and F_h are computed using the starting value h.

Table 7.3 shows how the final value of h and number of iterations for the secant method changes as the weight K_h is increased. The prior estimate h' was 25 and it can be seen that the final value of h approaches this estimate as K_1 is increased. The number of iterations first increases as K_1 is increased, which suggests the existence of two adjacent local minima of F.

In order to investigate this more closely, we have graphed F as a function of h for several values of K_h in Figure 7.2. When $K_h = 0$, F has two local minima, at h approximately equal to 25 and 65, the second minimum value being several orders of magnitude smaller than the first. By coincidence, we had chosen $h = 25$ as the prior estimate in Table 7.3, so the relative importance of the first minimum is enhanced as K_h is increased. For $(M - 2)JK_h = 1$, the two minimum values are almost equal, leading to a large number of iterations before final convergence. (Use of second order Hessian information can reveal more information concerning the existence of multiple local minima.)

$(M - 2)JK_H$	Final value of h	Number of iterations
10^{-2}	65.12	6
10^{-1}	64.01	4
10^{0}	59.25	13
10^{1}	24.45	6
10^{2}	24.84	4
10^{3}	24.98	3

Table 7.3. Final value of h and number of iterations for different values of the prior weighting factor K_h. The starting value was $h = 55$ in each case.

Case (iii)

When both h and k_1 are unknown, eqns (6.20_1) and (6.20_3) must be solved together.

Table 7.4 gives the final values of the two parameters and the number of iterations using the PO direct iteration method, the secant method and the Polak-Ribiere conjugate gradient method with Davidon cubic interpolation. The tabulated values refer to the case when K_1 and K_A are both zero and results for two different pairs of starting values are given. In the case of the PO method, a very considerable amount of experimentation is needed to find the optimal value of s and the number of iterations sometimes increases very significantly if s differs only a little from this value. The number of function evaluations in the conjugate gradient method is significantly reduced if Beale restarts are included, and the algorithm then becomes comparable in efficiency with the secant method (see also sub-section (b) below).

The value of the objective function is very significantly reduced by the minimization, from initial values of 0.1 and 0.4×10^{-2} in the two cases to about 0.1×10^{-11}.

	PO method		Secant method		Conjugate gradient	
Start values	Final values	N	Final values	N	Final values	N
$k_1 = 0.1\times10^{-4}$	0.2981×10^{-4}	55	0.2987×10^{-4}	12	0.2987×10^{-4}	26
$h = 55$	65.26		65.26		65.26	
$k_1 = 0.43\times10^{-4}$	0.2987×10^{-4}	20	0.2987×10^{-4}	10	0.2987×10^{-4}	21
$h = 71$	65.26		65.26		65.26	

Table 7.4. Estimates in the two-parameter case. The starting values of k_1 and h are given in column 1 and the final values obtained with the three different minimization algorithms are in subsequent columns.

7.3.2 Constant coefficients, quadratic friction

We now consider the general case when $k_1 = 0$ and k_2 and h are constants, so that the parameters are determined from eqns (6.20_2) and (6.20_3). In this case, the exact solution cannot be found analytically, so it has been determined numerically by the same algorithm as described in Chapter 6 but with very fine spatial and temporal grids. In practice a grid size of Δx = 1600m and time step Δt = 15s were used,

smaller by factors of 25 and 15 than the corresponding values used for the parameter estimations. This "exact" numerical solution is then used in place of the experimental measurements Z_i in eqn (6.13).

Case (i)

Here, $k_1 = 0, h = 65$ is assumed known and k_2 is to be determined from eqn (6.20_2), the true value being 0.25×10^{-5}. The results found are similar to those for linear friction. In this case, the starting intervals in which the three algorithms converge are all about the same, namely $0 \le k_2 \le 0.7\times10^{-5}$.

Some typical results obtained with the three methods for two starting values of k_2 are given in Table 7.5. In both cases the prior weighting $K_2 = 0$. Again, for the PO method the value of s in (7.2) is adjusted to give the minimum number of iterations within the interval of convergence. For the secant method the second value of the parameter is chosen as $k_2 - 2F/F_2$ where F and F_2 are computed using the starting value k_2. As in the linear case, all three algorithms yield essentially the same final value of the parameter.

	PO method		Secant method		Davidon method	
Start value	Final value	N	Final value	N	Final value	N
$k_2 = 0.5\times10^{-7}$	0.2472×10^{-5}	2	0.2472×10^{-5}	8	0.2474×10^{-5}	12
$k_2 = 0.5\times10^{-5}$	0.2472×10^{-5}	7	0.2472×10^{-5}	7	0.2472×10^{-5}	11
$h = 55$	65.04	2	65.04	6	65.05	16

Table 7.5. Estimates in the single parameter cases for quadratic friction. The starting value of k_2 or h is given in column 2 and the final values obtained with the three different minimization algorithms are in subsequent columns.

If the prior weighting K_2 is non-zero, results similar to those shown in Table 7.1 are obtained. The final value of k_2 approaches the prior estimate as K_2 is increased. Again we plot the function value against k_2 as K_2 is increased in Figure 7.3. We have also

plotted the logarithm of the values of $\frac{|\nabla F|}{|\nabla F_0|}$ against the number of iterations for the secant case in Figure 7.3(a).

Case (ii)

Here, $k_1 = 0$, $k_2 = 0.25\times10^{-5}$ and h is to be determined, the true value being 65. The intervals of starting values in which the three algorithms converge were found to be convergent were $40 \leq h \leq 1100$ for the PO method, $43.5 \leq h \leq 80$ for the secant method and $40 \leq h \leq 125$ for the Davidon method. One typical set of results with the starting value 55 is given in the last row of Table 7.5.

Again for non-zero values of the prior weighting factor K_A results similar to those shown in Table 7.3 are obtained.

Case (iii)

Here it is assumed that $k_1 = 0$, and k_2 and h are both to be determined from eqns (6.20_2) and (6.20_3), the true values being 0.25×10^{-5} and 65 respectively. Table 7.6 gives the final values of the two parameters and the number of iterations using the PO direct iteration method, the secant method and the Polak-Ribiere conjugate gradient method with Davidon cubic interpolation. The tabulated values refer to the case when K_2 and K_A are both zero and results for two different pairs of starting values are given. In the first case, the value of F is reduced by the minimization from 0.28×10^{-2} to 0.64×10^{-5} and in the second from 0.14×10^{-1} to 0.73×10^{-5}. These optimal values of F are greater than those in the linear case, presumably because of additional discretization errors in the treatment of the nonlinear damping.

As in the case of linear friction, the efficiency of the conjugate gradient method is improved to a level comparable to that of the secant method if Beale restarts are included. We have also tested the BFGS quasi-Newton algorithm on this problem and have found that the values of the parameters converge to 0.2475×10^{-5} and 64.98 in the first case and 0.2478×10^{-5} and 65.00 in the second, with 9 and 8 function calls respectively.

	PO method		Secant method		Conjugate gradient	
Start values	Final values	N	Final values	N	Final values	N
$k_2 = 0.35\times10^{-5}$	0.2471×10^{-5}	8	0.2470×10^{-5}	11	0.2470×10^{-5}	32
$h = 75$	64.95		64.95		64.95	
$k_2 = 0.15\times10^{-5}$	0.2470×10^{-5}	13	0.2470×10^{-5}	9	0.2471×10^{-5}	21
$h = 55$	64.95		64.95		64.95	

Table 7.6. Estimates in the two-parameter case for quadratic friction. The starting values of k_2 and h are given in column 1 and the final values obtained with the three different minimization algorithms are in subsequent columns.

Case (iv)

We have also examined the case when all three variables k_1, k_2 and h are unknown and must be determined from all three of eqns (6.20), the true values being 0.3×10^{-4}, 0.25×10^{-5} and 65 repectively. In this case, all the methods converge provided the starting values are sufficiently close to the true values, the number of iterations being generally in the range 10-20. The final value of h is in every case as close to the true value as in the results reported above. However, the values of k_1 and k_2 are not obtained accurately. Almost invariably, one of these parameters is estimated as too large, the other too small, the final estimated values depending on the starting values and the errors being typically 10-20%. Commonly, but not invariably, all the minimization algorithms yield the same erroneous estimates.

It seems clear from this experience that k_1 and k_2 are to some extent interchangeable parameters, with the solutions at the two measurement points being relatively insensitive to an increase in one of these parameters and appropriate decrease of the other. The problem of distinguishing between them on the basis of the assumed data is apparently not well-posed.

7.3.3 Variable coefficients

We have examined some problems in which k_1 or k_2 and h are functions of position along the channel. Again the "empirical" values are constructed numerically using the very fine grid. As before we considered both linear friction in which $k_2 = 0$ and k_1 and h are estimated from eqns (6.19_1) and (6.19_3) and quadratic friction in which $k_1 = 0$ and k_2 and h are estimated from

eqns (6.19_2) and (6.19_3). With the grid used, the number of grid points at which parameter values are to be determined is 17, giving in each case a parameter space of dimension 34 if eqns (6.19) are used. This dimension is reduced if finite element approximations of the type given in eqns (6.21) and (6.22) are used.

In the two-parameter cases, we found the PO direct iteration method quite difficult to use insofar as elaborate experimentation was needed to discover a suitable iteration parameter, so we have not attempted to use this approach in these cases involving more parameters. Consequently, in these variable parameter cases, we have examined only the conjugate gradient and BFGS algorithms and the secant method. In all of the cases tested, these algorithms yielded essentially the same values of the parameters when they all converged. The BFGS algorithm generally converged for a wider range of starting values than the conjugate gradient like memoryless quasi-Newton algorithm with Beale restarts (CGB) while the secant method was the least robust in this regard. Since most of the computing cost lies in the evaluation of the function and gradient values, the matrix inversions of the secant method did not add significantly to the cost even with the full 34 parameters.

First, we considered the same problem as in subsection (b) in which $k_2 = 0.25\times10^{-5}$ and h = 65 are constant, but with these two parameters determined pointwise from eqns (6.21) and (6.22). Figure 7.4(a) and (b) shows the estimated values of k_2 and h obtained using piecewise linear approximations with 2, 3, 4 and 5 nodes. The value of F is reduced by the minimization from 0.14×10^{-1} to about 0.6×10^{-5} in each case, and takes between 15 and 22 iterations.

Figure 7.5(a) and (b) shows similar estimations of k_2 and h in a case where the true values of these parameters increase linearly from the closed to the open end of the channel. In this case the value of F is reduced from 0.2×10^{-1} to 0.2×10^{-4}. We have plotted the logarithm of the values of $\frac{|\nabla F|}{|\nabla F_0|}$ against the number of iterations in Figure 7.5(c) for this case.

It is clear from these two figures that the estimates obtained with 2 nodes are as accurate as those described earlier for the constant parameter cases, but those with more nodes are very inaccurate. The parameter values obtained using eqns (6.19) and the full 34 dimensions of the parameter space are even less accurate than those shown for four nodes. Note that the parameter estimates are not even accurate in the vicinity of the two data stations, m = 8 and 16. The data at these stations is reproduced as accurately with these unsatisfactory parameter

profiles as it is with the exact profiles, the residual errors coming predominantly from the truncation errors in the approximations (6.11) and (6.12).

It thus appears that the inverse problem is not well posed if the number of independent parameter values to be determined exceeds four. This however is not surprising since the assumed empirical data, the surface elevations at two stations, contains essentially four scalar values, namely the amplitudes and phases of the fundamental at the two stations. While for quadratic friction, the nonlinearity does generate higher harmonics, the amplitudes of these are apparently too weak to provide significant additional information. This would suggest that the number of independent parameters that can be estimated cannot exceed twice the number of data stations. (It is also worth noting that in the case of many parameter values ill-posedness can be eliminated by using a penalty-regularization approach.)

In order to test this hypothesis we have examined the effect of including additional data stations. We first considered the same example of constant linear friction that was used in subsection 7.3.1 in which $k_1 = 0.3\times10^{-4}$ and $h = 65$. The number of nodes was allowed to be 2,3,4 or 5. In each case we found that when the number of tide stations is equal to the number of nodes the final estimates converged to the values $k_1 = 0.29868\times10^{-4}$ and $h = 65.261$ regardless of the starting values (provided these latter were sufficiently close to the true values for the minimization algorithm to converge). (To achieve this five figure accuracy we used a more stringent convergence criterion than previously.) On the other hand, if the number of tide stations is smaller than the number of nodes then the predicted values of the parameters depend sensitively on the starting values and moreover show similar irregularities to those illustrated in Figure 7.4 for 3 or more nodes. This result is consistent with the above conjecture. Figure 7.6 gives the variation of the logarithm of the values of $\frac{|\nabla F|}{|\nabla F_0|}$ with the number of iterations.

Figure 7.7(a) and (b) shows some results obtained for quadratic friction when the true values of depth and friction coefficient vary as quadratic functions of distance along the channel. The figure shows the approximations to these functions obtained using 2,3,4 and 5 nodes, in each case with the number of data stations equal to the number of nodes. The estimated parameters are reasonable approximations to the true values within the respective function class in each case; as anticipated, the approximation improves as the number of nodes is increased. As with the previous example, if a smaller number of data stations is used, the estimates become less reasonable and depend on the assumed starting values.

In a subsequent series of experiments we experimented with large-scale minimization algorithms such as L-BFGS(Nocedal, 1980) and the truncated-Newton method(Nash, 1985; Schlick and Fogelson, 1990). The performance of all the above algorithms for all the three cases of constant, linearly varying and quadratically varying parameters. In the first case the function value goes down to 3.1×10^{-10}, in the second to $2.\times10^{-9}$ and in the third to 7.75×10^{-8}. It is worth noting that the final function values turn out to be very small as compared to that achieved by the CONMIN subroutine.

7.4 SUMMARY AND DISCUSSION

In Chapters 6 and 7 we have examined the feasibility of estimating the parameters of a hydraulic model by assimilating periodic tidal data. A variational approach has been used in which the dynamical equations are imposed as strong constraints (Sasaki, 1970). The forward and adjoint problems are solved by finite difference methods using staggered spatial and temporal grids. In the test problems considered, the data consisted of periodic surface elevation values at two stations in a channel of length 17.5 grid spacings. The data itself was taken from the exact analytical solution when this was available or else from a very exact numerical solution. The parameters estimated are the depth of water and the linear and quadratic bottom friction coefficients, which may be constant or may vary along the channel.

Several methods were used and compared to solve the parameter equations: the secant method, a direct iteration method, the Polak-Ribiere conjugate gradient method, the conjugate gradient like memoryless quasi-Newton method with Beale restarts and the BFGS quasi-Newton method. The last two algorithms were taken from the CONMIN subroutine of Shanno and Phua (1980).

In the case of constant parameters, when only one parameter is to be estimated, the secant method, direct iteration method and conjugate gradient method (which reduces simply to Davidon cubic interpolation) all produce essentially identical results in about the same number of iterations, though some experimentation is needed to find an appropriate iteration parameter for the direct iteration method. When two parameters are estimated (depth and either of the friction coefficients) this continues to be true, except that the direct iteration method becomes significantly more expensive than the other methods; the conjugate gradient method without restarts is somewhat more expensive.

In all these problems, the estimated values of the parameters obtained by all methods agree almost to four significant figures. These values differ from the exact parameter values by almost one percent, because of truncation errors in the finite difference approximation of the forward and adjoint equations. In the case of quadratic friction, the value of the objective function at the minimum is reduced by about four orders of magnitude from its starting value. For linear friction the reduction is between nine and eleven orders of magnitude, this smaller value being presumably due to the more exact treatment of the bottom friction by the finite difference algorithm in the linear case.

An attempt to estimate all three parameters was not successful in yielding accurate values. The linear and quadratic friction coefficients appear to some extent to be interchangeable and the assumed data is not sufficient to resolve them.

In the case of distributed parameters, we have used a finite element approximation by means of which the parameter functions are expressed in terms of some reduced number of coefficients such as certain nodal values of the parameters. The method has proved to be very accurate provided the total number of independent nodal values that are estimated does not exceed twice the number of data stations. The estimates obtained by the secant method, the conjugate gradient like memoryless quasi-Newton method with Beale restarts and the BFGS quasi-Newton method are completely consistent whenever the different methods converge. In general, the estimated parameter functions are, as can be expected, found to be more accurate the greater the number of nodes.

If the number of independent nodal values that are estimated does exceed twice the number of data stations then the estimated parameters have turned out to be quite unreliable and to depend on the assumed starting values.

The cpu time for solving the forward problem and the adjoint problem is almost the same and is the major part of the total computational cost. One iteration (involving integrating the model equations forward and the adjoint equations backward once) requires about 0.25 second on an UNIX SUN Sparcstation 1.

APPENDIX B

The conjugate-gradient algorithm is an iterative method for unconstrained minimization that produces a better approximation to the minimum of a general unconstrained nonlinear function of N variables, $x_1, x_2, \ldots, x_N$ with each iteration. Within a given iteration an estimate is made of the best way to change each component of the vector **x**, so as to produce the maximum reduction of the function, by finding the gradient of the function with respect to the variables and combining this gradient with information from the previous iterations to produce a search direction. The search direction is an estimate of the relative change in each component of the vector **x** to produce the maximum reduction in the function F. To find the magnitude of the changes along the search direction, an optimal step size must be estimated. The new vector after an iteration of the conjugate gradient $\mathbf{x}_{k+1}$ is given by the previous vector $\mathbf{x}_k$ plus an optimal step size times the search direction.

Given a set of linearly independent vectors $-\mathbf{g}_0, -\mathbf{g}_1, \ldots, -\mathbf{g}_{n-1}$, one can construct a set of mutually G-conjugate (G is a positive definite symmetric matrix) directions $\mathbf{d}_0, \mathbf{d}_1, \ldots, \mathbf{d}_{n-1}$ by the following procedure. Set

$$\mathbf{d}_0 = -\mathbf{g}_0$$

and then for $i = 1, \ldots, n-1$ successively define

$$\mathbf{d}_i = -\mathbf{g}_i + \sum_{j=0}^{i-1} a_{ij}\mathbf{d}_j$$

where a_{ij} are coefficients chosen so that $\mathbf{d}_i$ is G-conjugate to the previous directions $\mathbf{d}_{i-1}$, $\mathbf{d}_{i-2}, \ldots, \mathbf{d}_0$. This is possible if, for $l = 0, \ldots, i-1$,

$$\mathbf{d}_i^{\mathrm{T}}\mathbf{G}\mathbf{d}_l = -\mathbf{g}_i^{\mathrm{T}}\mathbf{G}\mathbf{d}_l + \sum_{j=0}^{i-1} a_{ij}\mathbf{d}_j^{\mathrm{T}}\mathbf{G}\mathbf{d}_l = 0.$$

If previous coefficients a_{ij} were chosen so that at $\mathbf{d}_0, \ldots, \mathbf{d}_{i-1}$ are G-conjugate, then we have

$$\mathbf{d}_j^{\mathrm{T}}\mathbf{G}\mathbf{d}_l = 0 \text{ if } j \neq l$$

and hence we get

$$a_{ij} = \frac{g_i^T G d_j}{d_j G d_j} \quad \text{for all } i = 1, \ldots, n-1$$
$$j = 0, \ldots, i-1.$$

For a quadratic function $F(x) = \frac{1}{2} x^T G x + b^T x + c$, (where G has been defined earlier, b is a vector, and c a scalar) $g_k = \nabla F(x_k)$ and $g_{k+1} - g_k = G(x_{k+1} - x_k)$. Therefore

$$d_i = -g_i + \sum_{j=0}^{i-1} \frac{g_i^T (g_{j+1} - g_j)}{d_j^T (g_{j+1} - g_j)} d_j.$$

Using the fact that the subspace spanned by $g_0, \ldots, g_{i-1}$ is also the subspace spanned by $d_0, \ldots, d_{i-1}$ and the fact that

$$g_i^T d_j = 0, j = 0, \ldots, i-1$$

we obtain

$$g_i^T g_j = 0, j = 0, \ldots, i-1$$

so that we have a simpler formula

$$d_i = -g_i + \beta_i d_{i-1}$$

with

$$\beta_i = \frac{g_i^T (g_i - g_{i-1})}{d_{i-1}^T (g_i - g_{i-1})}$$

Using the equalities

$$g_i^T g_j = g_i^T d_j = 0 \qquad j = 0, \ldots, i-1$$
$$d_{i-1} = -g_{i-1} + \beta_{i-1} d_{i-2}$$

the coefficient β_i can be written as

$$\beta_i = \frac{g_i^T (g_i - g_{i-1})}{g_{i-1}^T g_{i-1}} = \frac{g_i^T g_i}{g_{i-1}^T g_{i-1}}.$$

In order to generate the direction d_i in the minimization process, we need only know current and next previous gradients g_i and g_{i-1} and the previous direction d_{i-1} (i.e., storage of three vectors). For a nonlinear function $G = \nabla^2 F$. The first expression for β_i is the Polak-Ribiere form and the second expression is the Fletcher-Reeves form. They are equal for exact quadratic functions. For real world functions which are not exactly quadratic, to reach the supposed minimum of the quadratic form, the Polak-Ribiere form accomplishes the transition to further required set of iterations more gracefully, by resetting d to be down the local gradient, which is equivalent to beginning the conjugate-gradient procedure anew.

Davidon's Cubic Interpolation Method

Davidon devised a method which uses the values of the function $f(x)$ at two points on the line $x = x_k + \lambda d$, together with values of the directional derivatives of the function along the line at the same two points. Given a point x_k and a direction of search d, where d need not be a unit vector, Davidon's cubic interpolation method for minimizing the differentiable function $f(x)$ on the line
$x = x_k + \lambda d$ is as follows:

1. Evaluate $f_0 = f(x_k)$ and $G_0 = [g(x_k)]'d$. Check that $G_0 < 0$. In the following expression

$$\alpha = \min\left\{\kappa, -\frac{2(f_0 - f_e)}{G_0}\right\}$$

choose κ and f_e, where κ is some representative magnitude for the problem (usually, $\kappa = 2$) and f_e is a preliminary estimate, preferably low than high, of $f(x_k + \lambda_m d)$, and hence determine α.

2. Evaluate $f_\alpha = f(x_k + \alpha d)$ and $G_\alpha = [g(x_k + \alpha d)]'d$.

3. If $G_\alpha > 0$, or if $f_\alpha > f_0$, proceed to rule 5. Otherwise go to rule 4.

4. Replace α by 2α, evaluate the new f_α and G_α and return to rule 3.

5. Interpolate in the interval $[0, \alpha]$ for λ_m, using

$$\frac{\lambda_m}{\alpha} = 1 - \frac{G_\alpha + w - z}{G_\alpha - G_0 + 2w}.$$

In this equation $w = \sqrt{z^2 - G_0 G_\alpha}$ and $z = \frac{3}{\alpha}(f_0 - f_\alpha) + G_0 + G_\alpha$.

6. Return to rule 5 to repeat the interpolation in the smaller interval $[0, \lambda_m]$ or $[\lambda_m, \alpha]$, according as

$$[g(x_k + \lambda_m d)]'d \geq \text{or} < 0.$$

Stop when the interval of interpolation has decreased to some prescribed value.

For further details on this method see Walsh(1975).

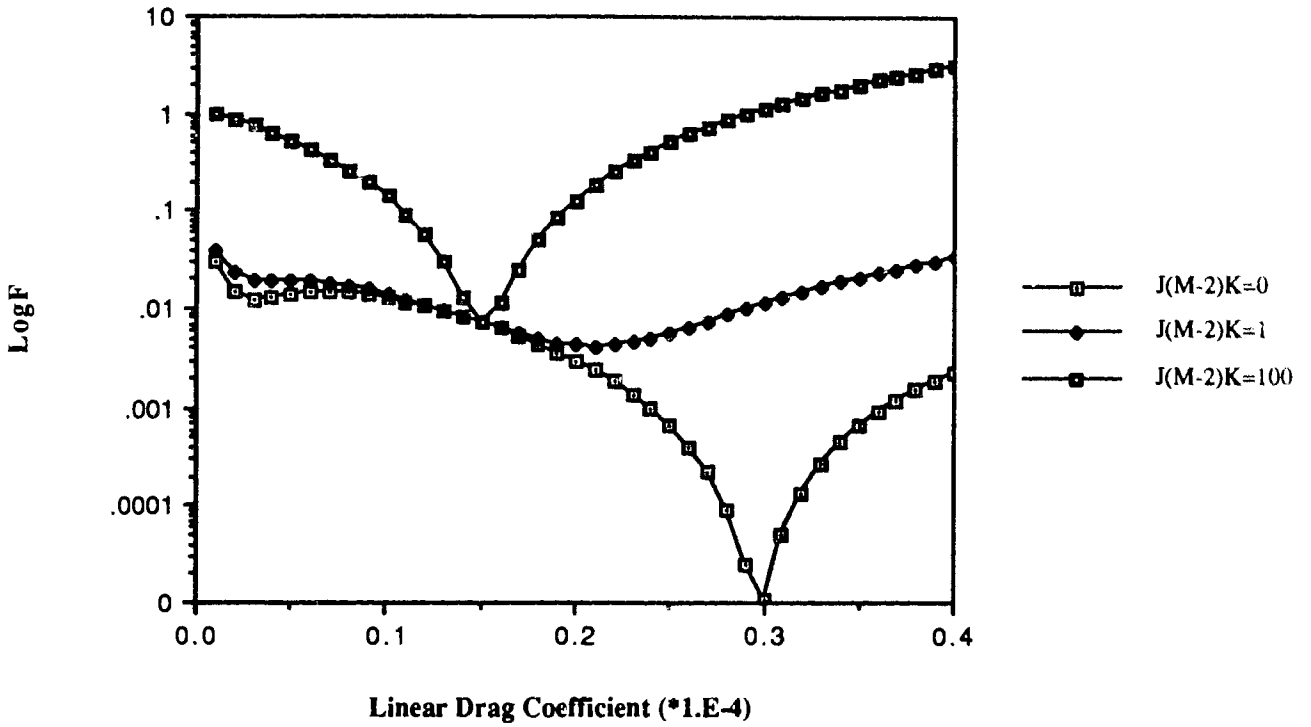
10
1
.1
.01
.001
.0001
0
LogF
0.0
0.1
0.2
0.3
0.4
Linear Drag Coefficient (*1.E-4)
J(M-2)K=0
J(M-2)K=1
J(M-2)K=100

Figure 7.1

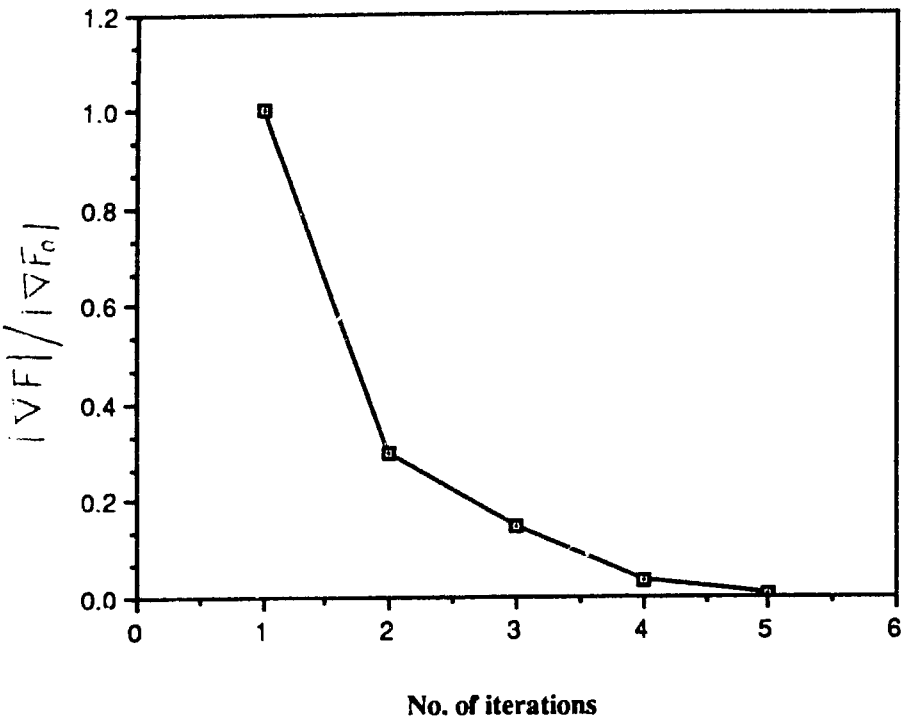

Figure 7.1(a)

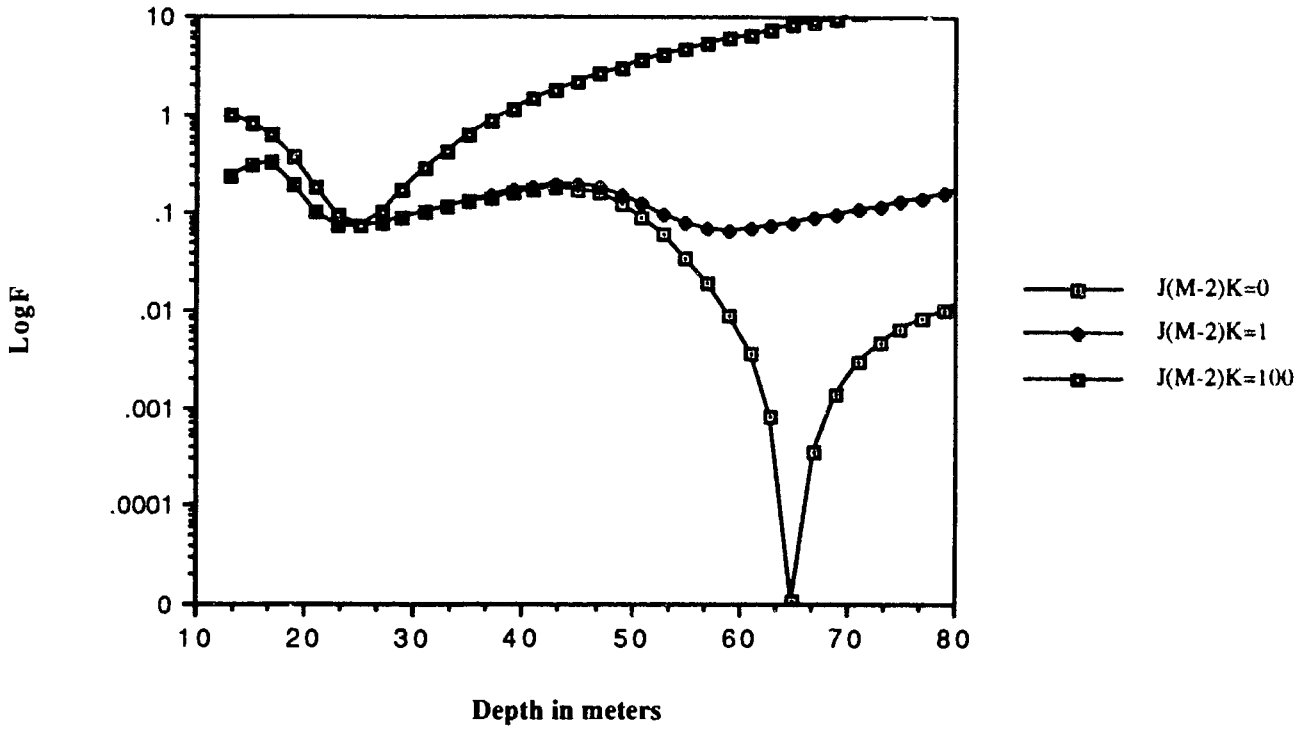
10
1
.1
.01
.001
.0001
0
LogF
10
20
30
40
50
60
70
80
Depth in meters
J(M-2)K=0
J(M-2)K=1
J(M-2)K=100

Figure 7.2

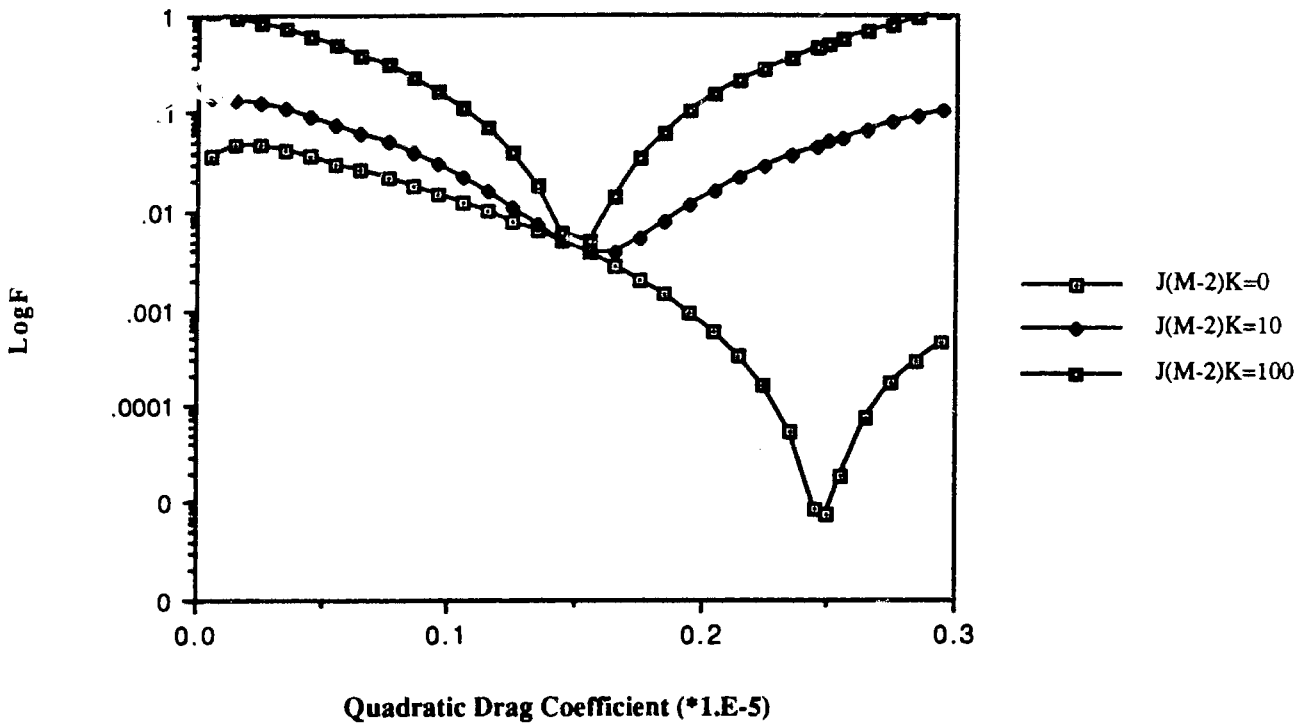
LogF
1
.1
.01
.001
.0001
0
0
0.0
0.1
0.2
0.3
Quadratic Drag Coefficient (*1.E-5)
J(M-2)K=0
J(M-2)K=10
J(M-2)K=100

Figure 7.3

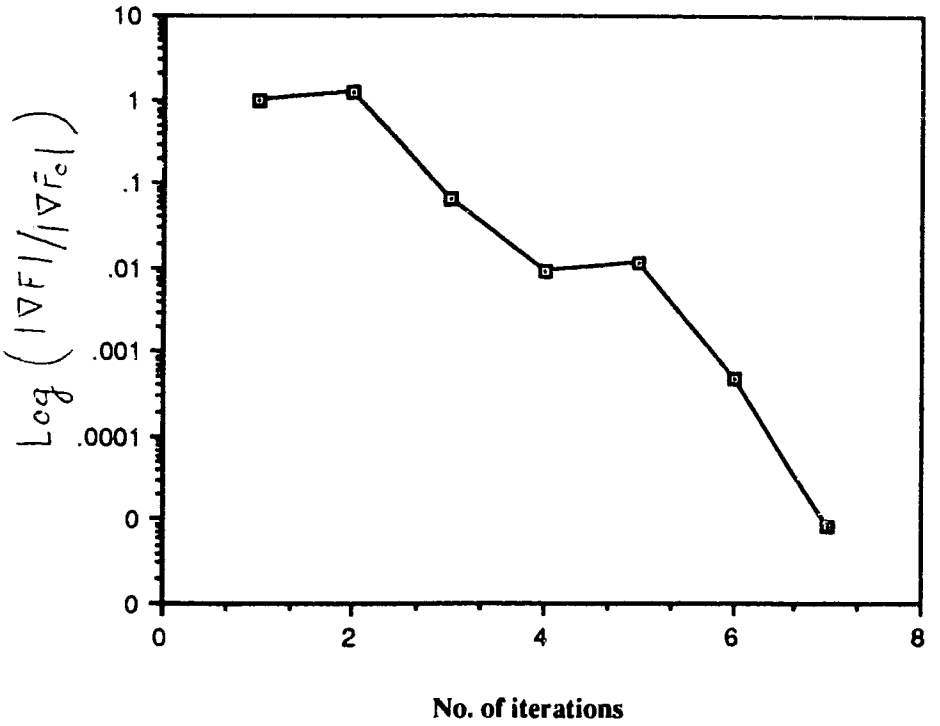

Figure 7.3(a)

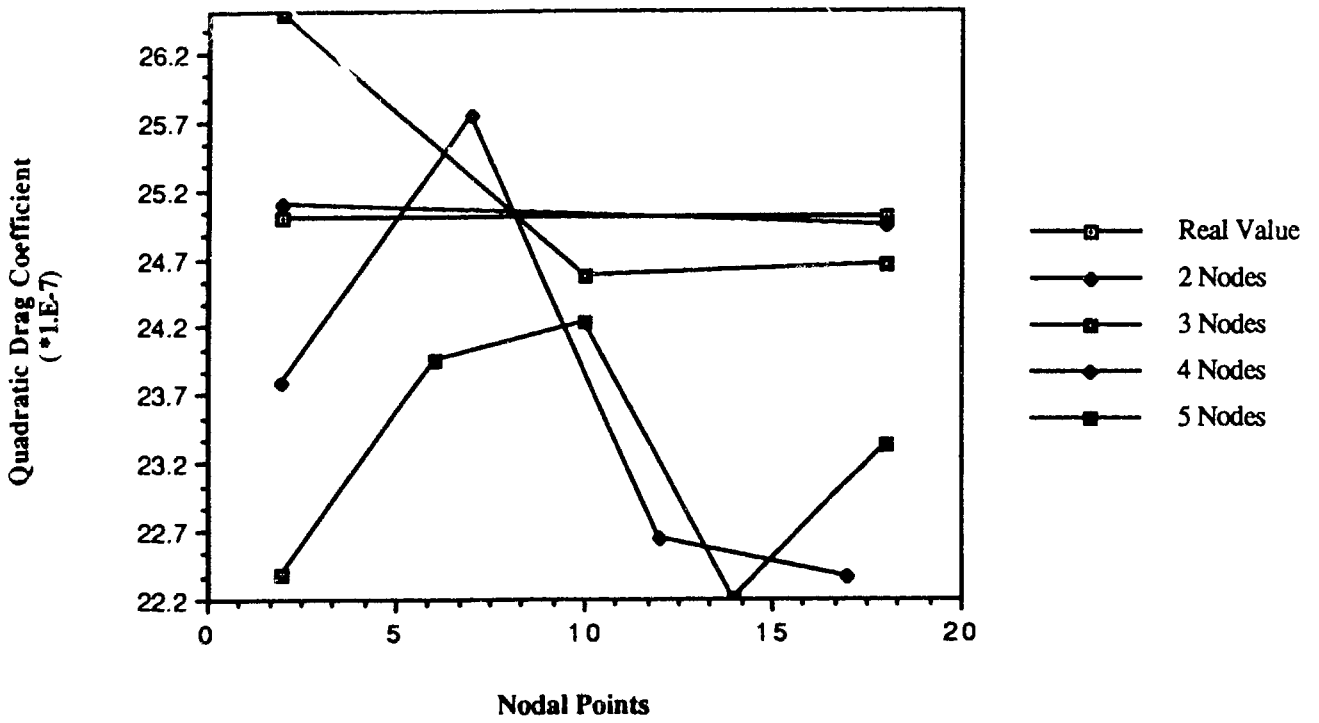
Quadratic Drag Coefficient
(*1.E-7)
26.2
25.7
25.2
24.7
24.2
23.7
23.2
22.7
22.2
0
5
10
15
20
Nodal Points
Real Value
2 Nodes
3 Nodes
4 Nodes
5 Nodes

Figure 7.4(a)

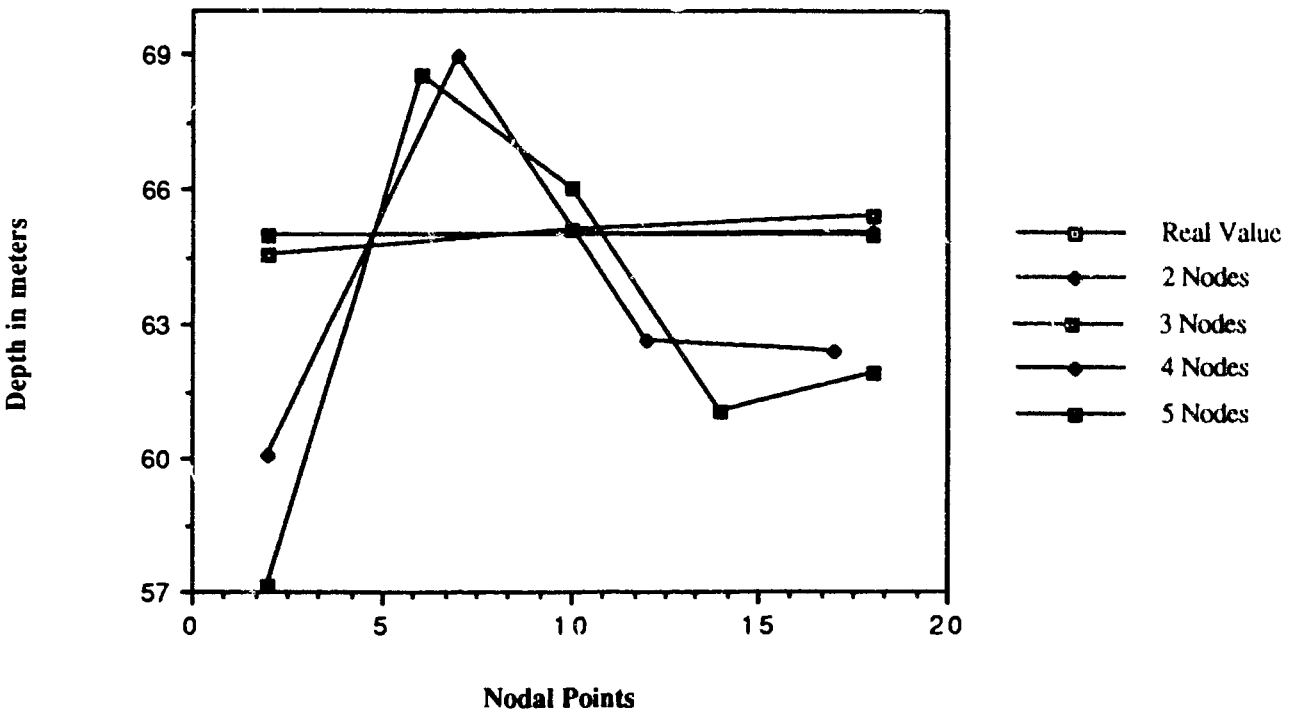
Depth in meters
69
66
63
60
57
0
5
10
15
20
Nodal Points
Real Value
2 Nodes
3 Nodes
4 Nodes
5 Nodes

Figure 7.4(b)

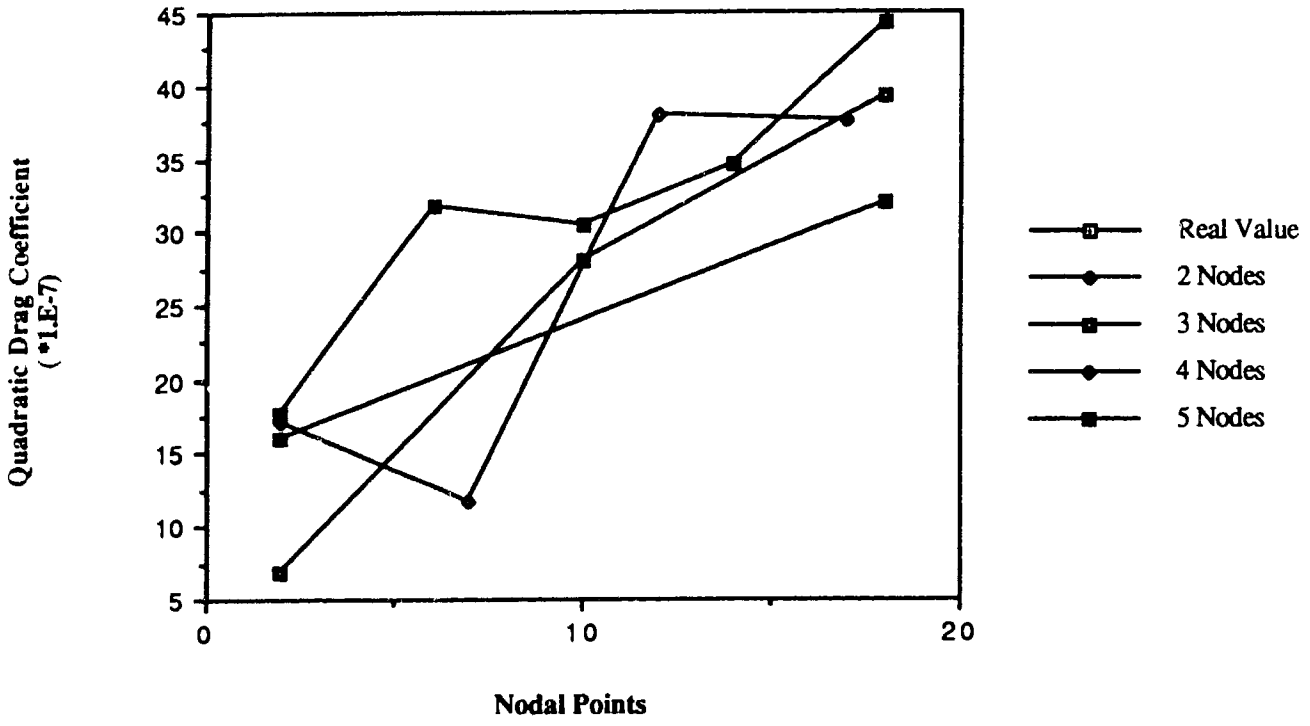
Quadratic Drag Coefficient
(*1.E-7)
45
40
35
30
25
20
15
10
5
0
10
20
Nodal Points
Real Value
2 Nodes
3 Nodes
4 Nodes
5 Nodes

Figure 7.5(a)

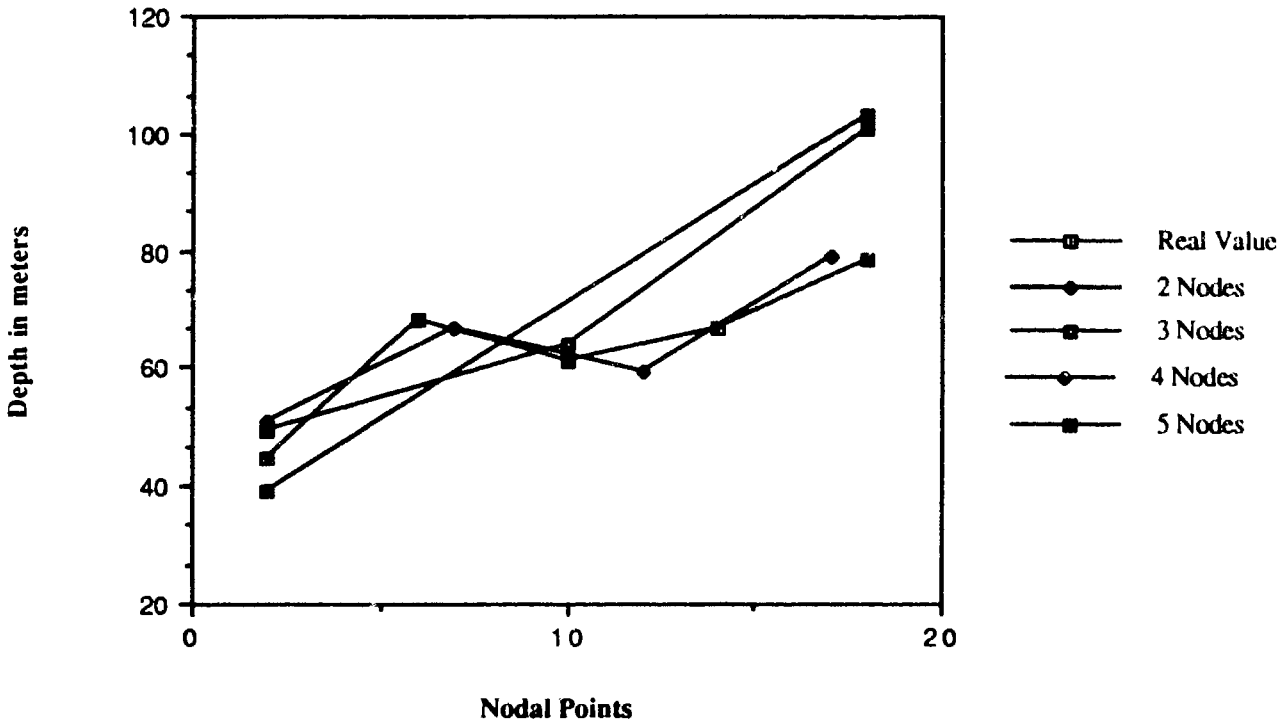
120
100
80
60
40
20
0
10
20
Depth in meters
Nodal Points
Real Value
2 Nodes
3 Nodes
4 Nodes
5 Nodes

Figure 7.5(b)

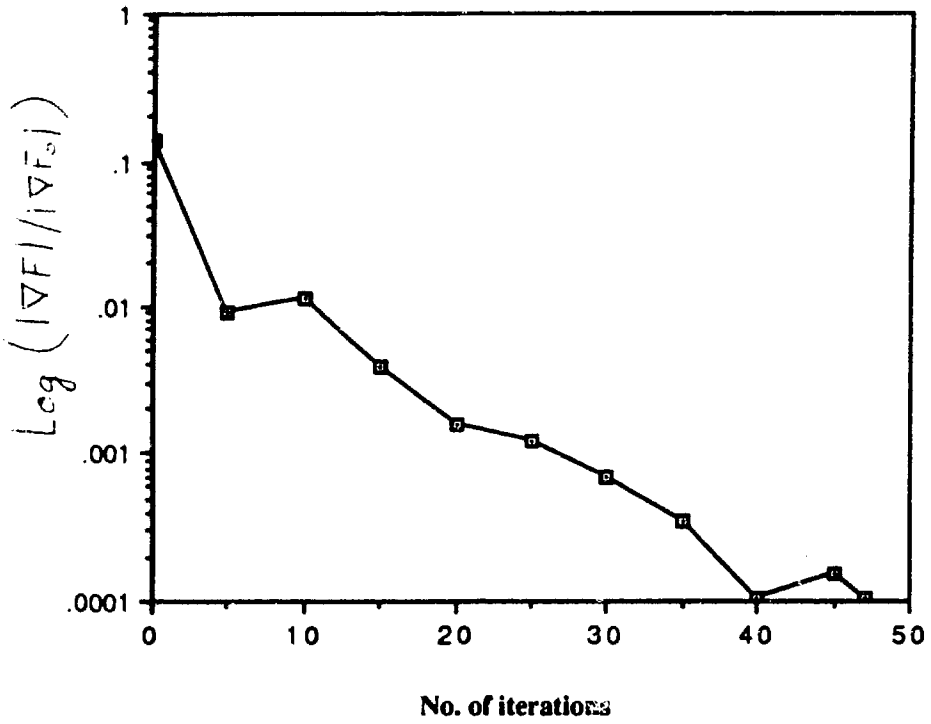

Figure 7.5(c)

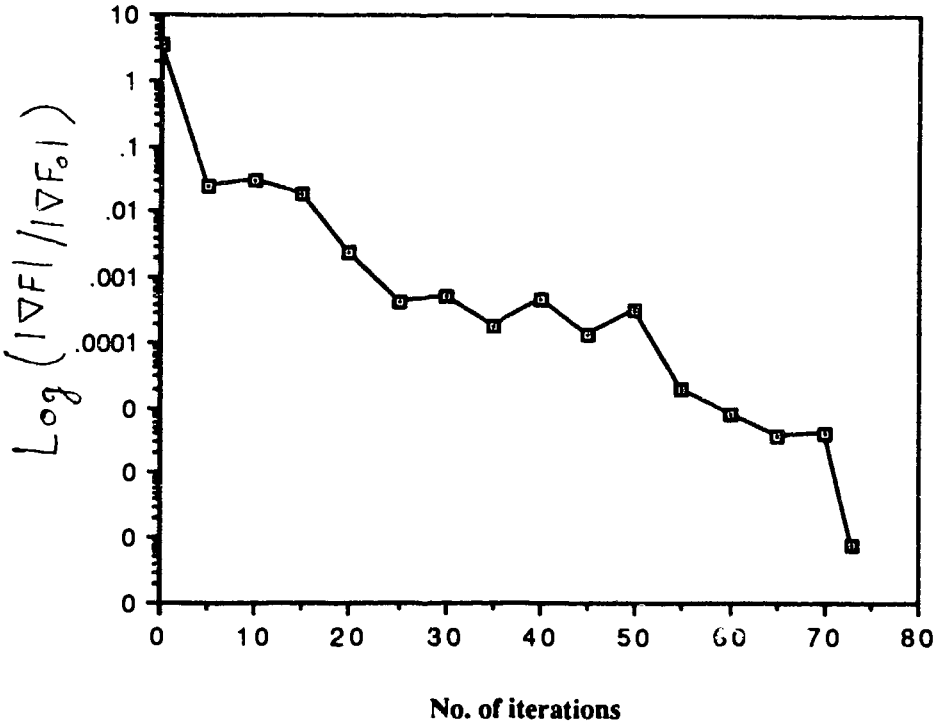
10
1
.1
.01
.001
.0001
0
0
0
0
0
10
20
30
40
50
60
70
80
Log (|∇F| / |∇F₀|)
No. of iterations

Figure 7.6

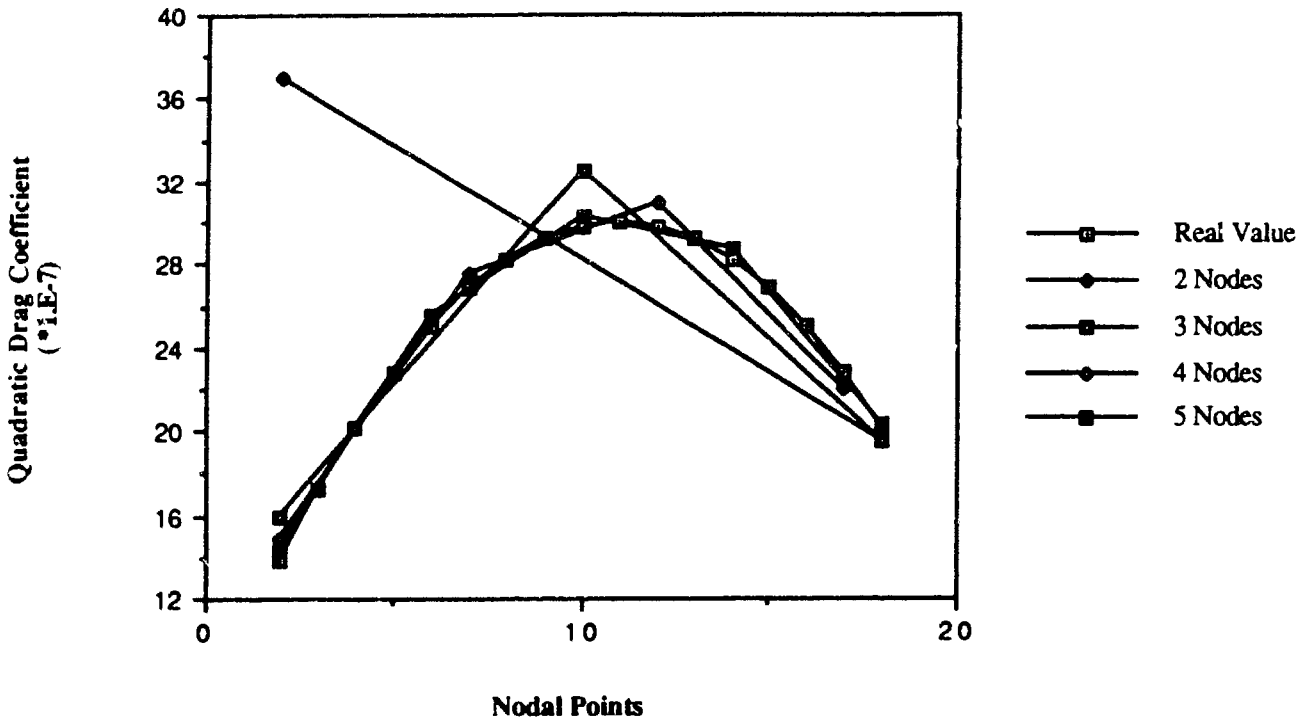
Quadratic Drag Coefficient
(*1.E-7)
40
36
32
28
24
20
16
12
0
10
20
Nodal Points
Real Value
2 Nodes
3 Nodes
4 Nodes
5 Nodes

Figure 7.7(a)

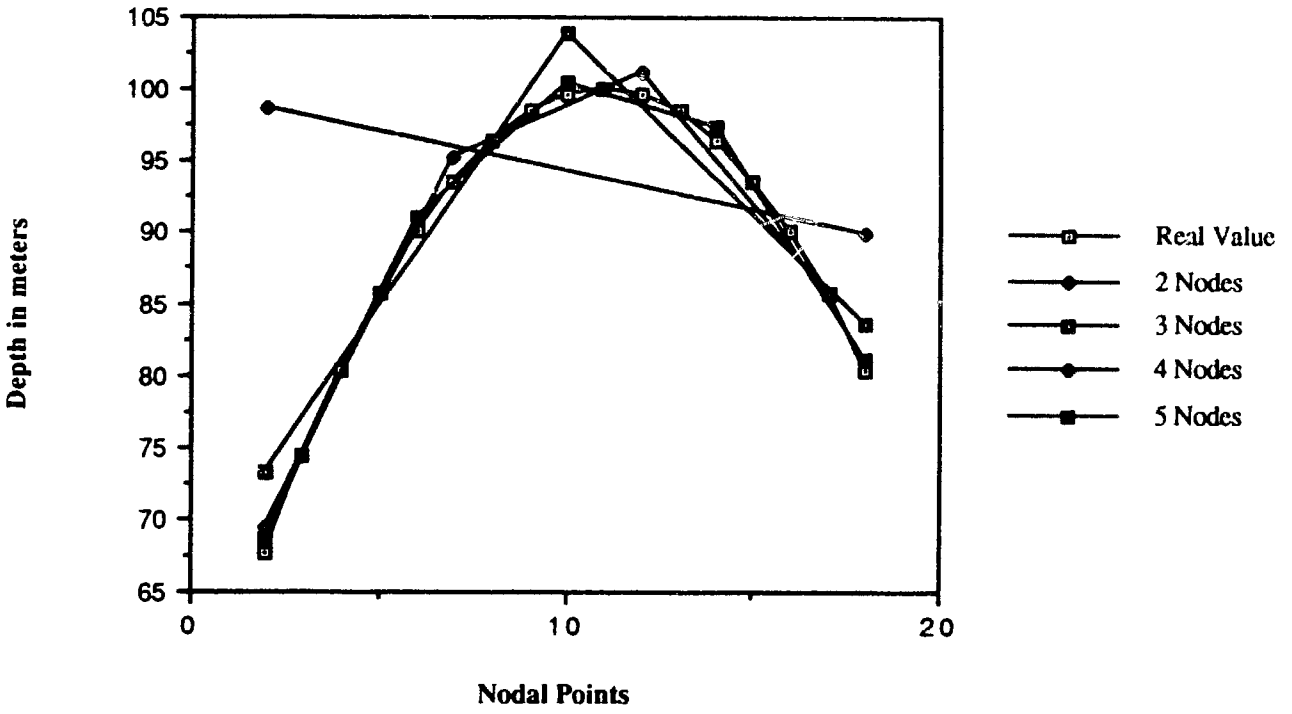
105
100
95
90
85
80
75
70
65
0
10
20
Depth in meters
Nodal Points
Real Value
2 Nodes
3 Nodes
4 Nodes
5 Nodes

Figure 7.7(b)

CHAPTER 8 PARAMETER ESTIMATION WITHOUT THE GRADIENT

In this Chapter we present a method for estimating the constant parameters in a sectionally integrated hydrodynamical model of tidal flow which does not use the adjoint formulation for evaluating the gradient of the cost function. This prompts us to make use of an optimization algorithm that needs only evaluations of the cost function itself to get to the minimum. The algorithm is known as the Powell's Direction Set Method in the literature.

We tested the algorithm on two model problems in which the parameters k_1 and h are determined. For all starting values of the parameters lying within a specified range we always reached the minimum with errors of the order 0.01%. This sounds encouraging as it saves the cpu time used in estimating the gradient of the function. But before the actual minimization procedure starts, the minimum has to be bracketed within an interval. This requires the function to be evaluated a number of times and hence, adds significantly to the cpu time. In our numerical experiments we found that the Powell method is 2-5 times as expensive in computer time as the gradient method.

8.1 Basic Equations

We again consider the channel problem as described in Chapter 6. We have the depth-integrated equations of continuity and momentum as

$$\zeta_t + (hu)_x = 0, \qquad \rho h u_t + g\rho h\zeta_x + \tau = 0$$

where τ is the bottom friction stress and ρ the density, assumed constant. (See eqns. (2.13) and (2.14a) in which $p \to \rho hu$, $q \to 0$, $H \approx h$ and $\rho = \overline{\rho} = \rho^{(s)}$.) We have only taken the linear bottom friction κ_1 into account. It is assumed that the bottom friction has the form

$$\tau = \rho \kappa_1 u$$

The equations are then given as (6.1) and (6.2). The boundary conditions are given as (6.3).

8.2 Optimization algorithm

The prime aim is to minimize the functional as given in (6.4), subject to the boundary value problem (6.1)-(6.3). The surface elevation is measured at two stations x_1 and x_2, and these are used to define the functional. The first step in the process is to bracket the minimum. This is achieved by Golden Section Search in one dimension. The idea is to get the optimum bracketing interval $a<b<c$ where the middle point b is a fractional distance 0.38197 from one end (say, a) and 0.61803 from the other end (say, c). This bracketing of the minimum is based on the principle of stepping downhill.

Once we get this interval we use the Powell's method to get to the minimum. The first step in the method is to come with a set of N linearly independent, approximately mutually conjugate directions. Then the application of N line minimizations will get us approximately to the minimum of a quadratic function. For functions F which are not exactly quadratic forms, repeated cycles of N line minimizations will in due course converge quadratically to the minimum. A detailed discussion of the method is given in Press et al (1989).

8.3 Numerical Tests

The numerical algorithm used to solve the basic equations (6.1)-(6.3) are given in (6.11) and (6.12). Equations (6.11) and (6.12) are stepped forward starting from zero initial values. The initial transients disappear after several periods and the solution becomes periodic. Again we assume that the values of ζ at the two grid points m=8 and m=16 are known from measurements. The convergence criterion used is based on the magnitude of the function value. Essentially two tests were conducted.

8.3.1 Constant coefficients, unsegmented channel

The exact solution of (6.1)-(6.3) with boundary condition (7.3) is given by

$$Z_i(t) = \Re\left\{\frac{\zeta_0 \cos \alpha x_i}{\cos \alpha L} e^{i\omega t}\right\}, \qquad \alpha = \sqrt{\frac{\omega^2 - ik\omega}{gh}},$$

and this is used as the "empirical" values at the two points x_1 and x_2.

We consider the following three cases: (i) h is known (= 65m) and k_1 is determined, the true value being 0.3×10^{-4}; (ii) k_1 is known (= 0.3×10^{-4}) and h is determined, the true value being 65; (iii) both k_1 and h are to be determined, with their true values being 0.3×10^{-4} and 65 respectively. The results are summarized in Table 8.1.

Case	Start Value	Final Value	N
(i)	$k_1=0.2\times10^{-4}$	0.2975×10^{-4}	44
(ii)	$h = 55$	65.27	44
(iii)	$k_1=0.2\times10^{-4}$ $h = 55$	0.2986×10^{-4} 65.25	391

Table 8.1. Estimates in the numerical test no. 1.

In another series of tests we have used a modified objective function equal to the square norm of the amplitude of the fundamental in the difference between $\zeta(x_i,t)$ and $Z_i(t)$. This amplitude was extracted from the accumulated values of the elevation over the last 120 time steps by using the Fast Fourier Transform (see, De Boor and Conte, 1980). The number of iterations in the case of (i) and (ii) were 46 but in the case (iii) was only 149.

8.3.2 Constant coefficients, segmented channel

We now consider the case where the channel is considered to be divided into two parts with different values of bathymetry and bottom friction. In this example the value $M = 90$ and $\Delta x =$ 8000m is used. The two ends of the channel are subjected to boundary conditions of the form (6.3). In $0 < x < L_1$, the parameters are k_1 and h_1 while in $L_1 < x < L$ they are k_2 and h_2. At the dividing point the velocity and surface elevation are considered to be continuous.

The solution to the equations (6.1)-(6.3) is given by

Region 1

$$Z_i(x) = \frac{2\zeta_0}{D}\,\alpha_1\cos\alpha_1 x_i\,\exp(i\alpha_2 L),$$

where $\alpha_1 = \sqrt{\frac{\omega^2 - ik_1\omega}{gh_1}}$ and α_2 is defined similarly, and

$D = \alpha_1 P\cos\alpha_1 L_1 - i\alpha_2 Q \sin\alpha_1 L_1$, $P = \exp(i\alpha_2 L_1) + \exp(i\alpha_2(2L-L_1))$ and

$Q = \exp(i\alpha_2 L_1) - \exp(i\alpha_2(2L-L_1))$.

Region 2

$$Z_i(x) = \frac{2i\zeta_0\alpha_2}{PD}\sin(\alpha_1 L_1)\left(\exp(i\alpha_2(L+x_i)) - \exp(i\alpha_2(3L-x))\right)$$

$$+\frac{\zeta_0}{P}\left(\exp(i\alpha_2(L-L_1+x_i)) - \exp(i\alpha_2(3L-L_1-x))\right) + \zeta_0\exp(i\alpha_2(L-x_i))$$

We took $h_1 = 65$ and $h_2 = 50$, regarded as known, while k_1 and k_2 are to be determined, the true values being 0.3×10^{-4} and 0.15×10^{-4}. The starting values are taken to be 0.2×10^{-4} and 0.05×10^{-4}. The final values are 0.2982×10^{-4} and 0.1462×10^{-4}. It takes 122 iterations for the convergence with tolerance of 10^{-4} when we evaluate the function by using Fast Fourier Transform and 293 iterations when the function is obtained by using the method in Chapter 6.

REFERENCES

Anon. (1980). Climatic study of the Persian Gulf and Gulf of Oman. (Naval Oceanography Command Detachment, Asheville, N. Carolina)

Backhaus, J.O. (1985). A three-dimensional model for simulation of shelf-sea dynamics, Dt. Hydrogr. Z., **38**, 165-187.

Bailey, P.B. (1978). SLEIGN An eigenvalue-eigenfunction code for Sturm-Liouville problems, SAND77-2044, Sandia Laboratories, Albuquerque, N.M.

Bennett, A.F. and McIntosh, P.C. (1982). Open ocean modelling as an inverse problem: Tidal theory. J. Phys. Oceanog., **12**, 1004-1018.

Brewer, P., A. Fleer, S. Kadar, D. Shafer and C. Smith (1978). Chemical oceanographic data from the Persian Gulf and Gulf of Oman. Woods Hole Oceanog. Inst. Tech. Rep. WHOI-78-37, 105pp.

Brebbia, C.A. and P.W. Partridge (1976). Finite element simulation of water circulation in the North Sea, Appl. Math. Model., **1**, 101-107.

Blumberg, A.F. and Kantha, L.H. (1985). Open boundary conditions for circulation models. J. Hydraulic Engng., **111**, 237-255.

Carrera, J. and Neumann, S.P. (1986). Estimation of aquifer parameters under transient and steady state conditions. Part I. Maximum likelihood method incorporating prior information. Water Resourc. Res. **22**, 199-210. Part II. Uniqueness, stability and solution algorithms. Water Resourc. Res. **22**, 211-227. Part III. Application to synthetic and field data. Water Resourc. Res., **22**, 228-241.

Cekirge, H.M., R.W. Lardner and R.J. Fraga (1986). Adaptation of the solution of the two-dimensional tidal equations using the method of characteristics to wind-induced currents and storm surges, Comp. Math. Applic., **12A**, 1081-1090.

Chavent,G., Dupuy,M. and Lemonnier, P. (1975). History matching by use of optimal theory. Soc. Petroleum Engrs J., **15**, 74-86.

Connor, J.J. and C.A. Brebbia (1976). Finite elements for fluid flow, London: Butterworth.

Connor, J.J. and J. Wang (1973). Finite element modelling of hydrodynamic circulation. In Numerical Methods in Fluid Mechanics (ed. C.A. Brebbia & J.J. Connor), 335-387, London: Pentech Press.

Conte, S.D. and Carl de Boor (1980). Elementary Numerical Analysis: an algorithmic approach, third edition, McGraw Hill Publishing Company, New York.

Courtier,P. and Talagrand, O. (1987) Variational assimilation of meteorological observations with the adjoint vorticity equation II: Numerical results. Quart. J. Roy. Meteor. Soc., **113**, 1329-1348.

Das, S.K. and R.W. Lardner (1989). A smooth fit to a series of measurements of salinity, temperature and density in the Arabian Gulf, SFU preprint.

Davies, A.M. (1980a). On formulating a three-dimensional hydrodynamic sea model with an arbitrary variation of vertical eddy-viscosity, Comp. Meth. Appl. Mech. Engg., **22**, 187-211.

Davies, A.M. (1980b). Application of the Galerkin method to the formulation of a three-dimensional nonlinear hydrodynamic numerical sea model, Appl. Math. Model., **4**, 245-255.

Davies, A.M. (1983). Formulation of a linear three-dimensional hydrodynamic sea model using a Galerkin eigenfunction method, Int. J. Num. Methods Fluids, **3**, 33-60.

Davies, A.M. (1985a). On determining the profile of steady wind-induced currents, Appl. Math. Modelling, **9**, 409-418.

Davies, A.M. (1985b). Application of the Dufort-Frankel and Sau'lev methods with time splitting to the formulation of a three-dimensional hydrodynamical sea model, Int. J. Num. Meth. Fluids, **5**, 405-425.

Davies, A.M. (1987). On extracting current profiles from vertically integrated numerical models, Coastal Engg., **11**, 445-477.

Davies, A.M. (1988). On formulating two-dimensional vertically integrated hydrodynamic numerical models with an enhanced representation of bed stress, J. Geophys. Res., **93**, 1241-1293.

Davies, A.M. and A. Owen (1979). Three-dimensional numerical sea model using the Galerkin method with a polynomial basis set, Appl. Math. Model., **3**, 421-428.

Duff, G.F.D. (1983). A special ADI model for the Laplace tidal equations, Comp. Math. Applic., **9**, 507-516.

Flather, R.A. and N.S. Heaps (1975). Tidal computations for Morecambe Bay, Geophys. Jl R. Astr. Soc., **42**, 489-517.

Forristal, G.Z. (1974). Three-dimensional structure of storm-generated currents, J. Geophys. Res., **79**, 2721-2729.

Forristal, G.Z. (1980). A two-layer model for hurricane-driven currents on an irregular grid, J. Phys. Oceanogr., **10**, 1417-1438.

Galt, J.A., D.L. Payton, G.M. Torgrimson and G. Watabayashi (1983). Trajectory analysis for the Nowruz oil spill with specific application to Kuwait. Report of National Oceanic and Atmospheric Agency, Seattle, Washington.

Golub, G.H. and C.F. Van Loan (1983). Matrix Computations, The Johns Hopkins University Press, Baltimore, Maryland, U.S.A.

Hansen, W., (1962). Hydrodynamical methods applied to oceanographic problems, Proc. Symp. Math. Hydrodyn. Phys. Ocean., 24-34. Institut fur Meereskunde, Universitat Hamburg.

Harlan, J. and O'Brien, J.J. (1986). Assimilation of scatterometer winds into surface pressure fields using a variational method. J. Geophys. Res., **91**, 7816-7836.

Hearn, C.J. and J.R. Hunter (1988). A new method of describing bottom stress in two-dimensional hydrodynamical models of shallow, homogeneous seas, estuaries and lakes, Appl. Math. Model., **12**, 573-580.

Henaidi, A.K. (1984). Preliminary report on drifting buoy movements, MEPA, Gulf Area Oil Companies Mutual Aid Organization Doc. No. GO-86/87-07.

Hoffman , R.N. (1986). A four-dimensional analysis exactly satisfying equations of motion, Mon. Wea. Rev., **114**, 388-397.

Hughes, P. and J.R. Hunter (1980). A proposal for a physical oceanography program and numerical modelling in the KAP region. Project for Kuwait Action Plan 2/2, UNESCO, Paris.

Hunter, J.R. (1975). A note on quadratic friction in the presence of tides, Estuarine and Coastal Marine Science, 3, 473-475.

Hunter, J.R. (1982). The physical oceanography of the Arabian Gulf: A review and theoretical interpretation of previous measurements. 1st Gulf Conference on Environment and Pollution, Kuwait.

Hunter, J.R. (1983). Aspects of the dynamics of the residual circulation in the Arabian Gulf, in *Coastal Oceanography* (ed. H.G.Gade, A.Edwards and H.Svendsen, Plenum Press) pp. 11-42.

Jamart, B.M. and Ozer, J. (1986). Numerical boundary layers and spurious residual flows, J. Geophys. Res., **91**, 10,621-10,631.

Jelesniansky, C.P. (1970). Bottom stress time history in linearized equation of motion for storm surges, Mon. Wea. Rev., **98**, 472-478.

Johns, B., P.C. Sinha, S.K. Dube, U.C. Mohanty and A.D. Rao (1983). Simulation of storm surges using a three-dimensional numerical model: an application to the 1977 Andhra cyclone. Quart. J. R. Met. Soc., **109**, 211-224.

Jordan, T.F. and J.R. Baker (1980). Vertical structure of time-dependent flow dominated by friction in a well-mixed fluid, J. Phys. Oceanogr., **10**, 1091-1103.

Laevastu, T. (1975). Multilayer hydrodynamical-numerical models. In Proc. Symp. Modelling Tech.(ASCE), 1010-1020.

Lai, C. (1976). Some computational aspects of one- and two-dimensional unsteady flow simulation by the method of characteristics, Proc. Int. Symp. Unsteady Flow Open Channels, D1-12, Int. Association for Hydraulic Research, Newcastle upon Tyne.

Lardner, R.W. (1990). Stability of the numerical solution of a parabolic system with integral subsidiary conditions. Comp. Math. Applics., **19**, 41-46.

Lardner, R.W. (1990). Numerical solution of the linearized three-dimensional tidal equations using eddy-viscosity eigenfunctions. J. Geophys. Res. (Oceans), **C95**, 22,269-22,274.

Lardner, R.W. (1991). Optimal control of open boundary conditions in a numerical tidal model. SFU preprint

Lardner, R.W., M.S. Belen and H.M. Cekirge (1982). Finite difference model for tidal flows in the Arabian Gulf. Comp. & Math. w. Applics., **8**, 425-444.

Lardner, R.W. and Cekirge, H.M. (1987). An efficient algorithm for the computation of three-dimensional wind-driven currents, Engng. Analysis **4**, 425-444.

Lardner, R.W. and H.M. Cekirge (1988). A new algorithm for three-dimensional tidal and storm-surge computations, Applied Mathematical Modelling **12**, 471-488.

Lardner, R.W., H.M. Cekirge and N. Gunay (1986). Numerical solution of the two-dimensional tidal equations using the method of characteristics, Comp. Maths. Applic., **12A**, 1065-1080.

Lardner, R.W. and S.K. Das (1990). On the computational of flows driven by density gradient: residual currents in the Arabian Gulf, Applied Mathematical Modelling, in press.

Lardner, R.W., W.J. Lehr, R.J. Fraga and M.A. Sarhan (1987). Residual currents in the Arabian Gulf I: Density-driven flow. Arabian J. Sci. Engng., **12**, 341-354.

Lardner, R.W., W.J. Lehr, R.J. Fraga and M.A. Sarhan (1988a) Residual currents in the Arabian Gulf II: Wind-driven flow. Arabian J. Sci. Engng., **13**, 411-423.

Lardner, R.W., W.J. Lehr, R.J. Fraga and M.A. Sarhan (1988b). Residual currents and pollutant transport in the Arabian Gulf. Appl. Math. Modelling, **12**, 379-390.

Lardner, R.W. and P. Smoczynski (1990). A vertical/horizontal splitting algorithm for three-dimensional tidal and storm-surge computations, Proc. Roy. Soc. (London) **A430**, 263-284.

Lardner, R.W. and Y. Song, (1990a). A hybrid spectral method for the 3-D numerical modelling of nonlinear flows in shallow seas, submitted.

Lardner, R.W. and Y. Song, (1990b). A comparison of spatial grids for numerical modelling of flows in near-coastal seas, submitted.

Le Dimet, F.X. and Navon, I.M. (1989). Variational and optimization methods in meteorology - a review, Mon. Wea. Rev. (submitted).

Le Dimet, F.X. and Talagrand, O. (1986). Variational algorithms for analysis and assimilation of meteorological observations: theoretical aspects, Tellus **38A**, 97-110.

Leendertse, J.J. (1967). Aspects of a computational model for long period water-wave propagation, Rand Corp. Rep., RM-5294-PR.

Leendertse, J.J. and S.K. Liu (1975a). A three-dimensional model for estuaries and coastal seas, Rand Corp. Tech. Rep., R-1764-OWRT.

Leendertse, J.J. and S.K. Liu (1975b). Modelling of three-dimensional flows in estuaries. In Modelling Techniques, pp. 625-6, ASCE.

Le Provost, C. and A. Poncet (1978). Finite element method for spectral modelling of tides, Int. J. Num. Meth. Engg., **12**, 853-871.

Le Provost, C., G. Rougier and A. Poncet (1981). Numerical modelling of the harmonic constituents of the tides, with application to the English channel, J. Phys. Oceanogr., **11**, 1123-1138.

Lewis, J.M. and Derber, J.C. (1985). The use of adjoint equations to solve a variational adjustment problem with advective constraints, Tellus **37A**, 309-322.

Lorenc, A.C. (1986). Analysis methods for numerical weather prediction. Quart. J. Roy. Meteor. Soc., **112**, 1177-1194.

Lorenc, A.C. (1988). Optimal nonlinear objective analysis. Quart. J. Roy. Meteor. Soc., **114**, 205-240.

Lystad, M. and Martinsen, E.A. (1980). The importance of barotropic current for the simulation of oil spills, Norwegian Meteorol. Inst. Tech. Rep. No. 49.

Matthews, J.B. and J.C.H. Mungall (1972). A numerical tidal model and its application to Cook Inlet, Alaska, J. Mar. Res., **30**, 27-38.

Mathison, J.P. and Johansen, Ø. (1983). A numerical tidal and storm surge model of the North Sea, Marine Geodesy, **6**, 267-291.

Marchuk, G.I. (1974). Numerical solution of the problems of the dynamics of the atmosphere and oceans, (Leningrad: Gidrometeoizdat).

Nash, S.G. (1985). Preconditioning of truncated-Newton methods. SIAM J. Sci. Stat. Comput., **6**, 599-616.

Navon, I.M. (1986). A review of variational and optimization methods in meteorology, in Variational methods in geosciences, edited by Y. Sasaki (Elsevier, New York) pp. 29-34.

Navon, I.M. and Legler, D.M. (1987). Conjugate gradient methods for large-scale minimization in meteorology. Mon. Wea. Rev., **115**, 1479-1502.

Neumann, G. and Pierson, W.J. (1964). Principles of physical oceanography (Prentice-Hall Inc., Englewood Cliffs, N.J.)

Nocedal, J. (1980). Updating qasi-Newton matrices with limited storage. Mathematics of Computation, **35**, 773-782.

Panchang, V.G. and O'Brien, J.J. (1989). On the determination of hydraulic model parameters using the adjoint state formulation in Modelling marine systems, edited by A.M.Davies (CRC Press) pp 6-18.

Pearson, C.E. and D.F. Winter (1977). On the calculation of tidal currents in homogeneous estuaries, J. Phys. Oceanogr., **7**, 520-531.

Pinder, G.F. and Gray, W.G. (1977). Finite element simulation in surface and subsurface hydrology, Academic Press, New York.

Phillips, N.A., (1957). A coordinate system having some spacial advantages for numerical forecasting. J. Meteorol., **14**, 184-186.

Press, W.H., B.P. Flannery, S.A. Teukolsky and W.T. Vetterling (1989). Numerical Recipes, The Art of Scientific Computing (FORTRAN Version), Cambridge University Press.

Prevost, C. and Salmon, R. (1986). A variational method for inverting hydrographic data. J. Mar. Sci., **44**, 1-34.

Sasaki, Y. (1955). A variational study of the numerical prediction based on the variational principle. J. Meteor. Soc. Japan, **33**, 262-275.

Sasaki, Y. (1970). Some basic formalisms in numerical variational analysis. Mon. Wea. Rev., **98**, 875-883.

Schlick, T. and A. Fogelson (1990). TNPACK - A truncated Newton Minimization Package for Large-Scale Problems, ACM Transactions of Mathematical Software.

Sengupta, S., S.S. Lee and H.P. Miller (1978). Three-dimensional numerical investigations of tide and wind-induced transport processes in Biscayne Bay, Sea Grant Tech. Bull., No. 39, University of Miami.

Shanno, D.F. and Phua, K.H. (1980). Remark on algorithm 500, a variable metric method for unconstrained minimization. ACM Trans. on Math. Software, **6**, 618-622.

Simons, T.J. (1974). Verification of numerical models of Lake Ontario, Part I, J. Phys. Oceanogr., **4**, 507-519. 1975, Part II, J. Phys. Oceanogr., **5**, 98-110.

Smedstad, O.M. (1989). Data assimilation and parameter estimation in oceanographic models. PhD thesis, Geophysical Fluid Dynamics Institute, Florida State University, Tallahassee.

Smedstad, O.M. and James J. O'Brien (1991). Variational data assimilation and parameter estimation in an equatorial Pacific Ocean model, Prog. Oceanog., **26**, 179-241.

Song, Y. (1990). Some Three-Dimensional Computational Fluid Dynamics Problems for Shallow Seas, Ph.D. thesis, Department of Mathematics and Statistics, Simon Fraser University, Burnaby, Canada.

Sundermann, J. (1974). A three-dimensional model of a homogeneous estuary, Proc. Conf. Coastal Engg., 2337-2390, ASCE.

Talagrand, O. and Courtier, P. (1987). Variational assimilation of meteorological observations with the adjoint vorticity equation I: Theory. Quart. J. Roy. Meteor. Soc., **113**, 1311-1328.

Thepaut, J. -N. and Philippe Courtier (1991). Four-dimensional variational data assimilation using the adjoint of a multilevel primirive equation model.

Townson, J.M. (1974). An application of the method of characteristics to tidal calculations in x-y-t space, J. Hydraul. Res., **12**, 499-523.

Tziperman, Eli and W.C. Thacker (1989). An optimal-control/adjoint equations approach to studying the oceanic general circulation, J. Phys. Oceanogr., **19**, 1471-1485.

Tziperman, Eli, W.C. Thacker, R.B. Long and S.M. Hwang (1990a). Oceanic data analysis using a general circulation model : simulations, preprint.

Tziperman, Eli, W.C. Thacker, R.B. Long, S.M. Hwang and S.R. Rintoul (1990b). A North Atlantic inverse model using an oceanic general circulation model, preprint.

Walsh, G.R. (1975). Methods Of Optimization. (John Wiley & Sons, London).

Wang, J.D. (1978). Real time flow in unstratified shallow water, J. Waterway Port, Coastal Ocean Div., A.S.C.E., 104, 53-68.

Welander, P. (1957). Wind action on a shallow sae: some generalization of Ekman's theory, Tellus, 9, 45-52.

Yu, L. and O'Brien, J.J. (1990). Using ocean current data to determine the wind stress. J. Phys. Oceanog. (submitted).